博士論文（要約）

A Study of Supercell Tornadogenesis Using Data Assimilation and High-resolution Ensemble Forecasts

（データ同化と高解像度アンサンブル予報を用いた
スーパーセル竜巻の発生に関する研究）

横　田　　祥

Abstract

Most strong tornadoes are spawned by supercells: convective storms having persistent mesocyclones which are mesoscale vortices of diameters of $O(1)$ km. Such tornadoes in supercells (supercell tornadoes) are considered to be generated in the following processes that proceed in order of (i) genesis of midlevel mesocyclones (MMCs) due to tilting environmental horizontal vorticity, (ii) genesis of low-level mesocyclones (LMCs) due to tilting baroclinically generated horizontal vorticity in downdrafts of the storm, and (iii) tornadogenesis due to stretching vertical vorticity in updrafts near the surface induced by vertical perturbation pressure gradient force (VPPGF) below LMCs. However, these processes are considered based on limited observations, deterministic numerical simulations, and idealized sensitivity numerical experiments. In fact, the mechanisms of actual tornadogenesis have been examined only for several cases. Furthermore, several different origins of vorticity and circulation of tornadoes have been proposed: horizontal vorticity due to the baroclinity, the surface friction, and vertical shear of the environmental wind. In order to clarify the relationship between tornadoes, LMCs, and the surrounding environment, the origin of vorticity and circulation of the tornado, and conditions for tornadogenesis, we performed ensemble forecasts of an actual supercell tornado generated in Japan through assimilation of dense observations and ensemble-based statistical analyses. Such ensemble-based analyses give new approaches for analyzing mesocyclogenesis and tornadogenesis.

The case we studied in this thesis is a supercell tornado that passed through Tsukuba city on the Kanto Plain, Japan, at about 1230–1250 Japan Standard Time (JST) 6 May 2012. The ensemble forecasts of the tornado were performed with Japan Meteorological Agency non-hydrostatic model (JMANHM), where the initial states were prepared by a nested four-dimensional local ensemble transform Kalman filter (4D-LETKF) of 32 members. In outer LETKF, the grid interval was 15 km horizontally, and hourly observations used in the mesoscale analysis of JMA were assimilated in a 6-h assimilation window from 0900 JST 3 May 2012. In inner LETKF, the grid interval was 1.875 km horizontally, and dense surface and radar data observed every 10 minutes were assimilated in an hourly assimilation window from 0300 JST 6 May 2012. The surface meteorological data were horizontal winds, temperature, and relative humidity observed at Meteorological Observatories and by Automated Meteorological Data Acquisition System (AMeDAS; operated by JMA) and Environmental Sensor Network (ESN; operated by NTT DOCOMO, Inc.). These surface data were assimilated after transformed to the data at 20-m height. Radar data consist of radial velocities observed by the Meteorological Research Institute advanced C-band solid-state polarimetric radar (MACS-POL) and three operational C-band Doppler radars in Kashiwa city and at Haneda and Narita airports, and the amount of rainwater estimated from reflectivity and specific differential phase of MACS-POL. These radar data were assimilated after interpolated to the model grid points of inner LETKF on the plan position indicator surface at each elevation angle. To predict LMCs in supercells, the downscaling ensemble forecasts with a 350-m horizontal resolution were performed. The inner-LETKF analyses of 32 members and their ensemble mean at 1100 JST 6 May 2012 and their forecasts were used as the initial and boundary conditions of the

ensemble forecasts. Furthermore, realistic strong tornadoes were predicted with the higher-resolution downscaling ensemble forecasts with a 50-m horizontal resolution, where the 33-member ensemble forecasts with a 350-m horizontal resolution from 1110 to 1210 JST 6 May 2012 were used as the initial and boundary conditions.

In all 33 members of the ensemble forecasts with a 350-m horizontal resolution, strong LMCs (defined as maximum vertical vorticity at 0.8-km height $\zeta^{(\mathrm{LMC})} > 0.03\ \mathrm{s}^{-1}$) were successfully predicted near the path of the actual tornado. However, the strength of the predicted LMC, $\zeta_{\mathrm{MAX}}^{(\mathrm{LMC})}$, defined as a 20-min moving average of $\zeta^{(\mathrm{LMC})}$ around the time of the maximum $\zeta^{(\mathrm{LMC})}$ had a large spread among the ensemble members. Hence, the sensitivities of $\zeta_{\mathrm{MAX}}^{(\mathrm{LMC})}$ to variables at the time of maximum $\zeta^{(\mathrm{LMC})}$ and at 1100 JST were clarified by an ensemble-based sensitivity analysis (ESA), where inclinations of regression lines of $\zeta_{\mathrm{MAX}}^{(\mathrm{LMC})}$ and variables at each grid were regarded as sensitivities. The ESA showed that the sensitivities to southerly wind below 1-km height on the forward right side of the storm and to water vapor below 1-km height on the rear side of the storm at 1100 JST were especially large. Therefore, the LMCs are considered to be intensified by low-level convergence on the forward side of the storm and by low-level water vapor on the rear side of the storm.

Some members of the ensemble forecasts with a 50-m horizontal resolution successfully predicted strong vortices, where maximum vertical vorticity at 30-m height $\zeta^{(\mathrm{TOR})}$ exceeded 1.0 s^{-1}. If tornadoes are defined as vortices having $\zeta_{\mathrm{MAX}}^{(\mathrm{TOR})} > 1.0\ \mathrm{s}^{-1}$, where $\zeta_{\mathrm{MAX}}^{(\mathrm{TOR})}$ is a 5-min moving average of $\zeta^{(\mathrm{TOR})}$ around the time of the maximum $\zeta^{(\mathrm{TOR})}$, seven of 33 members produced tornadoes. To clarify the mechanism of tornadogenesis, backward trajectories of the parcels around the point of $\zeta^{(\mathrm{TOR})} > 0.6\ \mathrm{s}^{-1}$ for several members of largest $\zeta_{\mathrm{MAX}}^{(\mathrm{TOR})}$ were obtained and the vorticity budget, changes of the circulations, and their generation terms were examined. Vorticity budget analyses show that frictionally generated crosswise vorticity was mainly transformed to the vertical vorticity. Furthermore, circulation analyses show that the changes of the circulations of the vortices were caused more dominantly by the friction terms than by the baroclinic terms. However, the friction terms did not necessarily contributed to increase the circulations and $\zeta_{\mathrm{MAX}}^{(\mathrm{TOR})}$ was not closely related to changes of circulation by friction and baroclinic terms. Therefore, generation terms of vorticity and circulations of the vortices near the surface were changeable and do not seem to be essential for tornadogenesis.

To clarify essential factors for tornadogenesis, we produced the composite fields with respect to the point and time of the maximum $\zeta^{(\mathrm{TOR})}$, and calculated correlations between $\zeta_{\mathrm{MAX}}^{(\mathrm{TOR})}$ and mesocyclone-scale variables in these composite fields. The results show that $\zeta_{\mathrm{MAX}}^{(\mathrm{TOR})}$ were strongly correlated to mesocyclone-scale maximum vertical vorticity ζ_{max} at 1-km height and to water vapor mixing ratio $\mathrm{QV}_{\mathrm{mean}}$ averaged below 100-m height at several minutes before the time of the maximum $\zeta^{(\mathrm{TOR})}$. On the other hand, correlation to potential temperature was not significant. Importance of ζ_{max} at about 1-km height for tornadogenesis is explained by stronger VPPGF below the LMC, which is associated with negative perturbation pressure. Importance of near-surface $\mathrm{QV}_{\mathrm{mean}}$ is explained by weaker negative buoyancy above lifted condensation level (LCL), stronger positive buoyancy above level of free convection (LFC), and stronger VPPGF due to vertical buoyancy gradient near LCL. In the ensemble forecasts of this study, the necessary conditions of ζ_{max} at 1-km height and $\mathrm{QV}_{\mathrm{mean}}$ averaged below 100-m height for tornadogenesis at three minutes before the time of the maximum $\zeta^{(\mathrm{TOR})}$ are $\zeta_{\mathrm{max}} > 0.077\ \mathrm{s}^{-1}$ and $\mathrm{QV}_{\mathrm{mean}} > 10.6\ \mathrm{g\ kg}^{-1}$, respectively, and the sufficient condition is "$\zeta_{\mathrm{max}} > 0.1\ \mathrm{s}^{-1}$

and $\mathrm{QV_{mean}} > 10.7\ \mathrm{g\ kg^{-1}}$."

In this study, ensemble forecasts of an observed supercell tornado and ensemble-based analyses were performed for the first time, and clarified the following three points: (i) Low-level convergence on the forward side of the storm and low-level water vapor on the rear side of the storm play an important role in intensifying LMCs. (ii) Strong LMCs at about 1-km height and near-surface humid air are essential factors for tornadogenesis. (iii) The generation processes of the horizontal vorticity to be tilted into vertical vorticity of tornadoes can be due to both the surface friction and the baroclinity, but are not essential for determining whether tornadoes are generated or not. The conclusions (i) and (ii) are consistent with the mechanisms of the low-level mesocyclogenesis suggested in the recent studies. Because strong LMCs have more potential for tornadogenesis, larger-scale low-level convergence and water vapor, which intensify LMCs, are also important factors for tornadogenesis. In fact, the strong LMC was not predicted accurately when either surface or radar data were not assimilated. This means that improvement of low-level variables through assimilating dense surface and radar data was essential for successful forecasts of LMCs and associated tornadoes. The conclusion (iii) was firstly clarified in this study, and implies that the high-resolution forecasts resolving tornado vortices may not be necessarily required for improving tornado forecasts.

Contents

1. Introduction

1.1. Supercell tornadoes

Tornadoes are violently rotating columns of air extending from the cumuliform cloud to the surface. Their typical diameters and vertical vorticities are $O(10^{-1})$ km and $O(1)$ s^{-1}, respectively, near the surface. Extremely strong gusty winds due to tornadoes cause severe damage to buildings and human life. Most of strong tornadoes are generated in supercells (Browning 1964): a special type of convective storms with persistent mesocyclones, which are rotating updrafts having diameters of $O(1)$ km and vertical vorticities of $O(10^{-2})$ s^{-1}. Tornadoes generated in supercells are hereafter called "supercell tornadoes." Although a considerable fraction of tornadoes detected in Japan were not associated with supercells[1], strong tornadoes ranked EF2 or stronger on the EF-scale[2] (Table 1.1) are often generated in supercells (Markowski and Richardson, 2010). Hence, it is important to understand mechanisms of supercell tornadogenesis for improving forecasts for tornadoes and mitigating their disasters.

In this chapter, a review of the processes and mechanisms of supercell tornadogenesis is presented in section 1.2. Section 1.3 introduces data assimilation and ensemble forecasts, which are useful for realistically reproducing supercell tornadoes with numerical simulations and accurately analyzing the tornadogenesis. Section 1.4 summarizes motivation and structure of this thesis.

1.2. Mechanism of supercell tornadogenesis

1.2.1. Midlevel mesocyclogenesis

Supercells are known to develop in an environment with strong vertical wind shear and unstable stratification (Weisman and Klemp 1982). In such an environment, a pair of midlevel (above 1-km height) mesocyclone (MMC) and mesoanticyclone (MMAC) are generated through tilting horizontal vorticity associated with an environmental vertical wind shear (e.g., Klemp 1987; Figs. 1.1a and 1.1b). Rotunno and Klemp (1982) theoretically explained that streamwise horizontal vorticity associated with an environmental veering (backing) shear tends to enhance MMCs (MMACs) with the following equation:

$$p' \propto \underbrace{\left(\frac{\partial u'}{\partial x}\right)^2 + \left(\frac{\partial v'}{\partial y}\right)^2 + \left(\frac{\partial w'}{\partial z}\right)^2 + 2\left(\frac{\partial v'}{\partial x}\frac{\partial u'}{\partial y} + \frac{\partial w'}{\partial x}\frac{\partial u'}{\partial z} + \frac{\partial w'}{\partial y}\frac{\partial v'}{\partial z}\right)}_{-\nabla^2 p'_{\mathrm{NDL}}/\rho \text{ (non-linear dynamic pressure)}} + \underbrace{2\left(\frac{\partial w'}{\partial x}\frac{dU}{dz} + \frac{\partial w'}{\partial y}\frac{dV}{dz}\right)}_{-\nabla^2 p'_{\mathrm{DL}}/\rho \text{ (linear dynamic pressure)}} \underbrace{-\frac{\partial B}{\partial z}}_{-\nabla^2 p'_{\mathrm{B}}/\rho \text{ (buoyancy pressure)}} . \quad (1.1)$$

This is derived from governing equations of motion in Boussinesq approximation by taking the divergence and using an approximation that perturbation pressure p' is roughly proportional to $-\nabla^2 p'/\rho$ (ρ: density), where velocity is denoted by $\mathbf{v} = \mathbf{V}(z) + \mathbf{v}' = (U(z), V(z), 0) + (u', v', w')$, and buoyancy is B. Because the horizontal scale is small, Coriolis force and β effect are neglected. If a shear vector of the environmental wind $\mathbf{S}(z) = d\mathbf{V}/dz = (dU/dz, dV/$

[1] For example, some tornadoes are generated by horizontal shear instability without mesocyclones.
[2] Six-level (EF0–EF5) classification of wind speed estimated from damage used in the U.S., Canada, France, and so on (McDonald and Mehta 2004). It is enhanced based on F-scale (Fujita 1971) for the local features of damage (Table 1.1).

$dz, 0)$ is dominant over that of the perturbation winds, then

$$p' \approx p'_{\mathrm{DL}} \propto 2\mathbf{S} \cdot \nabla_{\mathrm{h}} w'. \tag{1.2}$$

Therefore, upshear (downshear) side of an updraft region tends to have high (low) pressure.

If an environmental vertical wind shear does not change its direction with height (horizontal vorticity is crosswise), a pair of MMC and MMAC is generated symmetrically with respect to the direction of $\mathbf{V}$ because $\mathbf{S}$ is parallel to $\mathbf{V}$. In this case, the storm is symmetrically separated into right-moving and left-moving storms because precipitation at the center and associated cold outflow tend to shift low-level convergence regions symmetrically to left and right (Fig.1.1c). When an environmental wind has veering (backing) shear, however, $\mathbf{S}$ directs to the left (right) of $\mathbf{V}$ in the lower (upper) layer (red and green arrows in Fig. 1.2) and perturbation pressure becomes asymmetric (labels H and L in Fig. 1.2). Because of this asymmetric perturbation pressure due to the veering (backing) shear, upward (downward) dynamic vertical perturbation pressure gradient force (VPPGF) is generated in right-moving (left-moving) storms (yellow arrows in Fig.1.2). Therefore, the veering (backing) shear selectively intensifies right-moving (left-moving) storms and associated MMCs (MMACs).

Considering that the vertical vorticity of MMCs is produced through tilting horizontal vorticity of the environmental wind by the storm updraft, Davies-Jones et al. (1990) proposed that storm-relative environmental helicity (SREH) is a useful parameters for estimating the production of vertical vorticity through the tilting horizontal vorticity associated with environmental veering shear. SREH at 0–z km height is defined as

$$\mathrm{SREH} = \int_0^z \{\mathbf{S}(z') \times [\mathbf{V}(z') - \mathbf{C}]\} \cdot \mathbf{k} dz' \,, \tag{1.3}$$

where $\mathbf{k}$ is the vertical unit vector and $\mathbf{C}$ is the moving vector of the storm. It is given by vertically integrated streamwise vorticity multiplied by storm-relative wind.

Another useful parameter for estimating potential for supercell storms is convective available potential energy (CAPE), which gives potential intensity of convective updrafts. CAPE is defined as

$$\mathrm{CAPE} = \int_{\mathrm{LFC}}^{\mathrm{EL}} g \frac{T_{vp}(z) - T_v(z)}{T_v(z)} dz \,, \tag{1.4}$$

where $T_v(z)$ is the virtual temperature at height z, $T_{vp}(z)$ is the virtual temperature of the air parcel adiabatically lifted to height z, EL is the equilibrium level of the parcel, LFC is the level of free convection of the parcel, and $g = 9.8\ \mathrm{m\ s^{-2}}$ is the gravitational acceleration. CAPE is the energy of the parcel obtained from buoyancy, which is largely affected by initial temperature and water vapor of the parcel, and gives a measure for the maximum vertical velocity once convection is initiated. When both CAPE and SREH are large, atmospheric fields are favorable for midlevel mesocyclogenesis.

1.2.2. Low-level mesocyclogenesis

It is known that the presence of a low-level (below 1-km height) mesocyclones (LMCs) raises potential for tornadogenesis. However, the presence of MMCs does not assure the occurrence of LMCs because tilting midlevel

environmental horizontal vorticity by an updraft does not lead to an increase in low-level vertical vorticity. The genesis mechanism of LMCs, which is important for tornado forecasts, is different from that of MMCs.

It is argued that, without initial vertical vorticity in the lower layer, a downdraft is required for low-level mesocyclogenesis (Davies-Jones 1982; Rotunno and Klemp 1985; Wicker and Wilhelmson 1995; Adlerman et al. 1999). Markowski et al. (2002, 2003, 2008) and Straka et al. (2007) have suggested that the rear-flank downdraft (RFD) of the storm baroclinically generates horizontal vorticity, which in turn is tilted by the updraft near the rear-flank gust front (RFGF) to form LMCs (Fig. 1.3). In this mechanism of low-level mesocyclogenesis, environmental low-level vertical shear and water vapor may also play an important role. In fact, Craven and Brooks (2004) statistically clarified that storms are more tornadic in the stronger vertical wind shear at 0–1-km height and with the lower lifted condensation level (LCL) of the parcel averaged in the lowest 100 hPa.

Several results of idealized numerical experiments also support that baroclinically generated horizontal vorticity by the RFD and this vorticity tilted by the updraft are important for low-level mesocyclogenesis. Richardson et al. (2007) pointed out a gradient of vertical shear across the storm as favorable conditions for the intensification of right-moving supercells associated with strong LMCs. Markowski and Richardson (2014) showed that the strength of the cold pool is a "Goldilocks" problem for low-level mesocyclogenesis: it should be intermediate because horizontal vorticity is not generated near the surface by the downdraft in too weak cold pool and vertical vorticity is not intensified by the updraft in too strong cold pool. Parker and Dahl (2015) showed that low-level environmental vertical wind shear and the downdraft intensify vertical vorticity near the surface.

1.2.3. Tornadogenesis

Tornadoes are not necessarily generated even if MMCs and LMCs are generated (Trapp et al 2005). Therefore, the origin of vorticity and circulation of tornadoes is considered to be different from that of MMCs and LMCs. The origin of rotation of tornadoes may be clarified with simulations that resolve tornadoes. To resolve tornadoes having diameters of $O(10^{-1})$ km with a numerical model, however, huge computational resources are required. It becomes only recently possible to conduct such high-resolution simulations owing to improvement of computer performance (Mashiko et al. 2009; Schenkman et al. 2012, 2014; Mashiko 2016a, b).

Mashiko et al. (2009) succeeded in reproducing the Nobeoka city tornado in Japan, on 17 September 2006, with a model of 50-m horizontal grid interval, and showed that the origin of vorticity and circulation of the tornado was the environmental low-level streamwise vorticity associated with the Typhoon Shanshan (Fig. 1.4a). Schenkman et al. (2012, 2014) also analyzed vorticity budget about two typical supercell tornadoes generated in Oklahoma city, U.S., on 8–9 May 2007 and on 8 May 2003 with models of 100-m and 50-m horizontal grid interval, respectively, and showed that main origins of the rotation of these tornadoes were frictionally generated crosswise vorticity (Fig. 1.4b). Roberts et al. (2016) also showed that the frictionally generated crosswise vorticity can be a main origin of tornadoes with idealized numerical experiments.

Because such vorticity and circulation budget analyses are sensitive to location and timing of parcels used for the

trajectory analysis, however, the principal origin of vorticity of tornadoes has not been clarified in a satisfactory manner. Mashiko (2016b) analyzed circulation budget of the typical supercell tornado in Tsukuba city, Japan, on 6 May 2012, which was reproduced with a model of 50-m horizontal grid interval, and showed that frictionally generated circulation was the main origin of the weak vortex before developing to the tornado while baroclinically generated circulation was the main origin of the rapidly developing tornado (Fig. 1.4c). Using idealized numerical experiments, Markowski (2016) showed that the main origin of the circulation of tornadoes is changeable depending on environmental wind and the strength of the friction.

Once weak vortices are generated near the surface, they are likely to be intensified by the updraft associated with LMCs. For strong vertical vorticity of LMCs, Eq. (1.1) may be simplified to

$$p' \approx p'_{\mathrm{DNL}} \propto -\frac{1}{2}\zeta'^{2}, \tag{1.5}$$

where fluid extension, deformation, and horizontal vorticity can be neglected. This equation means that pressure drops at the centers of LMCs and non-linear dynamic VPPGF is generated below the LMCs. This non-linear dynamic VPPGF strengthens the low-level updraft and convergence near the surface, which in turn stretches weak vorticity near the surface and causes tornadogenesis (e.g., Markowski and Richardson 2014). Therefore, tornadoes are likely to be generated when LMCs are strong and are located just above the local points of maximum vertical vorticity near the surface. However, whether the strength of LMCs is the essential factor for tornadogenesis or not has not been clarified.

1.3. Data assimilation and ensemble forecasts to analyze tornadoes

Although the several mechanisms for geneses of mesocyclones and tornadoes have been suggested, important conditions for their geneses are not identified. Most of the previous studies about mesocyclogenesis and tornadogenesis are based on observations (e.g., Craven and Brooks 2004), numerical simulations of observed cases, and sensitivity studies in idealized numerical experiments by artificially eliminating effects of the friction, evaporation, and so on (e.g., Mashiko et al. 2009; Mashiko 2016b). However, it is not easy to clarify the mechanisms of mesocyclogenesis and tornadogenesis only from observations which have limited spatiotemporal resolutions. A successful simulations of observed tornadoes are useful because detailed analyses of three-dimensional data with high temporal resolution can be made. However, uncertainty in the initial and boundary conditions due to insufficient observational data makes difficult to evaluate the processes of tornadogenesis in deterministic simulations against the true processes occurring in nature. Thus, the sensitivity studies using deterministic simulations are also difficult to evaluate. Therefore, numerical experiments with more reliable initial and boundary conditions using assimilation of dense observations are desired to clarify the observed mesocyclogenesis and tornadogenesis. In addition, ensemble experiments with multiple initial and boundary conditions are also desired to find possibility of mesocyclogenesis and tornadogenesis that cannot be forecasted deterministically and what is especially important for mesocyclogenesis and tornadogenesis.

In the U.S., various kinds of dense observations around tornadoes are obtained with many instruments in field

campaigns such as VORTEX (Rasmussen et al. 1994) and VORTEX2 (Wurman et al. 2012). One of their aims is to give warnings of tornadoes based on realistic ensemble forecasts of storm features conducted with several kilometer horizontal grid intervals by assimilating such dense observations (e.g., Warn-on-forecast; Stensrud et al. 2009, 2013; Cintineo and Stensrud 2013).

In Japan, strong supercell tornadoes occur much less frequently than they do in the U.S. Once they occur, however, they can be observed by the dense surface observation network and the operational C-band radars covering the whole Japan. In particular, the supercell that spawned the tornado in Tsukuba city on 6 May 2012 was observed not only by these observational systems but also by the C-band polarimetric radar located very close to the supercell. Therefore, assimilating observational data around the tornadic supercell on 6 May 2012 is useful for clarifying the supercell tornadogenesis.

For assimilating dense observations and making initial states of ensemble experiments, three-demensional variational method (3D-VAR, Sasaki 1958) and ensemble Kalman filter (EnKF, Kalman 1960; Evensen 1994) are commonly used. These two methods are explained in the following subsections.

1.3.1. Variational method (3D-VAR, 4D-VAR)

Three-demensional variational method (3D-VAR) is one of the data assimilation methods based on the Baysian probability theory (Lorenc 1986). In 3D-VAR, the analysis $\mathbf{x}^a$ is solved by minimization of cost function J defined as

$$J = \frac{1}{2}(\mathbf{x}^a - \mathbf{x}^f)^T \mathbf{B}^{-1}(\mathbf{x}^a - \mathbf{x}^f) + \frac{1}{2}[H(\mathbf{x}^a) - \mathbf{y}]^T \mathbf{R}^{-1}[H(\mathbf{x}^a) - \mathbf{y}], \tag{1.6}$$

where $\mathbf{x}^f$ is the first guess obtained by forecast from the previous analysis and $\mathbf{y}$ is the observation. H is the observation operator to convert values in the model space corresponding to those in the observation space (interpolation to observation point when $\mathbf{x}^a$ and $\mathbf{y}$ are same variables). $\mathbf{B}$ and $\mathbf{R}$ are background and observation error covariance matrices, respectively. Non-diagonal components of $\mathbf{R}$ (error covariance between different observations each other) are usually set to zero for simplification. The first and second terms in right hand side (rhs) of Eq. (1.6) (called background and observation terms) are small when the analysis is close to the first guess and the observation, respectively. Minimization of J is conducted by making

$$\nabla J = \mathbf{B}^{-1}(\mathbf{x}^a - \mathbf{x}^f) + \mathbf{H}^T \mathbf{R}^{-1}[H(\mathbf{x}^a) - \mathbf{y}] \tag{1.7}$$

close to zero with conjugate gradient method (e.g., Navon and Legler 1987), quasi-Newton method (e.g., Nocedal 1980), and so on, where $\mathbf{H}$ is tangent linear H [Jacobian matrix of $H(\mathbf{x}^f)$].

3D-VAR assimilation is useful for forecasting supercell storms easily with the high-resolution model. In 3D-VAR, however, analyses based on flow-dependent (varying according to the atmospheric fields) $\mathbf{B}$ cannot be accomplished because the components of $\mathbf{B}$ are climatologically determined. Moreover, correlations between variables in non-diagonal components of $\mathbf{B}$ are usually set to zero because it is difficult to estimate them. In this case, assimilation of radar reflectivity does not correct atmospheric fields except water contents. Therefore, “cloud analysis,” which directly

corrects atmospheric fields with radar reflectivity, has been often used together with 3D-VAR for forecasting the tornadic supercells: for example, supercells in Fort Worth, Texas, on 23 March 2000 (Hu et al. 2006a, b), in Oklahoma in 4–5 May 2003 (Hu and Xue 2007; Xue et al. 2014), in Greensburg, Kansas, on 4–5 May 2007 (Stensrud and Gao 2010), and in Oklahoma on 9 May 2007 (Schenkman et al. 2011a, b, 2012). In particular, Xue et al. (2014) and Schenkman et al. (2011b, 2012) succeeded to reproduce tornado-like vortices with the experiments of 100-m and 50-m horizontal grid intervals, respectively, where initial conditions were made by 3D-VAR and cloud analysis.

In four-demensional variational method (4D-VAR, Sasaki 1969, 1970; Thompson 1969), which is the extension of 3D-VAR, observations at different time periods in the analysis window are assimilated simultaneously with flow-dependent $\mathbf{B}$. However, huge cost is required to develop the tangent linear forecast model, which is used to calculate flow-dependency of $\mathbf{B}$. Furthermore, if the forecast model is strongly non-linear, flow-dependency of $\mathbf{B}$ is not accurately calculated with the tangent linear model. Therefore, there are few studies to make high-resolution initial states with 4D-VAR. In fact, Caya et al. (2005) have shown that EnKF can produce better analyses than 4D-VAR after several assimilation cycles in observation system simulation experiments (OSSEs) using radar observations of a supercell storm.

1.3.2. Ensemble Kalman filter

Ensemble Kalman filter (EnKF) makes flow-dependent analyses more efficiently for forecasting strongly non-linear phenomena, such as supercell tornadoes, with linear minimum variances estimation. Using $H(\mathbf{x}^a) \approx H(\mathbf{x}^f) + \mathbf{H}(\mathbf{x}^a - \mathbf{x}^f)$ in 3D-VAR, $\nabla J = 0$ can be solved explicitly as

$$\mathbf{x}^a = \mathbf{x}^f + \mathbf{K}[\mathbf{y} - H(\mathbf{x}^f)]\,, \tag{1.8}$$

$$\mathbf{K} = \left(\mathbf{B}\mathbf{H}^T\mathbf{R}^{-1}\mathbf{H} + \mathbf{I}\right)^{-1}\mathbf{B}\mathbf{H}^T\mathbf{R}^{-1} = \mathbf{B}\mathbf{H}^T\left(\mathbf{H}\mathbf{B}\mathbf{H}^T + \mathbf{R}\right)^{-1}, \tag{1.9}$$

where $\mathbf{K}$ is called Kalman gain. In EnKF, on the other hand, analyses are solved by Eq. (1.8) and

$$\mathbf{K} = E[\delta\mathbf{x}^f(\delta H^f)^T]\{E[\delta H^f(\delta H^f)^T] + \mathbf{R}\}^{-1}\,, \tag{1.10}$$

where $\delta\mathbf{x}^f$ and δH^f are ensemble perturbations of $\mathbf{x}^f$ and $H(\mathbf{x}^f)$, respectively. $\mathbf{x}^f$ and $H(\mathbf{x}^f)$ are ensemble means. E is a matrix consisting of expected values calculated with ensemble forecasts. In these formulations, components of $\mathbf{B}$ are flow-dependent because $E[\delta\mathbf{x}^f(\delta H^f)^T]$ and $E[\delta H^f(\delta H^f)^T]$ calculated with ensemble forecasts are used instead of $\mathbf{B}\mathbf{H}^T$ and $\mathbf{H}\mathbf{B}\mathbf{H}^T$, respectively. Because this ensemble-based analysis does not use the tangent linear forecast model, the EnKF system is simpler than the 4D-VAR one. However, enormous computational resources are required for ensemble forecasts by a number of members to calculate $E[\delta\mathbf{x}^f(\delta H^f)^T]$ and $E[\delta H^f(\delta H^f)^T]$ accurately. Therefore, "covariance localization," where the covariance between two points distant each other is artificially made smaller, and "covariance inflation," where the ensemble perturbation is artificially made larger, are usually used to suppress sampling error and underestimation of the forecast error because of limited ensemble members in EnKF.

One of the advantages of EnKF is that ensemble perturbations $\delta\mathbf{x}^a$ based on the analysis error covariance matrix,

$$E[\delta\mathbf{x}^a(\delta\mathbf{x}^a)^T] = E[\delta\mathbf{x}^f(\delta\mathbf{x}^f)^T] + \mathbf{K}E[\delta H^f(\delta\mathbf{x}^f)^T], \quad (1.11)$$

are explicitly calculated with the perturbed observation method (Burgers et al. 1998) or square root filters (Anderson 2001; Whitaker and Hamill 2002; Hunt et al. 2007). Ensemble forecasts with initial perturbations made by these methods are used for the first guess of the next assimilation cycle. For example, EnKF with square root filters were used to assimilate dense observations for improving severe weather forecasts in Snyder and Zhang (2003), Zhang et al. (2004), Dowell et al. (2004, 2011), Caya et al. (2005), Tong and Xue (2005), Xue et al. (2006), Dawson et al. (2012), Marquis et al. (2012, 2014), Snook et al. (2012, 2015), Yussouf et al. (2013a, b), Tanamachi et al. (2013), Putnum et al. (2014), and so on.

Although larger computational resources are generally required in EnKF assimilation than in 3D-VAR assimilation, EnKF assimilation can produce dynamically balanced analyses of supercell storms with the flow-dependent $\mathbf{B}$ estimated by ensemble forecasts. Furthermore, EnKF can make multiple atmospheric fields within the range of analysis error through assimilation of dense observations around the tornadoes. Therefore, ensemble forecasts from EnKF analyses accomplish ensemble-based analyses about tornadogenesis, which statistically clarify the relationship between tornadoes and the surrounding environment and also examine what is especially important for tornadogenesis [e.g., ensemble-based sensitivity analyses (ESA), Ancell and Hakim 2007; Torn and Hakim 2008].

In fact, Seko et al. (2015) performed ensemble-based analyses of the typical tornadic supercell generated in Japan on 6 May 2012 using 12-member ensemble experiments from EnKF analyses, and showed that low-level water vapor and vertical shear affected low-level mesocyclogenesis. However, the number of ensemble members and assimilated observations in Seko et al. (2015) were too small to do more reliable analyses.

1.4. Motivation and structure of this thesis

As reviewed above, important conditions for tornadogenesis have not been clarified well. Although it has been shown that modification of small-scale fields through assimilation of low-level dense observations helps to improve the predictability of mesocyclogenesis and tornadoegenesis, which physical variables are important to be assimilated for improving forecasts of LMCs has not been clarified. To clarify this, we conducts realistic ensemble forecasts of an LMC and a tornado with sub-kilometer horizontal grid intervals, and analyzes the results in this thesis.

The objective of this study is to clarify the conditions for strong LMCs and associated supercell tornadogenesis in more detail. Impacts of assimilating dense observations on the improvement of the prediction of LMCs and potential of warn-on-forecasts of tornadoes are also discussed. To fulfill these objectives, we conducted 33-member ensemble forecasts of the typical supercell tornado generated in Japan on 6 May 2012 by assimilating dense surface and radar observations with EnKF, and examined the sensitivities of the strength of LMCs to environmental parameters such as SREH and CAPE. The origins of vorticity and circulation of simulated tornadoes and mesocyclone-scale variables that are strongly correlated to tornadogenesis are also clarified based on the ensemble forecasts.

The rest of the thesis is structured as follows: The design of the assimilation experiment is described in chapter 2, and the results of the ensemble forecasts to clarify the mechanisms of intensification of the LMC and the tornadogenesis are presented in chapters 3 and 4, respectively. In chapter 5, conditions for tornadogenesis and potential for tornado forecasts are discussed. Finally, chapter 6 presents conclusions and remarks.

It is noted that parts of this thesis are related to the findings of the author and collaborators, which have already been published in scientific journals. Analyses of the synoptic field associated with the supercell tornado on 6 May 2012 in Seko et al. (2015) are referred to in chapter 2. The ensemble-based data assimilation method that is explained in chapters 2 and 6 is the same as that used in Yokota et al. (2016a). The ensemble forecasts of the LMC, which constitute the main parts of chapters 2 and 3 and are related to chapters 1, 5, and 6, have been described in Yokota et al. (2016b). This thesis synthesizes these works to clarify the essential conditions for supercell tornadogenesis more reliably.

Table 1.1. F-, EF-, JEF-scale wind speeds (cf., Fujita 1971; McDonald and Mehta 2004; Japan Meteorological Agency 2015). F-scale wind speed is fastest quarter-mile wind, while EF- and JEF-scale wind speeds are 3-min average.

	F-scale (m s^{-1})	EF-scale (m s^{-1})	JEF-scale (m s^{-1})
0	17–32	29–38	25–38
1	33–49	39–49	39–52
2	50–69	50–60	53–66
3	70–92	61–74	67–80
4	93–116	75–89	81–94
5	117–141	90–	95–

5 年以内に雑誌等で公表予定のため、非公開。

Fig. 1.1. Schematic illustrations of midlevel mesocyclogenesis due to tilting horizontal vorticity due to the environmental vertical wind shear. Red and blue arrows denote directions of velocity and vorticity vectors, respectively.

5 年以内に雑誌等で公表予定のため、非公開。

Fig. 1.2. Schematic illustrations of the asymmetric perturbation pressure in veering shear. Red arrows denote directions of velocity $\mathbf{V}$ and w'. Green, purple, and yellow arrows denote vertical shear vectors (of horizontal velocity) $\mathbf{S}$, horizontal gradient of the updraft $\nabla_{\mathrm{h}} w'$, and the linear dynamic VPPGF, respectively. This shows that the veering shear selectively intensifies right-moving storms and associated MMCs.

5 年以内に雑誌等で公表予定のため、非公開。

Fig. 1.3. Schematic illustrations of low-level mesocyclogenesis due to baroclinically generated vorticity that is tilted by the updraft. Red and blue arrows denote directions of velocity and vorticity vectors, respectively.

5 年以内に雑誌等で公表予定のため、非公開。

Fig. 1.4. Schematic illustrations of three possible origins of rotation of tornadoes: (a) environmental streamwise vorticity, (b) frictionally generated crosswise vorticity, and (c) baroclinically generated horizontal vorticity. Red and blue arrows denote directions of velocity and vorticity vectors, respectively.

2. Methodology

2.1. The tornadoes on 6 May 2012

In this study, we focused on three tornadoes that occurred almost simultaneously on the northern Kanto Plain at about 1230 Japan Standard Time (JST; 0900 JST corresponds to 0000 UTC) on 6 May 2012 (Japan Meteorological Agency 2012). The three tornadoes passed through Tsukuba, Chikusei, and Moka cities in order from the south, and they are hereafter called the Tsukuba, Chikusei, and Moka tornadoes, respectively. Their paths were determined by Japan Meteorological Agency (JMA) (black solid lines in Figs. 2.1–2.3). The Tsukuba, Chikusei and Moka tornadoes were ranked F3, F1 and F2, respectively, on the F-scale (Fujita 1971) by JMA. We focused particularly on the Tsukuba tornado, which caused the most severe damage of the three. It had the characteristics of a typical supercell tornado (Yamauchi et al. 2013; Mashiko 2016a, b). The damage path of the Tsukuba tornado was 17 km long and 500 m wide. It damaged about 800 houses, killed one person, and injured 37 people.

In Japan, no tornadoes have been ranked F4 or more and the number of tornadoes ranked F3 are only four between 1990 and March 2016[3]: they are the Mobara city tornado in 1990 (e.g., Niino et al. 1993), the Toyohashi city tornado in 1999 (e.g., Yoshino et al. 2002), the Saroma city tornado in 2006 (e.g., Kato and Niino 2007), and the Tsukuba tornado. These four toandoes are caused by supercells. Because there were much denser observations around the Tsukuba tornado than other three F3 tornadoes, however, the Tsukuba tornado is suitable for clarifying the mechanisms of supercell tornadogenesis in Japan.

At 0900 JST 6 May 2012, southerly winds prevailed near the surface of the Kanto Plain due to a low-pressure system centered over the Japan Sea, northwest of the Kanto Plain (Fig. 2.4a). At that time, a low-pressure system accompanying a cold air mass was located in the upper troposphere over the Japan Sea (Fig. 2.4b), and moved southeastward toward the Kanto Plain. Subsequently, band-shaped precipitation system extending from southwest to northeast over the central Japan started to develop in the western part of the Kanto Plain and moved northeastward across the Kanto Plain while developing. On the other hand, surface temperature and horizontal winds showed that a warm moist southerly flow in the southeast and a cold northerly flow in the northwest converged over the northern Kanto Plain. The warm moist flow was characterized by a water vapor mixing ratio exceeding 12 g kg^{-1}, which was supplied to the precipitation system (Meteorological Research Institute 2012). Cold advection due to the northwesterly winds in the upper troposphere and warm advection due to the southerly moist winds near the surface increased static instability and contributed to the intensification of the storm.

On the Kanto Plain, a considerable number of observations captured the structure and environment of the three tornadoes. In particular, the Meteorological Research Institute Advanced C-band Solid-state Polarimetric Radar (MACS-POL) observed the detailed structure and behavior of the tornado and its parent storm. MACS-POL has radial and azimuthal resolutions of 150 m and 0.7° (Adachi et al. 2013), and the Tsukuba tornado passed only about 15 km

[3] JMA used F-scale to estimate the strength of tornadoes until March 2016, but started to use JEF-scale (Japan Meteorological Agency 2015) from April 2016 to improve accuracy of estimation based on damage indicators and degree of damage (Table 1.1).

north of MACS-POL. The three tornadoes were generated at the southern edges of intense rainfall regions observed by MACS-POL. A region of strong horizontal shear and an associated low-level vortex observed by MACS-POL moved above the path of the Tsukuba tornado at the tip of a hook echo (southernmost solid black line in Figs. 2.1–2.3). The diameter and vorticity of this vortex, calculated from the local minimum and maximum velocities and their locations, were $O(1)$ km and $O(10^{-2})$ s^{-1}, respectively, at about 1230 JST, and they became $O(10^{-1})$ km and $O(10^{-1})$ s^{-1}, respectively, by 1250 JST (Yamauchi et al. 2013). In addition, the high-resolution surface observation network, comprising Automated Meteorological Data Acquisition System (AMeDAS; operated by JMA) and Environmental Sensor Network (ESN; operated by NTT DOCOMO, Inc.) stations, recorded the horizontal distributions of surface winds, temperature, and relative humidity on the Kanto Plain before and after the geneses of the three tornadoes. The average spatial interval of these surface observations was about 10 km (Figs. 2.1a–c).

Shoji et al. (2015) and Mashiko (2016a, b) deterministically simulated an LMC and a tornado corresponding to the Tsukuba tornado by a numerical simulation with a horizontal grid interval of 250 m and 50 m using JMA's operational mesoscale analysis. Although Shoji et al. (2015) and Mashiko (2016a, b) did not discuss the predictability of LMCs, Seko et al. (2015) simulated three LMCs corresponding to the three tornadoes and discussed their predictability by conducting ensemble experiments with a horizontal grid interval of 350 m from EnKF analyses. However, owing to model bias and inaccurate initial conditions due to the assimilation of spatially coarse conventional observations, the LMC outbreaks simulated by Seko et al. (2015) were about 45 minutes earlier than the actual outbreak, and the position of the LMC associated with the Tsukuba tornado was shifted 15–20 km north of the actual tornado.

2.2. Numerical model and data assimilation system

In this study, JMA non-hydrostatic model (JMANHM, Saito et al. 2006)[4] was used for the model of ensemble forecasts, and four-dimensional local ensemble transform Kalman filter (4D-LETKF, Hunt et al. 2004, 2007; Miyoshi et al. 2007) was used for the data assimilation. LETKF is a kind of EnKF based on Eqs. (1.8), (1.10), and (1.11), and "4D" means that observations at a plurality of times in a finite time window are assimilated together. In 4D-LETKF, analysis and analysis perturbation used for initial conditions of ensemble forecasts are given by

$$\overline{x^a_{i,t}} = \overline{x^f_{i,t}} + \sum_{j=1}^{m} \delta x^f_{ij,t} w_{ij} \tag{2.1}$$

$$\delta x^a_{ij,t} = \sum_{j_1=1}^{m} \delta x^f_{ij_1,t} T_{ij_1 j} \,, \tag{2.2}$$

where $\overline{x^{a(f)}_{i,t}}$ and $\delta x^{a(f)}_{ij,t}$ are an ensemble mean and perturbation of $x^{a(f)}_{ij,t}$, which is the analysis variable (a: analysis, f: first guess) of ensemble member $j\ (1 \le j \le m)$ at point $i\ (1 \le i \le n)$ at time slot $t\ (0 \le t \le T)$. w_{ij} and $T_{ij_1 j}$ are calculated by

[4] In this model, a hybrid terrain-following vertical coordinate system (Ishida 2007) is used. Hereafter, height (written as z^*) is given in this coordinate system.

$$w_{ij} = \sum_{j_1=1}^{m} \left[\sum_{j_2=1}^{m} \frac{1}{\lambda_{ij_2}} U_{ij_1j_2} U_{ijj_2} \sum_{t=0}^{T} \sum_{k=1}^{K} \frac{L_{ik}}{R_{k,t}} \delta H^f_{kj_1,t} \left(y_{k,t} - \overline{H^f_{k,t}} \right) \right], \tag{2.3}$$

$$T_{ij_1j} = \sqrt{m-1} \sum_{j_2=1}^{m} \frac{1}{\sqrt{\lambda_{ij_2}}} U_{ij_1j_2} U_{ijj_2}\,, \tag{2.4}$$

$$\frac{m-1}{\alpha^2} \delta_{j_1j} + \sum_{t=0}^{T} \sum_{k=1}^{K} \frac{L_{ik}}{R_k} \delta H^f_{kj_1,t} \delta H^f_{kj,t} = \sum_{j_2=1}^{m} \lambda_{ij_2} U_{ij_1j_2} U_{ijj_2}\,, \tag{2.5}$$

where $y_{k,t}$ is an observation at point k $(1 \le k \le K)$ at time slot t. $\overline{H^f_{k,t}}$ and $\delta H^f_{kj,t}$ are ensemble mean and perturbation of the first guess converted to the value corresponding to observation $y_{k,t}$ by the observation operator. $R_{k,t}$ is error variance of observation $y_{k,t}$. λ_{ij_2} and $\left(U_{i1j_2}, \ldots, U_{imj_2}\right)$ are the j_2th eigenvalue and eigenvector of an $m \times m$ matrix: (j_1, j) component is the left hand side of Eq. (2.5). This method to make the transformation matrix T_{ij_1j} of analysis perturbation $\delta x^a_{ij,t}$ with the eigenvalue decomposition is called "square root filter." α is the multiplicative inflation parameter to increase the underestimated forecast error perturbation (Anderson and Anderson 1999). L_{ik} is the localization factor between points i and k, defined as

$$L_{ik} = \begin{cases} \exp\left(-\dfrac{r_{ik}^2}{2\sigma^2} \right) & (r_{ik} \le r_{\max}) \\ 0 & (r_{ik} > r_{\max}) \end{cases}, \tag{2.6}$$

where r_{ik} is the distance between points i and k (**R**-localization). σ and $r_{\max}$ are constants and σ is called "localization length" (cf. Miyoshi et al. 2007). Eqs. (2.1)–(2.6) are the equations of EnKF assimilating observations at a plurality of times with **R**-localization. If $\sigma \to \infty$, $r_{\max} \to \infty$, and $T = 0$, so that Eqs. (2.1)–(2.6) satisfy Eqs. (1.8), (1.10), and (1.11).

The resulting values of $\overline{x^a_{i,t}}$ and $\delta x^a_{ij,t}$ become the initial values for the ensemble forecasts of the next cycle. Because $\overline{x^a_{i,t}}$ and $\delta x^a_{ij,t}$ are solved at each analysis point i independently with the distance to the observation point k, the computation of LETKF can be parallelized efficiently. In this study, we used 2-scale (outer and inner) nested 4D-LETKF system (Seko et al. 2013) to assimilate observations with smaller spatial representativeness as well as larger one. Figure 2.5 outlines the calculation procedures and shows the computational domains of this system. The settings of the nested 4D-LETKF system are summarized in Table 2.1.

2.2.1. Outer LETKF (resolution: 15 km)

In outer LETKF, the grid interval was 15 km horizontally, and it varied vertically from 40 m near the surface to 886 m near the top of the calculation domain. The number of vertical levels was 50. For the boundary conditions, the mesoscale analysis (until 0900 JST 6 May) and the global forecast (after 0900 JST 6 May) of JMA without any ensemble perturbations were used by all members. A bulk-type single-moment cloud microphysics scheme with water vapor, cloud water, rain, cloud ice, snow, and graupel (Lin et al. 1983) and Kain-Fritsch cumulus parameterization (Kain and Fritsch 1990; Kain 2004) were adopted. A second-order turbulence closure scheme based on Nakanishi (2001) and Nakanishi and Niino (2004, 2006) was also adopted. Hourly observations of surface stations (pressure), radiosondes (horizontal winds, temperature, and relative humidity), commercial aircraft (horizontal winds and temperature), wind profiler radars

(horizontal winds), and Doppler radars [Doppler velocity and relative humidity estimated from reflectivity (Ikuta and Honda 2011; Ikuta 2012)], which are used in the mesoscale analysis of JMA (Honda et al. 2005), were assimilated in a 6-h assimilation window.

2.2.2. Inner LETKF (resolution: 1.875 km)

In inner LETKF, the grid interval was 1.875 km horizontally, which is eight times finer than that of outer LETKF. The vertical grid interval was the same as that in outer LETKF to suppress the effect of inconsistency with the horizontally coarse lateral boundary. No cumulus parameterization was used. Surface and radar data observed every 10 minutes were assimilated in an hourly assimilation window. The hourly 32-member outer-LETKF analyses and forecasts were used for the boundary conditions of the 1-h inner-LETKF ensemble forecasts. Surface observations consisted of horizontal winds, temperature, and relative humidity observed at Meteorological Observatories and by AMeDAS and ESN. Radar observations consisted of radial velocity observed by MACS-POL and three operational C-band Doppler radars, in Kashiwa city and at Haneda and Narita airports (hereafter, the Kashiwa, Haneda, and Narita radars, respectively) and the amount of rainwater estimated by MACS-POL. The methods used to assimilate surface and radar observations are explained in subsections 2.3.1 and 2.3.2, respectively.

Only in making the analysis at 1100 JST 6 May 2012, observations from 1100 to 1200 JST were assimilated in addition to those before 1100 JST with an ensemble Kalman smoother (EnKS; Kalnay et al. 2007; Yang et al. 2009), which is a simple extension of EnKF in a time direction because in the LETKF formulation any time in the assimilation window can be an analysis time. In EnKS, $\overline{x_{i,0}^a}$ and $\delta x_{ij,0}^a$ in Eqs. (2.1) and (2.2) (start of the assimilation window) are used as the initial states for next ensemble forecasts, while $\overline{x_{i,T}^a}$ and $\delta x_{ij,T}^a$ (end of the assimilation window) are used in EnKF. With EnKS, requirements for a long spin-up time and the assimilation of observations just before the tornado outbreak are accomplished simultaneously.

2.2.3. Downscaling ensemble forecasts (resolution: 350 m)

In the downscale ensemble experiments (hereafter referred to as 350m-EXPs) used to forecast the LMC associated with the Tsukuba tornado, the grid interval was 350 m horizontally, and it varied vertically from 40 m near the surface to 609.5 m near the top of the calculation domain. The number of vertical levels was 70. A first-order turbulence closure scheme based on Deardorff (1980) was adopted, and no cumulus parameterization was used. The 32-member inner-LETKF analyses and their ensemble mean at 1100 JST 6 May 2012 and their forecasts were used as the initial and boundary conditions, respectively, for the 33 members of 350m-EXPs. Hereafter, forecast from the ensemble mean of the inner-LETKF analyses is called “350m-EXPm.” In this thesis, the mechanism of low-level mesocyclogenesis is clarified using the results of these 33 members of 350m-EXPs (Chapter 3).

2.2.4. High-resolution downscaling ensemble forecasts (resolution: 50 m)

In the high-resolution downscale ensemble experiments (hereafter referred to as 50m-EXPs) used to forecast the

Tsukuba tornado, the grid interval was 50 m horizontally, and it varied vertically from 10 m near the surface to 445 m near the top of the calculation domain. The number of vertical levels was 90. The turbulence closure scheme was same as 350m-EXPs and no cumulus parameterization was used. The 33-member ensemble forecasts of 350m-EXPs from 1110 to 1210 JST were used as the initial and boundary conditions for the 33 members of 50m-EXPs. In this thesis, the mechanism of tornadogenesis is examined with the results of these 33 members of 50m-EXPs (Chapter 4).

2.2.5. Experimental design to assimilate dense observations

Seko et al. (2015) reproduced LMCs of the supercells that spawned the several tornadoes by ensemble experiments with a horizontal grid interval of 350 m. In this study, the expetimental design was changed from that of Seko et al. (2015) to assimilate dense observation data more efficiently. The experiments in this study differ from those of Seko et al. (2015) with respect to the following points: (i) Dense surface and radar data were assimilated by inner LETKF; (ii) the number of ensemble members was increased from 12 to 32; (iii) multiplicative inflation parameters were increased from 1.1 to 1.5 in outer LETKF and from 1.1 to 1.2 in inner LETKF to increase the impact of the assimilation of the dense observations; (iv) the horizontal domain size of inner LETKF was increased from 300 km × 300 km to 450 km × 450 km to assimilate the dense surface observations in the larger domain; (v) observations assimilated by outer LETKF were not assimilated again by inner LETKF, and the inner-LETKF analyses did not affect the outer-LETKF analyses, to clarify the impact of the assimilation of the dense observations; (vi) the initial time of the 350m-EXPs was changed from 1030 to 1100 JST, and EnKS (Kalnay et al. 2007; Yang et al. 2009) was used to assimilate the dense observations near the time when the actual tornadoes were generated; (vii) the JMA global forecast was used for the boundary conditions of outer LETKF after 0900 JST 6 May 2012 to demonstrate the predictability of the LMC.

2.3. Verification of assimilation of dense observations

2.3.1. Assimilation of surface observations

Surface meteorological data directly capture the dynamic and thermodynamic characteristics of the planetary boundary layer, and these characteristics are closely related to low-level convergence and static instability. Therefore, assimilation of surface data can potentially improve the modeled state of the planetary boundary layer and associated forecasts of convective systems (Hacker and Snyder 2005; Zhang et al. 2006; Meng and Zhang 2007, 2008; Fujita et al. 2007; Ancell et al. 2011; Ha and Snyder 2014; Sobash and Stensrud 2015).

In inner LETKF, zonal and meridional winds, temperature, and relative humidity ($u_{20}, v_{20}, T_{20}, \mathrm{RH}_{20}$) at 20-m height, which is the lowest model level (Figs. 2.1a–c), were assimilated. These variables were transformed from the corresponding surface data ($u_{\mathrm{obs}}, v_{\mathrm{obs}}, T_{\mathrm{obs}}, \mathrm{RH}_{\mathrm{obs}}$) with the following equations:

$$\begin{pmatrix} u_{20} \\ v_{20} \end{pmatrix} = \frac{\ln(20.0/z_0)}{\ln(z_{\mathrm{obs}}/z_0)} \begin{pmatrix} u_{\mathrm{obs}} \\ v_{\mathrm{obs}} \end{pmatrix}, \tag{2.7}$$

$$T_{20} = T_{\rm obs} - \Gamma[(z_{\rm m} + 20.0) - (z_{\rm s} + z_{\rm obs})]\,, \tag{2.8}$$

$$\mathrm{RH}_{20} = \frac{p(z_{\rm m} + 20.0)/e_s(z_{\rm m} + 20.0)}{p(z_{\rm s} + z_{\rm obs})/e_s(z_{\rm s} + z_{\rm obs})}\mathrm{RH}_{\rm obs}\,, \tag{2.9}$$

where z_0 (Fig. 2.1d) is the roughness length of the model surface (m), $z_{\rm m}$ (Fig. 2.1d) and $z_{\rm s}$ are altitudes of the model and the actual surface, respectively, above sea level (m), $z_{\rm obs}$ is the height of the observation instruments above the surface (m), $p(z)$ and $e_s(z)$ are pressure and saturated water vapor pressure, respectively, at height z (m) of the model, $c_p = 1.01 \times 10^3$ J K^{-1} kg^{-1} is the specific heat at constant pressure, $R = 2.87 \times 10^2$ J K^{-1} kg^{-1} is the gas constant, and $\Gamma = 6.5 \times 10^{-3}$ K m^{-1} is the temperature lapse rate. ESN observations from only those sites that passed quality check procedures (u_{20} and v_{20} from 228 and T_{20} and RH_{20} from 215 of 332 total sites) were assimilated in the experiments; for details, see Appendix A.

Equation (2.7) assumes a neutrally stratified atmosphere in which vertical changes of horizontal winds are logarithmic. However, the assumption of neutral stratification is not appropriate for temperature and relative humidity because differences in their values at 20-m height between the model and the observation were mainly caused by the difference between $z_{\rm m}$ and $z_{\rm s}$. Therefore, Eqs. (2.8) and (2.9) assume a constant Γ instead of neutral stratification. Eq. (2.9) also assumes a constant water vapor mixing ratio with height.

In the present study, variables at the lowest model level (20-m height above the surface) were diagnosed from the surface observations and assimilated. This assimilation method is different from that used by previous studies, in which variables at 10 or 2 m above the surface were diagnosed from model grid values to assimilate surface observations directly (e.g., Hacker and Snyder 2005; Fujita et al. 2007; Ancell et al. 2011; Ha and Snyder, 2014; Sobash and Stensrud 2015). In our method, the impacts of the assimilation of surface data observed at various heights would be on the same level. Moreover, the present study also considered the difference between $z_{\rm m}$ and $z_{\rm s}$.

Figures 2.1a–c show the distributions of ($u_{20}, v_{20}, T_{20}, \mathrm{RH}_{20}$) assimilated at 1200 JST 6 May 2012. A mesoscale cold front dividing the northwestern region from the southeastern region was analyzed near the actual paths of the tornadoes (black lines): A warm humid southerly flow prevailed south of the front, whereas a cold dry northerly flow prevailed on its northern side.

Figures 2.6a–d show histograms of observation minus forecast ($O - F$) of all surface observations during 1100–1200 JST assimilated by inner LETKF. All ($O - F$) distributions were close to Gaussian, and, although the ($O - F$) averages were not zero because of biases of the model or observations, their standard deviations were larger than the averages and close to the radiosonde observational error variances at the surface used in the JMA operational mesoscale data assimilation system (2.2 m s^{-1} for u_{20} and v_{20}, 1.3 K for T_{20}, and 10.8% for RH_{20}; Honda 2010). Therefore, we used these observational error variances in the JMA system (Honda 2010) for the surface observations in this experiment.

The observational error variances were partly caused by the assumptions of neutral stratification in Eq. (2.7) and of constant Γ and water vapor mixing ratio in Eqs. (2.8) and (2.9). Typical scales of these transformation errors caused by Eqs. (2.7)–(2.9) were estimated as the difference between Eqs. (2.7)–(2.9) and the empirical functions proposed by

Beljaars and Holtslag (1991). First, horizontal winds at 10-m height and temperature and relative humidity at 1.5-m height were obtained hourly from the 1-h forecasts of inner LETKF from 0400 to 1200 JST on 6 May. Then, the root mean square (RMS) differences of variables at 20-m height were diagnosed by both methods hourly from the 1-h forecasts. The resulting RMS differences turned out to be 0.32 m s^{-1} for u_{20}, 0.62 m s^{-1} for v_{20}, 0.47 K for T_{20}, and 3.7% for RH_{20}, and are smaller than the observational error variances given in the previous paragraph.

2.3.2. Assimilation of radar observations

Doppler radar data assimilation is also useful for improving forecasts of convective systems because distributions of Doppler velocity and reflectivity observed by radar contain information on the structure and development of convective systems (Snyder and Zhang 2003; Zhang et al. 2004; Dowell et al. 2004, 2011; Caya et al. 2005; Tong and Xue 2005; Xue et al. 2006, 2014; Hu et al. 2006a, b; Hu and Xue 2007; Stensrud and Gao 2010; Schenkman et al. 2011a, b; Dawson et al. 2012; Marquis et al. 2012, 2014; Snook et al. 2012, 2015; Yussouf et al. 2013a, b; Tanamachi et al. 2013; Putnam et al. 2014). Although polarimetric radar information also has large potential to improve short-term forecasts of convective systems, their assimilation does not necessarily improve forecasts because quantitative forecasting of cloud microphysics is difficult (Jung et al. 2008a, b, 2010a, b; Li and Mecikalski 2010, 2012, 2013).

In inner LETKF, radial velocity V_R (m s^{-1}) observed by four radars (Fig. 2.2), and reflectivity Z (dBZ) (Fig. 2.3a) and specific differential phase K_{DP} (° km^{-1}) observed by MACS-POL were assimilated. V_R was obtained by the dual pulse repetition frequency technique (Dazhang et al. 1984) and dealiased by the hybrid multiple pulse-repetition interval method (Yamauchi et al. 2006). K_{DP} is defined as

$$K_{DP} = \frac{1}{2}\frac{\partial \phi_{DP}}{\partial r}, \tag{2.10}$$

where r is the distance from the radar, and ϕ_{DP} is the differential phase. Because the observed ϕ_{DP} (Fig. 2.3b) is noisy (Sachidananda and Zrnic 1986, 1987; Chandrasekar et al. 1990; Hubbert and Bringi 1995), the present study obtained K_{DP} after taking a 6-km moving average of ϕ_{DP} in the radial direction. The backscatter differential phase included in the observed ϕ_{DP}, which is caused by large raindrops or small melting hail (Hubbert and Bringi 1995; Carey et al. 2000; Tabary et al. 2009; Borowska et al. 2011; Tromel et al. 2013), was ignored because the observed ϕ_{DP} until 1200 JST increased almost monotonically in the radial direction, even when the backscatter differential phase was not removed.

Because the radar data were not uniformly distributed, we adopted the "superobservation" method for the radar data assimilation: uniform data of V_R, Z, and K_{DP} were produced by interpolation to the model grid points of inner LETKF within a 1-km influence radius (Cressman 1959; Seko et al. 2004) on the plan position indicator surface at each elevation angle. Data for elevation angles larger than 5.4° were not used (cf., Seko et al. 2004) because (i) vertical air motion and hydrometeor fall speeds at high elevation angles cannot be ignored and (ii) Z and K_{DP} above the environmental 0ºC level, which were observed at high elevation angles, cannot be caused by rainwater only.

In this study, Z and K_{DP} were not directly assimilated, but rainwater, Q_R, retrieved from Z and K_{DP}, was

assimilated (cf. Kawabata et al. 2011). To retrieve Q_R (g m^{-3}) from Z (dBZ) and K_{DP} (° km^{-1}), we used equations

$$Q_{RZ}\ (\mathrm{g\ m^{-3}}) = 10^{(Z-43.1)/17.5} \tag{2.11}$$

(Sun and Crook 1997) and

$$Q_{RK}\ (\mathrm{g\ m^{-3}}) = 3.565 \times \left(\frac{K_{DP}}{f}\right)^{0.77} \tag{2.12}$$

(Bringi and Chandrasekar 2001), respectively, where $f = 5.370$ GHz is the frequency of the MACS-POL (Adachi et al. 2013). Data with values of $Z < 15$ dBZ or $K_{DP} < 0$ were not used because such echoes may not be caused by rainwater. Although Z is affected by radar wave attenuation, Z in Eq. (2.11) was not corrected for the attenuation effect. In general, Q_{RK} is more accurate than Q_{RZ} because K_{DP} in Eq. (2.12) is less affected by the drop size distribution than Z in Eq. (2.11), and it is not affected by radar wave attenuation caused by rainfall. When K_{DP} is small, however, K_{DP} is noisier than Z because the amount of noise of K_{DP}, which is calculated by finite difference approximation of ϕ_{DP}, is not small even when K_{DP} is small (Sachidananda and Zrnic 1986, 1987; Chandrasekar et al. 1990; Hubbert and Bringi 1995). Therefore, as the equation for the retrieval of Q_R we used

$$Q_R\ (\mathrm{g\ m^{-3}}) = \begin{cases} Q_{RK} & (2\ \mathrm{g\ m^{-3}} \le Q_{RK}) \\ \alpha Q_{RK} + (1-\alpha) Q_{RZ} & (1\ \mathrm{g\ m^{-3}} \le Q_{RK} \le 2\ \mathrm{g\ m^{-3}}), \\ Q_{RZ} & (Q_{RK} \le 1\ \mathrm{g\ m^{-3}}) \end{cases} \tag{2.13}$$

where $\alpha = Q_{RK} - 1$. The quality control of Q_R mentioned above is very simple, and there is room for its improvement. However, the impact of improving the quality of Q_R is expected to be small because the impact of assimilating Q_R was not remarkable, as described later in subsection 3.2.2.

Figure 2.2 shows the distribution of V_R for the four radars, and Figs. 2.3c and 2.3d show that of Q_{RZ} and Q_R, respectively, for MACS-POL at an elevation angle of 1.0° at 1200 JST 6 May 2012. A precipitation band elongated in the meridional direction was located at around 139.5°E (Fig. 2.3d). This precipitation system was accompanied by a cyclonic shear line (red circles in Fig. 2.2), and peaks of Q_R that corresponded to the parent storms of the three tornadoes were present near the shear line (red circle in Fig. 2.3d). These three Q_R peaks are clearer than the Q_{RZ} peaks (Fig. 2.3c) because they were estimated by using K_{DP} as well as Z.

Because the $(O-F)$ distribution of V_R is close to Gaussian (Fig. 2.6e) and its standard deviation is larger than both the averages and standard deviations of u_{20} and v_{20} (Figs. 2.6a and 2.6b), a constant value of 3.0 m s^{-1} was used for the observational error variance of V_R in this experiment. Since the $(O-F)$ distribution of Q_R is far from Gaussian (Fig. 2.6f), however, we used a similar method to Koizumi et al. (2005) to set the observational error variance of Q_R. Because the absolute value of $(O-F)$ increases when Q_R is larger, the observational error variance of Q_R set in this experiment should be varied according to Q_R. However, it is expected to have a certain finite value even if Q_R is small because of the radar wave attenuation. Thus, the observational error variance of Q_R was set to $0.1Q_R$ ($Q_R \ge 1$ g m^{-3}) and 0.1 ($Q_R < 1$ g m^{-3}).

Table 2.1. Setting of the nested 4D-LETKF.

5 年以内に雑誌等で公表予定のため、非公開。

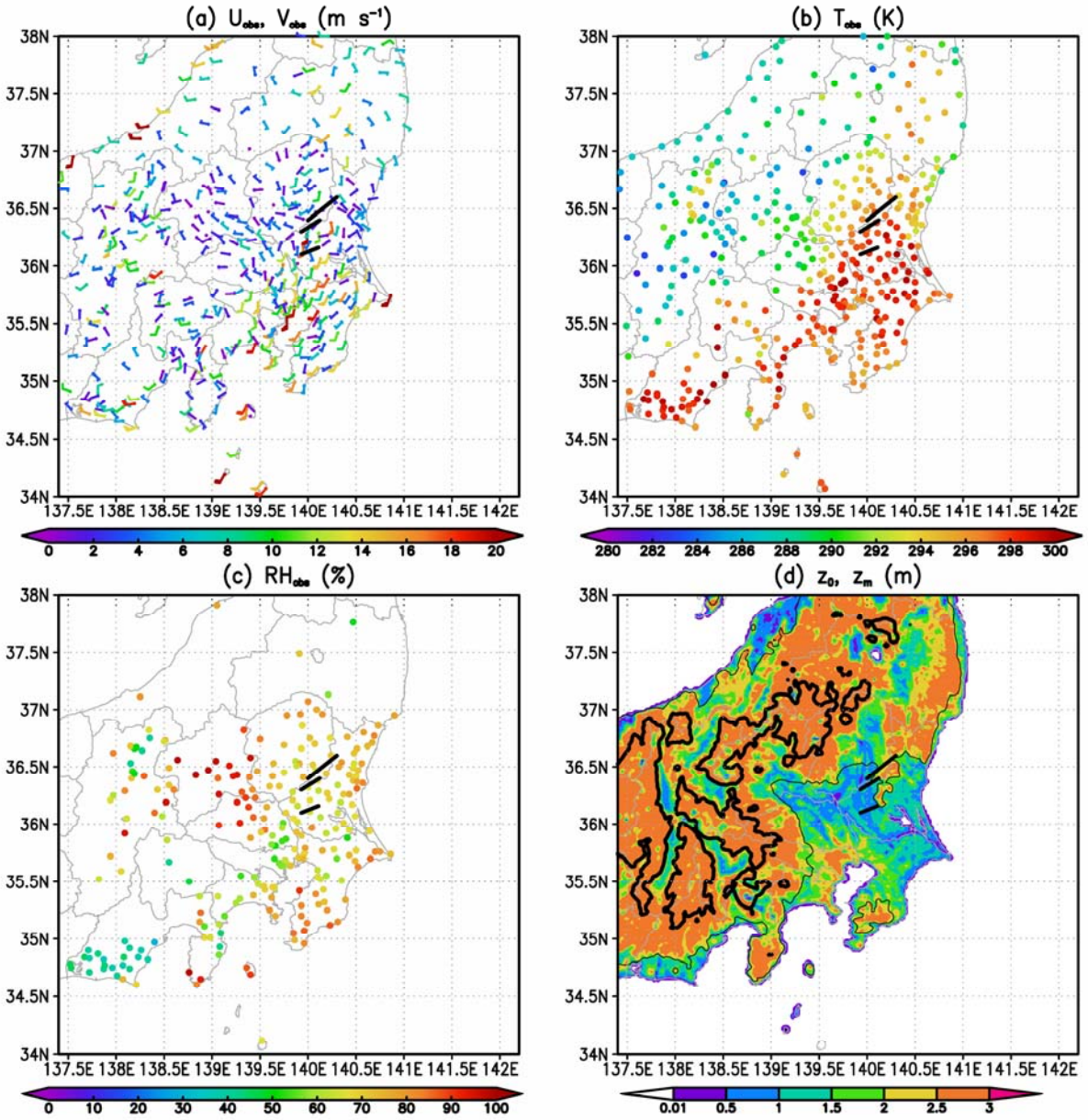

Fig. 2.1. Observations at 1200 JST used in the inner-LETKF analysis: (a) horizontal winds (m s^{-1}), (b) temperature (K), and (c) relative humidity (%) at 20-m height. Black lines denote the paths of the Tsukuba, Chikusei, and Moka tornadoes in order from south to north. (d) Roughness length of the modeled surface z_0 (color shading, m) and altitude in the model z_m (thin contours, 100 m; thick contours, 1000 m) used in Eqs. (2.7)–(2.9).

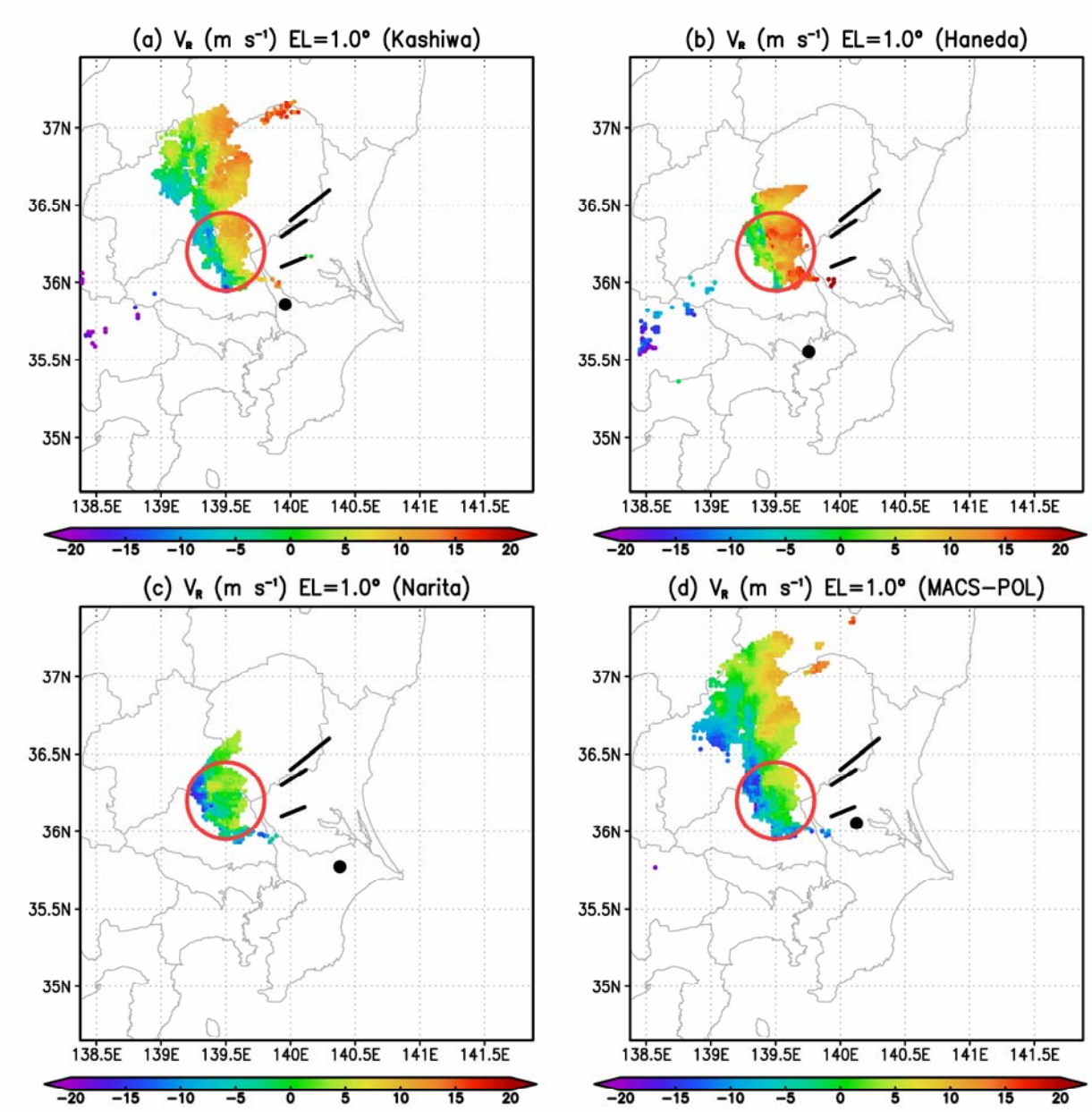

Fig. 2.2. Radial velocity (m s^{-1}) at 1.0° elevation used in the inner-LETKF analysis observed by (a) Kashiwa, (b) Haneda, and (c) Narita radars and by (d) MACS-POL at 1200 JST. The black dot denotes the position of each radar site. Black lines are as in Fig. 2.1. The red circles denote the position of cyclonic shear line.

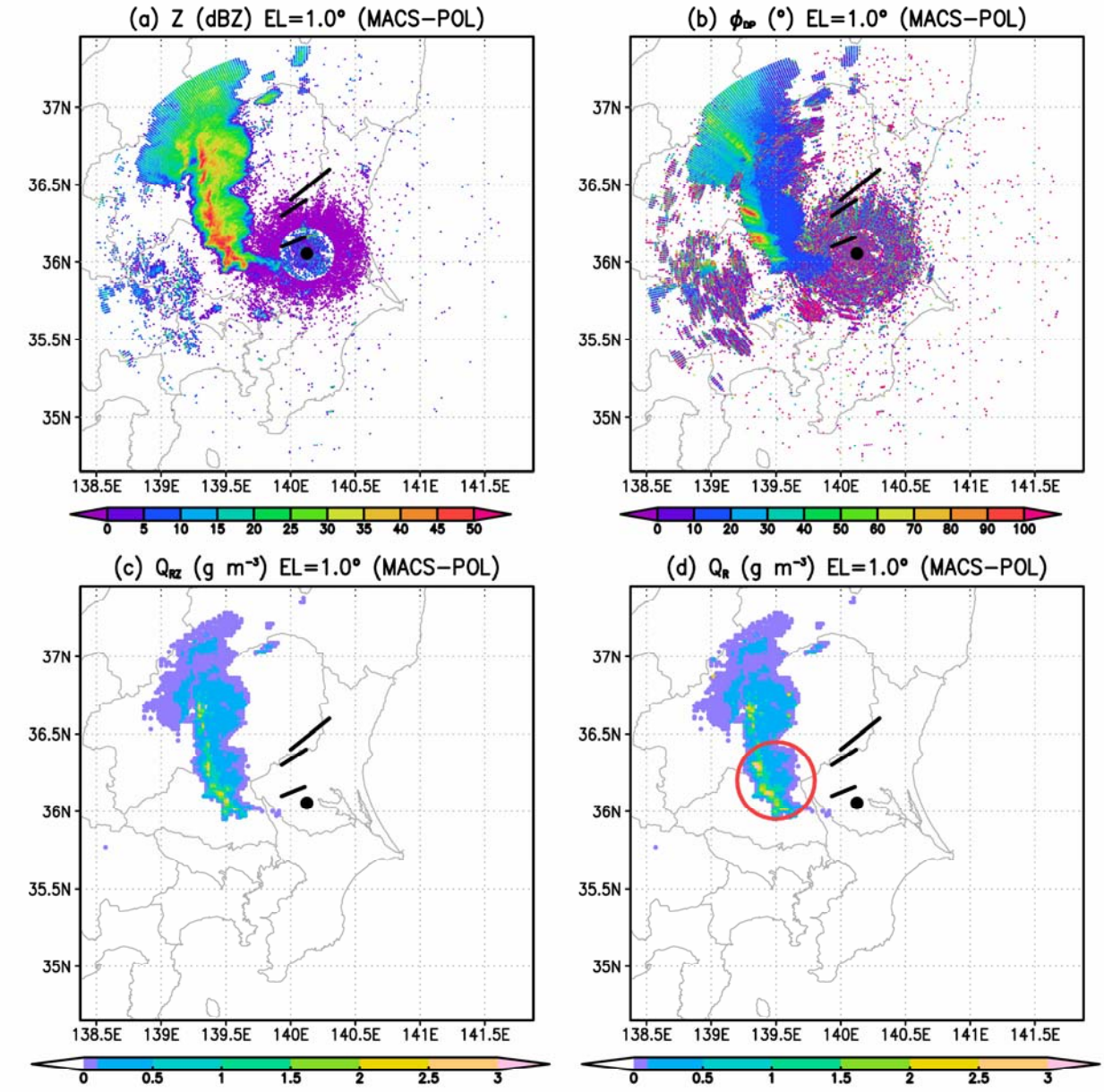

Fig. 2.3. (a) Z (dBZ) and (b) ϕ_{DP} (degrees) at 1.0° elevation observed by MACS-POL at 1200 JST, and (c) Q_{RZ} (g m^{-3}) and (d) Q_R (g m^{-3}) estimated from Z and K_{DP} at 1.0° elevation. The black dot and the black lines are as in Fig. 2.2. The red circle denotes the position of Q_R peaks.

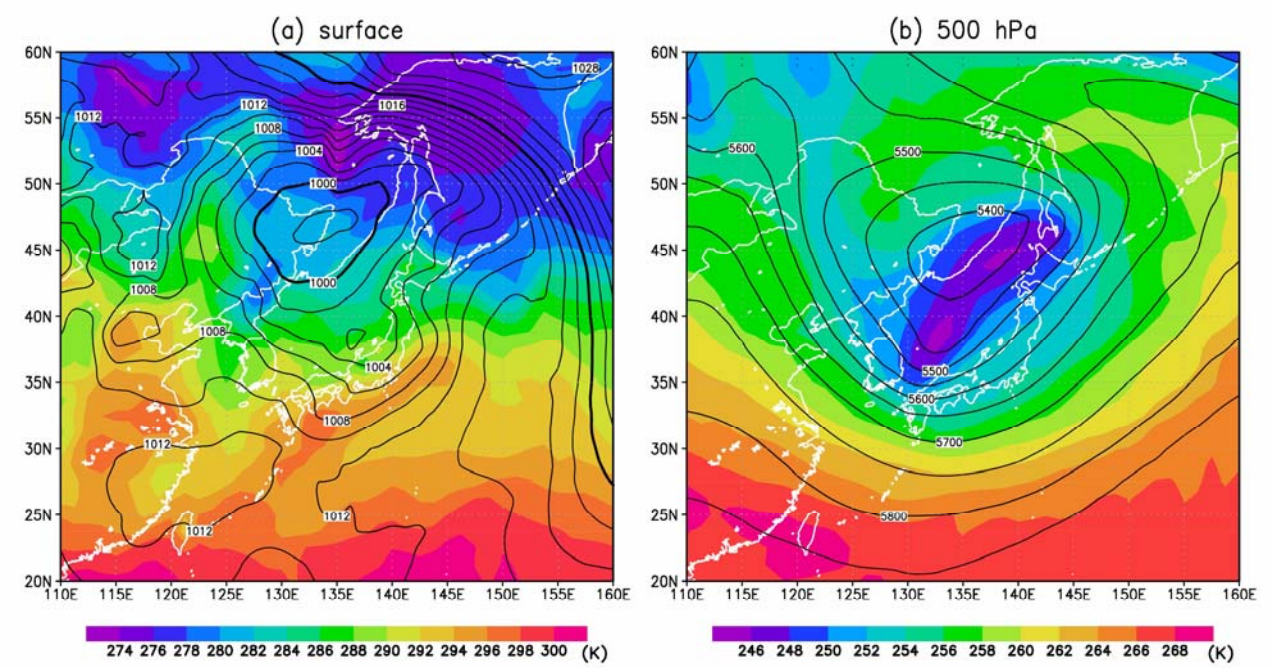

Fig. 2.4. Temperature (color shading, K) and pressure (contours, hPa) at the surface and (b) temperature (color shading, K) and height (contours, m) on the 500-hPa surface in the global analysis of JMA at 0900 JST 6 May 2012.

5 年以内に雑誌等で公表予定のため、非公開。

Fig. 2.5. Outline of the calculation procedure and the calculation domains of the nested 4D-LETKF system. Shading is altitude in each model (m).

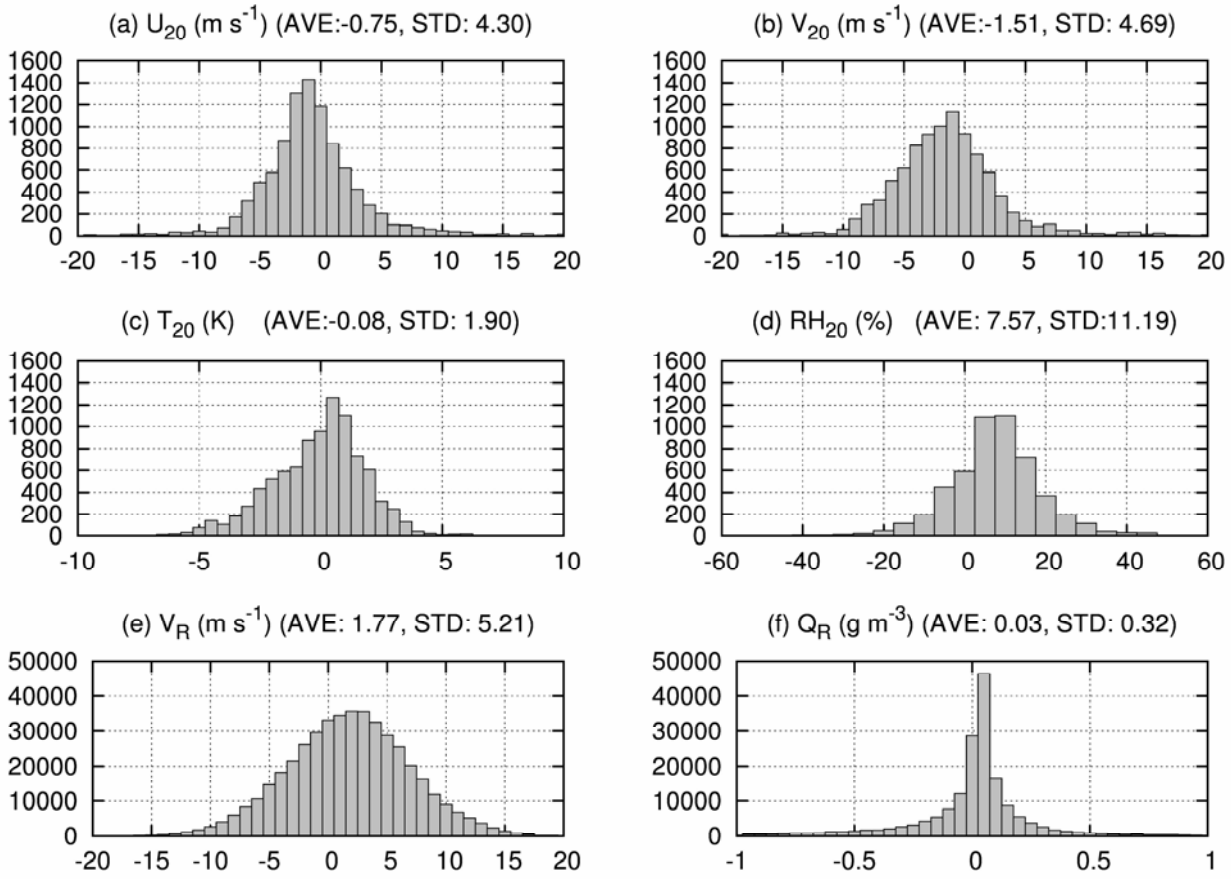

Fig. 2.6. Frequency distributions of $(O - F)$ (observation minus forecast) results of the inner-LETKF analysis during 1100–1200 JST: (a) zonal wind (m s^{-1}), (b) meridional wind (m s^{-1}), (c) temperature (K), and (d) relative humidity (%) at 20-m height, (e) radial velocity (m s^{-1}) observed by four radars, and (f) rainwater (g m^{-3}) observed by MACS-POL. "AVE" and "STD" are average and standard deviation, respectively.

3. Ensemble forecasts for low-level mesocyclogenesis

3.1. LMCs generated in the ensemble forecasts

3.1.1. Process of low-level mesocyclogenesis

350m-EXPm successfully predicted an LMC near the path of the Tsukuba tornado. Figure 3.1 shows the generation process of the predicted LMC in 350m-EXPm, where an LMC is defined as a vortex having maximum vertical vorticity at 0.8 km height, $\zeta^{(\mathrm{LMC})}$, exceeding 0.03 s^{-1}. At 1100 JST, the weak convective system that later spawned the LMC was already present (region C in Fig. 3.1a). This convective storm was a "right-moving storm": it moved to the right of the averaged horizontal wind velocity at 0–6-km height, and a strong LMC was generated at its southern edge at about 1140 JST (Fig. 3.1b). $\zeta^{(\mathrm{LMC})}$ reached a maximum at 1150 JST (Fig. 3.1c), and by this time, the region of large vertical vorticity reached from the surface to a height of over 6 km. The path of the LMC was several kilometers north of the damage path of the Tsukuba tornado and was closer to the damage path than the LMC path in Seko et al. (2015) (Fig. 3.1c and Fig. 3.2a). The LMC, which was accompanied by a hook-shaped rainwater distribution, started to dissipate after 1150 JST, and had disappeared by about 1210 JST (Fig. 3.1d).

Figure 3.3 shows the time series of $\zeta^{(\mathrm{LMC})}$ within the region 139.4°–140.2°E and 36.0°–36.4°N for the 33 members of 350m-EXPs. Temporal fluctuations of $\zeta^{(\mathrm{LMC})}$ were so large that it was not appropriate to estimate the strength of LMCs from $\zeta^{(\mathrm{LMC})}$ at a particular time. If "the strength of LMCs" is defined as the 20-min moving average of $\zeta^{(\mathrm{LMC})}$ around the time of the maximum $\zeta^{(\mathrm{LMC})}$ in each member (hereafter denoted by $\zeta_{\mathrm{MAX}}^{(\mathrm{LMC})}$), then $\zeta_{\mathrm{MAX}}^{(\mathrm{LMC})} = 0.052\ \mathrm{s}^{-1}$ at 1150 JST for a member in which the mean of the LETKF analyses at 1100 JST is used for the initial conditions (red line in Fig. 3.3). The radius of the maximum horizontal wind and maximum vorticity of the predicted LMC at that time were $O(1)$ km and $O(10^{-2})$ s^{-1}, respectively, which agree with those of the observed low-level vortex at about 1230 JST (Yamauchi et al. 2013). Note that no tornado vortices were predicted near the surface in this experiment because the horizontal grid interval of 350 m is too large to resolve tornadoes. The period with $\zeta^{(\mathrm{LMC})} > 0.04\ \mathrm{s}^{-1}$ was between 1142 and 1206 JST, and the time of maximum $\zeta^{(\mathrm{LMC})}$ (1150 JST) was about 45 minutes before the Tsukuba tornado was generated at about 1235 JST (Japan Meteorological Agency 2012; Yamauchi et al 2013); this timing is similar to that of Seko et al. (2015).

A probability that LMCs appear within 5 km between 1100 and 1300 JST is shown in Fig. 3.4 based on the 33 members of 350m-EXPs. In Fig. 3.4, the genesis points of the Tsukuba, Chikusei, and Moka tornadoes are located in areas with a probability of 50–70%, 10–30%, and 0–10%, respectively; this result confirms potential of the warn-on-forecast approach for the tornadoes (Stensrud et al. 2009, 2013; Cintineo and Stensrud 2013), and also suggests that the LMC generated at the southern edge of the storm was more easily predicted than the weak northern LMCs.

3.1.2. Environmental parameters related to the LMC

To clarify the cause of low-level mesocyclogenesis, we focused on the inner-LETKF analysis at 1100 JST, which was used for the initial condition of 350m-EXPm. Figure 3.5a shows the distribution of the ensemble mean SREH at 0–3-km height, which is a measure of the environmental vertical wind shear for the development of a right-moving storm. Here,

SREH was calculated for each member by assuming a storm motion vector based on the method of Maddox (1976): the speed of the storm was assumed to be 75% of the averaged horizontal wind velocity at 0–6 km height, and the storm was assumed to move at 30° to the right of this averaged wind. Because this storm motion vector was consistent with the motion of the simulated LMC (Figs. 3.1b–d), the distribution of SREH calculated with this storm motion vector is almost the same as that with the motion of the simulated LMC (not shown).

SREH at 0–3-km height was particularly large in the area south of the convective system [region H_+ (large SREH) in Fig. 3.5a]. This large-SREH region corresponds to the region of strong low-level southerly wind (region H_+ in Fig. 3.5c). This large-SREH field, which is favorable for development of a right-moving storm (Rotunno and Klemp 1982), is consistent with the genesis point of the LMC.

Static stability is another important factor for low-level mesocyclogenesis. Figure 3.5b shows the distribution of the ensemble mean mixed-layer CAPE (MLCAPE) of the inner-LETKF analysis at 1100 JST. MLCAPE is the maximum energy available to a lifted air parcel, which is averaged in the lowest 100 hPa, and gives an estimate of the maximum vertical velocity once convection is initiated.

In the inner-LETKF analysis at 1100 JST, the ensemble mean MLCAPE was particularly large around the path of the predicted LMC [region E_+ (large MLCAPE) in Fig. 3.5b]. This distribution is similar to that of the low-level water vapor (region E_+ in Fig. 3.5c).

3.2. Impact of assimilation of dense observations

Four additional experiments were performed to clarify the impacts of dense surface and radar data assimilation by inner LETKF on low-level mesocyclogenesis: In the first experiment, surface horizontal winds, temperature, and relative humidity were not assimilated. In the second experiment, radar data (both radial velocity and rainwater) were not assimilated. In the third experiment, only rainwater data were not assimilated. In the fourth experiment, observations during 1100–1200 JST 6 May were not assimilated. These experiments are hereafter called "NSRF" (no surface data), "NRAD" (no radar data), "NQR" (no Q_R), and "NSMT" (no smoother), respectively. The experiment with all surface and radar data as described in section 3.1 is called "CTL."

3.2.1. Assimilation of surface observations

In NSRF, in which no surface data were assimilated, an LMC still appeared at the southern edge of the storm in 350m-EXPm (Fig. 3.2b), but the precipitation distribution in CTL (Fig. 3.1c) was more similar to Q_R at 1230 JST (Fig. 3.2f) than that in NSRF (Fig. 3.2b). The LMC generated in NSRF shifted northward compared with that in CTL (Fig. 3.1c), and $\zeta_{\mathrm{MAX}}^{(\mathrm{LMC})} = 0.036\ \mathrm{s}^{-1}$ was weaker in NSRF than it was in CTL.

In the initial condition of 350m-EXPm (NSRF), SREH (Fig. 3.5d) and low-level southerly wind velocity (Fig. 3.5f) were smaller than those in CTL in the area south of the convective system (region H_+ in Figs. 3.5a and 3.5c). MLCAPE (Fig. 3.5e) and low-level water vapor (Fig. 3.5f) were also smaller along the path of the predicted LMC (region E_+ in

Figs. 3.5b and 3.5c) than those in CTL. Thus, the assimilation of surface observations contributes to an increase in the low-level southerly wind velocity in the area south of the convective system and to an increase in water vapor near the path of the predicted LMC. These increments of low-level southerly wind and water vapor improved the predictability of the LMC.

3.2.2. Assimilation of radar observations

In 350m-EXPm without radar data assimilation (NRAD), storms did not develop well compared to that in CTL (Fig. 3.1c) or observations (Fig. 3.2f), although a weak LMC was generated (Fig. 3.2c). The strength of the LMC ($\zeta_{\mathrm{MAX}}^{(\mathrm{LMC})} = 0.025\ \mathrm{s}^{-1}$) was weaker in NRAD than it was in either CTL or NSRF.

In the initial condition of 350m-EXPm (NRAD), as in NSRF, SREH (Fig. 3.5g) and low-level southerly wind velocity (Fig. 3.5i) were smaller than those in CTL in the area south of the convective system (region H_+ in Figs. 3.5a and 3.5c). These differences in SREH and southerly wind indicate that assimilation of both radar and surface data contributes to the increase in the low-level southerly wind velocity in this region. The increase in the low-level southerly wind velocity in the area south of the convective system causes larger SREH there and thus affects supercell development (cf. Schenkman et al. 2011b).

The distributions of MLCAPE (Fig. 3.5h) and low-level water vapor (Fig. 3.5i) were mostly similar to those in CTL (Figs. 3.5b and 3.5c). This similarity shows that radar data assimilation hardly affects low-level water vapor and associated MLCAPE. However, MLCAPE and low-level water vapor in some regions, especially in the southwest of the precipitation system (region e_+ in Figs. 3.5b and 3.5c), were smaller than those in CTL. These differences indicate that low-level water vapor is related to horizontal winds and rainwater, and that radar data assimilation in region e_+ increased low-level water vapor there.

Low-level water vapor in places where rainwater was assimilated as in region e_+ was greater in the inner-LETKF analysis (CTL) at 1100 JST than it was in NQR (Figs. 3.5c and 3.5l). This result suggests that rainwater assimilation affected the predicted precipitation distribution associated with low-level water vapor. However, it hardly affected other variables (Figs. 3.5j–l), and the LMC predicted in 350m-EXPm (NQR) (Fig. 3.2d) was very similar to that predicted in CTL (Fig. 3.1c). These findings indicate that the impact of rainwater assimilation on development of the LMC was not large in this experimental design.

In NSMT, the generated LMC ($\zeta_{\mathrm{MAX}}^{(\mathrm{LMC})} = 0.029\ \mathrm{s}^{-1}$; Fig. 3.2e) was weaker than that in CTL (Fig. 3.1c). Therefore, the assimilation of observations during 1100–1200 JST with EnKS, including radar data on the forward side of the storm, importantly modified the variables at 1100 JST in a reliable manner (Figs. 3.5m–o).

3.3. Ensemble-based sensitivity analysis

3.3.1. Method

In 350m-EXPm (CTL), the predicted LMC was closer to the path of the Tsukuba tornado than the LMC predicted by

Seko et al. (2015) or in NSRF, NRAD, and NSMT. The southward shift of the path of the LMC in CTL indicates that dense surface and radar data assimilation and other differences between CTL and the experiment of Seko et al. (2015), described in subsection 2.2.5, improved the LMC forecast. Using this improved forecast, we conducted an ESA to clarify further the factors important in low-level mesocyclogenesis.

The maximum and minimum strengths of the LMC among $\zeta_{\mathrm{MAX}}^{(\mathrm{LMC})}(j)$ ($j = 1, \ldots, 33$: indices of ensemble members) of the 350m-EXPs (CTL), in which the 32 LETKF analyses and their ensemble mean were used as the initial conditions, were 0.107 s^{-1} (blue line in Fig. 3.3) and 0.036 s^{-1} (green line in Fig. 3.3), respectively. We investigated the relationship between $\zeta_{\mathrm{MAX}}^{(\mathrm{LMC})}$ and environmental parameters simulated in the 350m-EXPs with the ESA.

In the ESA, the sensitivity of $\zeta_{\mathrm{MAX}}^{(\mathrm{LMC})}$ to variable x_i that characterizes the environment at each point i ($i = 1, \ldots, n$) was calculated as

$$\frac{d\zeta_{\mathrm{MAX}}^{(\mathrm{LMC})}}{dx_i} = \frac{\sum_{j=1}^{33}\left[\zeta_{\mathrm{MAX}}^{(\mathrm{LMC})}(j) - \overline{\zeta_{\mathrm{MAX}}^{(\mathrm{LMC})}}\right][x_i(j) - \overline{x_i}]}{\sum_{j=1}^{33}[x_i(j) - \overline{x_i}]^2} \tag{3.1}$$

(Ancell and Hakim 2007; Torn and Hakim 2008), where the overbar denotes the ensemble mean. This method gives quantitative information about the impacts of x_i on $\zeta_{\mathrm{MAX}}^{(\mathrm{LMC})}$ In this study, environmental parameters horizontally smoothed over 15.75 km × 15.75 km (45 × 45 grids) were used as x_i to discuss impacts of the mesoscale environment on the forecast of the strength of LMCs.

3.3.2. Sensitivities of the strength of LMCs to environmental parameters in the composite field

First, environmental parameters at the time of the maximum $\zeta^{(\mathrm{LMC})}$ were composited relative to the point of $\zeta^{(\mathrm{LMC})}$ to clarify the no-time-lag relationship between $\zeta_{\mathrm{MAX}}^{(\mathrm{LMC})}$ and these parameters. Figures 3.6a and 3.6b show the ensemble means of SREH and MLCAPE, respectively, in the composite field around the LMC (region C). SREH was large in the area south of the LMC (region H_+ in Fig. 3.6a) and small in the area north of the LMC (region H_- in Fig. 3.6a); this distribution indicates that the large SREH (the clockwise-turning vertical wind shear) south of the LMC was favorable for the development of a supercell. Similar to the distribution of SREH, the low-level southerly wind velocity was large (small) south (north) of the LMC (regions H_+ and H_- in Fig. 3.6c). This wind distribution also indicates convergence of low-level horizontal winds at the position of the LMC (region C in Fig. 3.6c). Low-level water vapor and associated MLCAPE were large southeast of the LMC (region E_+ in Figs. 3.6b and 3.6c). These large MLCAPE and water vapor values were caused by the low-level southerly winds, which blew from Tokyo Bay to the Kanto Plain.

The vectors in Fig. 3.6f show the sensitivity of the strength of LMCs to low-level zonal and meridional winds. The stronger the low-level winds were in the direction of these vectors, the stronger the LMC was. The vectors point toward the LMC, indicating that a strong low-level convergence was associated with a strong LMC. The distribution of the sensitivity to SREH, which was positive southeast of the LMC (region h_+ in Fig. 3.6d) and negative northwest of the LMC (region h_- in Fig. 3.6d), was similar to that of the sensitivity to the low-level southerly wind (regions h_+ and h_- in Fig. 3.6f).

Sensitivities to low-level water vapor and associated MLCAPE were positive in almost the whole region around the LMC, except to its west (region e_- in Figs. 3.6e and 3.6f). These positive sensitivities were larger on the low-level southwest (windward) side of the LMC (region e_+ in Figs. 3.6e and 3.6f) than in the region where the ensemble means of MLCAPE and low-level water vapor were large (region E_+ in Figs. 3.6b and 3.6c). West of the LMC, where the sensitivity to MLCAPE was negative (region e_- in Figs. 3.6e and 3.6f), low-level water vapor and associated MLCAPE were relatively small (Figs. 3.6b and 3.6c).

3.3.3. Sensitivities of the strength of LMCs to environmental parameters in the initial field

The sensitivities in the composite field described in subsection 3.3.2 resulted from the initial and boundary conditions. Clarification of the regions, in which the sensitivities of $\zeta_{\mathrm{MAX}}^{(\mathrm{LMC})}$ to the initial perturbations are large before the occurrence of the LMC, is important for forecasting the LMC. Figures 3.7a–c show the sensitivities to variables in the initial field (1100 JST), which were totally much larger than those in the composite field (Figs. 3.6d–f).

In the initial field, the sensitivity to SREH was positive on the southeastern (forward right) side of the storm, which corresponds to the area south of the path of the LMC that developed later (region h_+ in Fig. 3.7a). In contrast, the sensitivity to SREH was not large near the storm (region C in Fig. 3.7a), and it was negative on the northeastern (forward left) side of the storm (region h_- in Fig. 3.7a). The sensitivity to MLCAPE was positive in almost all of the area, and it was especially large on the southwestern (rear) side of the storm (region e_+ in Fig. 3.7b).

Sensitivities to SREH and MLCAPE correspond to those to the low-level southerly wind and water vapor, respectively (Figs. 3.7a–c), in both the initial and composite fields. These distributions of sensitivities to wind and water vapor indicate that the LMC became strong when the initial low-level horizontal winds converged toward the forward side of the storm (between region h_+ and h_- in Fig. 3.7c) and initial low-level water vapor was large on the rear side of the storm (region e_+ in Fig. 3.7c).

3.4. Discussion about low-level mesocyclogenesis

The ensemble-based sensitivities of the strength of the predicted LMCs to SREH and MLCAPE before their geneses (Figs. 3.7a and 3.7b) were larger than those when the LMCs were strongest (Figs. 3.6d and 3.6e). This result indicates that SREH and MLCAPE were highly correlated with the strength of LMCs not only when the LMCs were strongest, but also before their geneses. The larger sensitivities to SREH and MLCAPE before low-level mesocyclogenesis can be explained by the increase of the spread of SREH and MLCAPE with time in the denominator of Eq. (3.1) without a noticeable increase of the covariance of the strength of LMCs to SREH and MLCAPE in the numerator of Eq. (3.1) in the ensemble forecasts.

In the present case, the sensitivities to SREH and MLCAPE were large in the region where SREH and MLCAPE were relatively small in the initial field (regions h_+ and e_+ in Figs. 3.7a–c); this result suggests that areas with high SREH

or high MLCAPE are not necessarily the most important for the strength of LMCs. Furthermore, the sensitivities to SREH and MLCAPE, as well as their distributions, were similar to the sensitivities to the low-level southerly wind and water vapor, respectively, both before and after low-level mesocyclogenesis (Figs. 3.6d–f and 3.7a–c); these results suggest that large-scale, low-level southerly wind and water vapor played especially important roles in determining the strength of LMCs in this case.

The sensitivity to the low-level southerly wind before low-level mesocyclogenesis was positive on the forward right side with respect to the storm's direction of movement (region h_+ in Fig. 3.7c) and negative on the forward left side (region h_- in Fig. 3.7c). This sensitivity distribution shows that convergence of low-level meridional winds within the storm and high SREH on the forward right side relative to storm movement direction strengthened the predicted LMC. In a numerical model that assumes a horizontally uniform environment, an environmental wind with veering shear (i.e., high SREH) is suitable for development of a right-moving supercell (Rotunno and Klemp 1982). Richardson et al. (2007) additionally showed in idealized numerical experiments that the meridional gradient of vertical shear can intensify the supercell. The present study showed that, when horizontal inhomogeneity exists in the real atmosphere, a wide high-SREH region just on the forward right side of the storm (i.e., low-level southerly winds toward the storm's position at a later time) contributes to the strengthening of the LMC. The negative sensitivity to SREH (region h_- in Fig. 3.7a) indicates that large SREH associated with strong southerly winds in the northeast of the LMC would weaken the LMC, because low-level convergence would be weak if southerly winds were strong in the northeast of the LMC.

The sensitivity to low-level water vapor both before and after low-level mesocyclogenesis was positive in almost the whole region and was particularly large on the rear side of the storm (region e_+ in Figs. 3.6f and 3.7c). However, sensitivity to low-level potential temperature was negative (Fig. 3.8d) and correlation was weak (Fig. 3.9d) there after low-level mesocyclogenesis. When low-level water vapor is larger (Figs. 3.6f and 3.9b) and potential temperature is lower (Figs. 3.8d and 3.9d), relative humidity is higher (Figs. 3.8e and 3.9f), mixed-layer LFC (MLLFC) is lower (Figs. 3.8f and 3.9h), and the parcel is more easily lifted despite negative buoyancy in the updraft area. Therefore, these sensitivities seem to be consistent with the findings of the previous studies that tilting of baroclinically generated horizontal vorticity (Markowski et al. 2002, 2003, 2008; Straka et al. 2007) and stretching of vertical vorticity by the convection associated with large amounts of low-level water vapor behind the rear-flank gust front are important for low-level mesocyclogenesis.

The negative sensitivity to low-level water vapor and the positive sensitivity to potential temperature in the region indicated by e_- in Figs. 3.6f and 3.8d were caused by low-level dry and high potential temperature air advected from above by downdrafts in the precipitation area (Figs. 3.8a–c), which are more intense in the case of a relatively strong LMC. Although this positive sensitivity to potential temperature shows that cold pool in the RFD area tends to be weaker in the stronger LMC, correlation of the strength of the LMC to the cold pool was weak (Fig. 3.9c). Moreover, correlations of the strength of LMCs to low-level water vapor, relative humidity, and MLLFC were also weak there (Figs. 3.9a, 3.9e, and 3.9g). These results are consistent with the idealized experiments which showed that a cold pool in the strong supercell has to be neither too strong nor too weak for intensifying LMCs (Markowski and Richardson 2014).

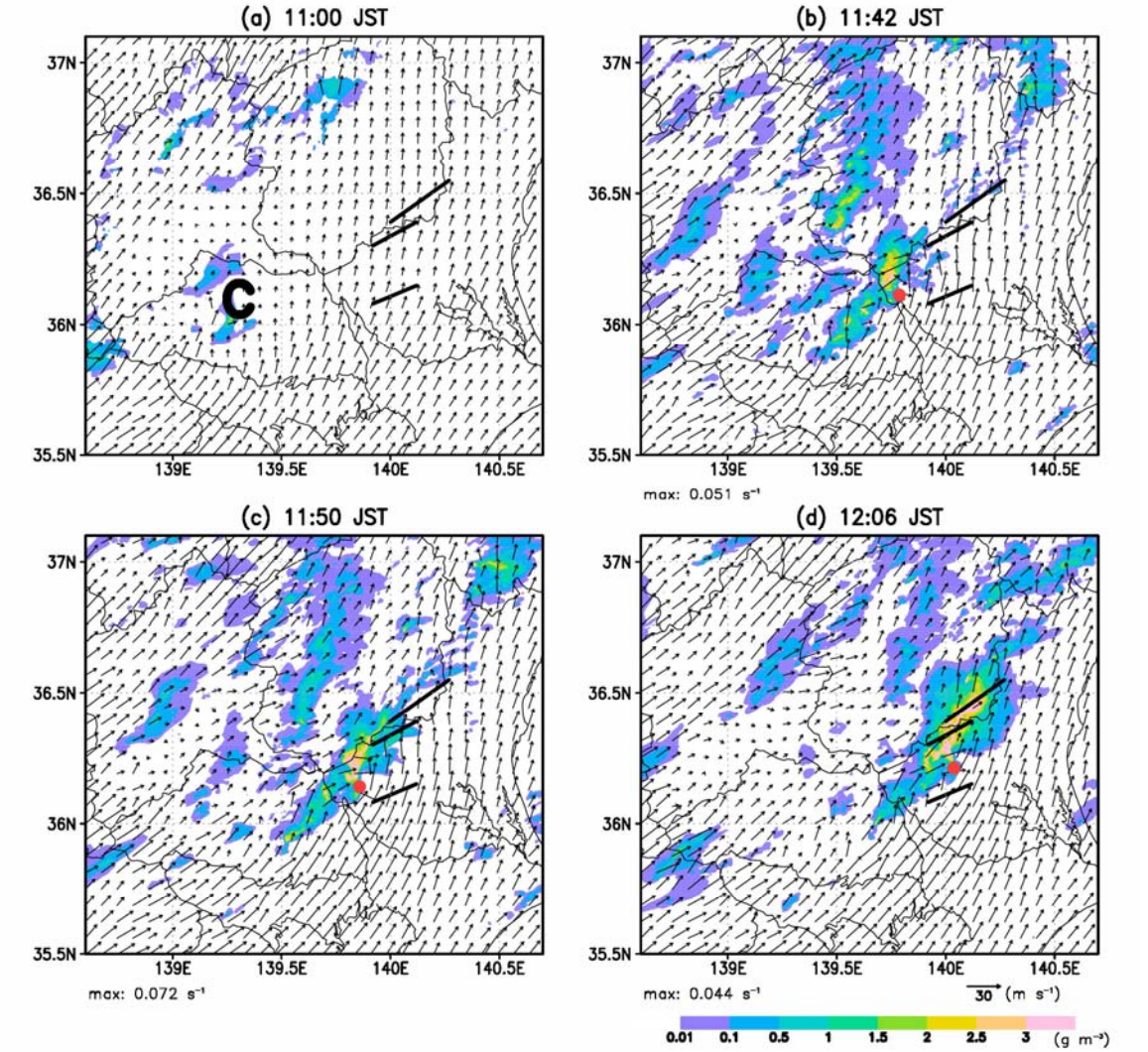

Fig. 3.1. The total of rain, snow, and graupel (color shading, g m^{-3}) and horizontal winds (arrows, m s^{-1}) at 0.8-km height at (a) 1100, (b) 1142, (c) 1150, and (d) 1206 JST in 350m-EXPm (CTL). Red dots denote the location of maximum $\zeta^{(\mathrm{LMC})}$ [value given below (b)–(d)]. Black lines are as in Fig. 2.1. Region C denotes the position of the convective system.

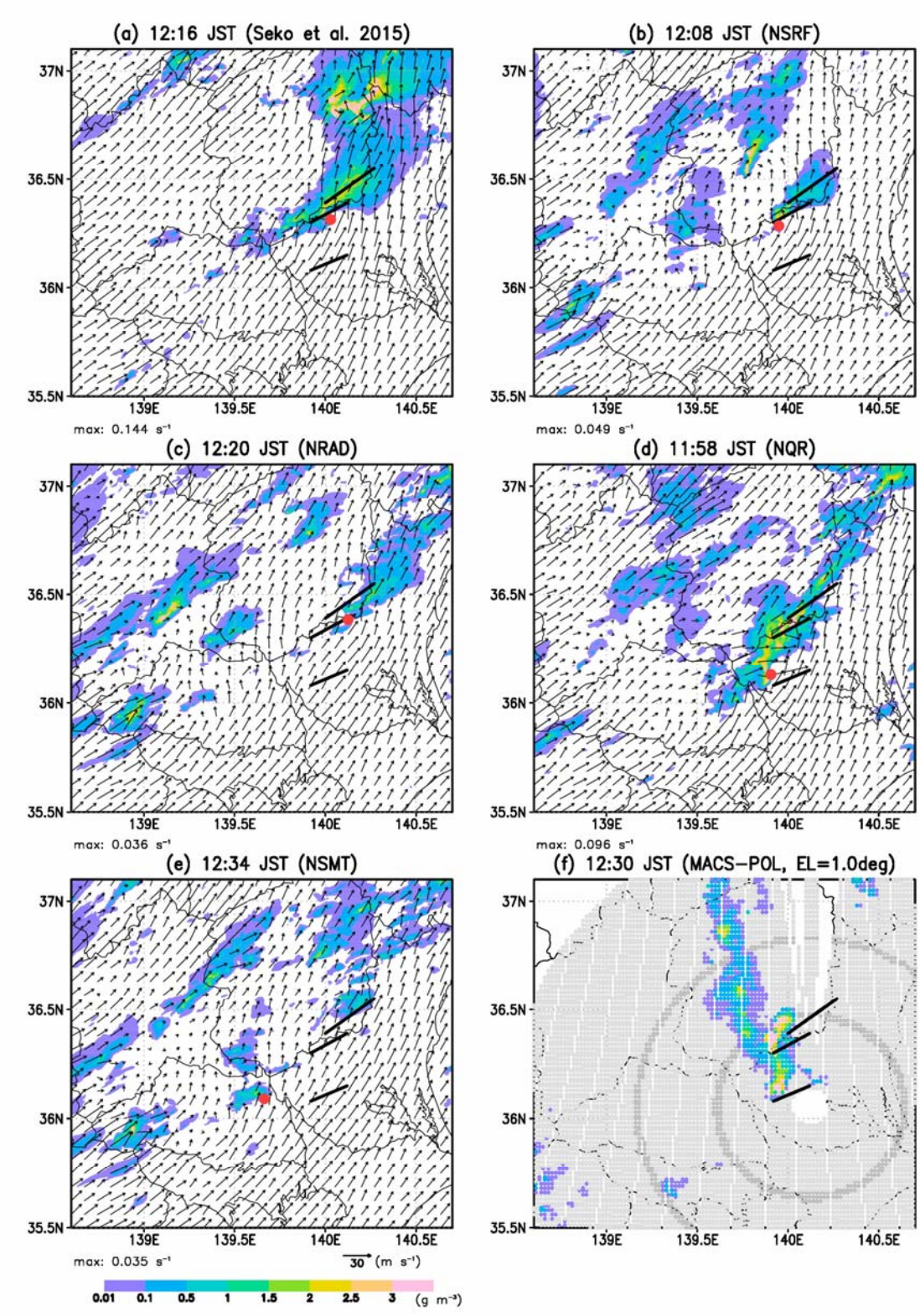

Fig. 3.2. The total of rain, snow, and graupel (color shading, g m^{-3}) and horizontal winds (arrows, m s^{-1}) at 0.8-km height when $\zeta^{(\mathrm{LMC})}$ reached a maximum in (a) the experimental design of Seko et al. (2015), (b) NSRF, (c) NRAD, (d) NQR, and (e) NSMT. (f) Rainwater Q_R (g m^{-3}) estimated from Z and K_{DP} at 1.0° elevation at 1230 JST. In the gray area, 0 g m^{-3} rainwater was estimated. The dark gray shows the heights of 1 km and 2 km.

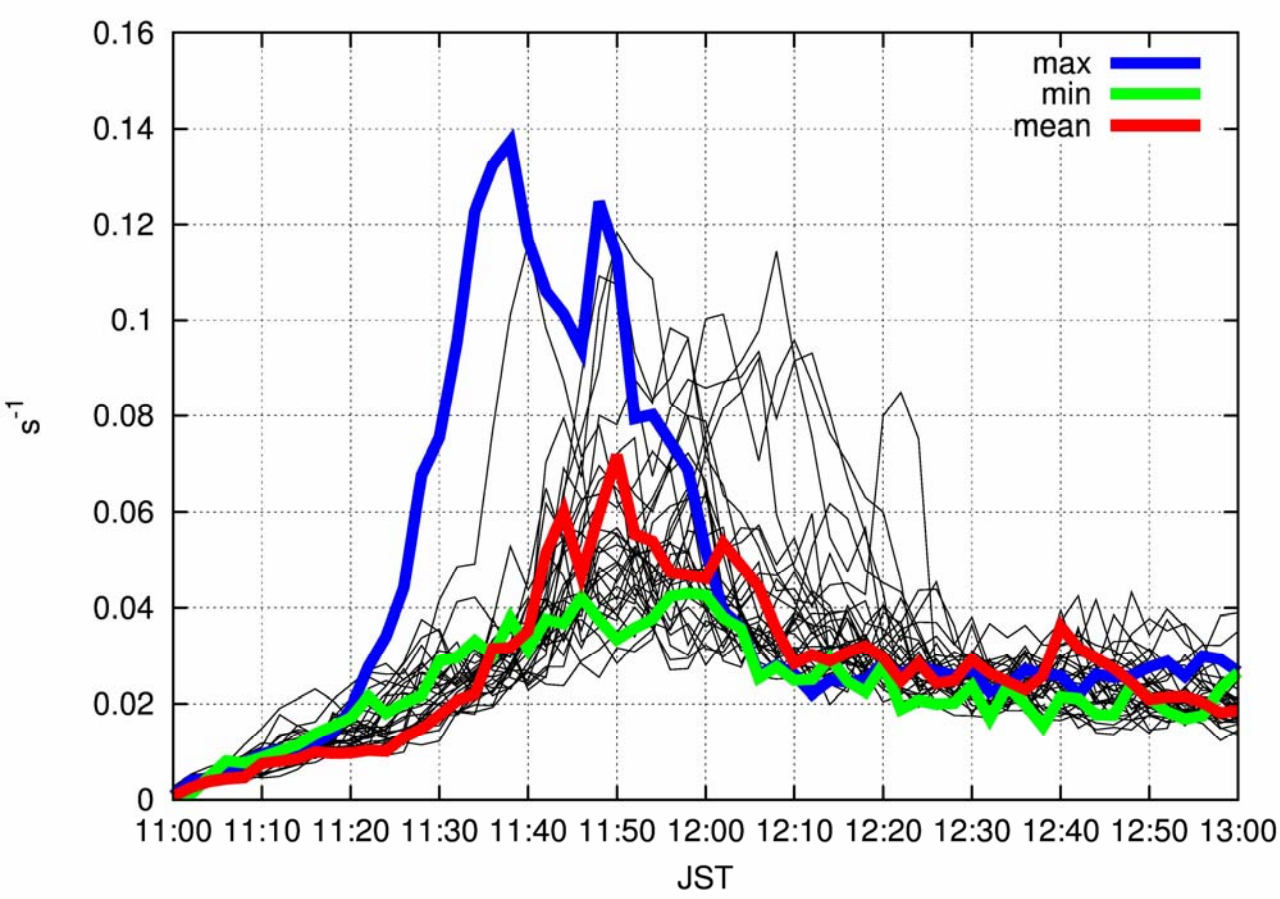

Fig. 3.3. Time series of maximum vertical vorticity (s^{-1}) at 0.8-km height, $\zeta^{(\mathrm{LMC})}$, within the region of 139.4°–140.2°E and 36.0°–36.4°N in 350m-EXPs (CTL) (red line, member with mean initial condition; blue line, member with maximum $\zeta_{\mathrm{MAX}}^{(\mathrm{LMC})}$; green line, member with minimum $\zeta_{\mathrm{MAX}}^{(\mathrm{LMC})}$).

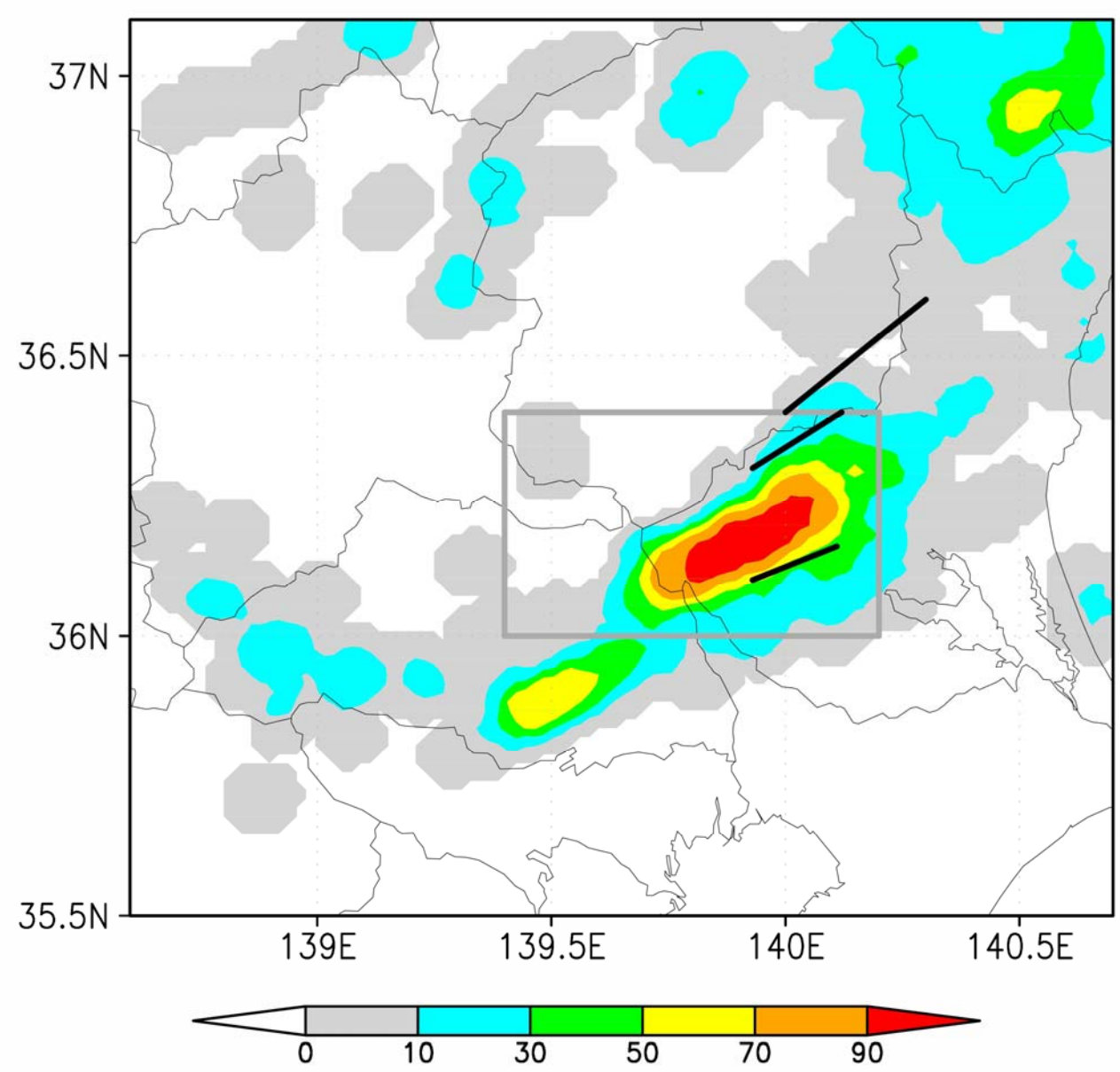

Fig. 3.4. Probability map that high vertical vorticity (exceeding 0.03 s^{-1}) at 0.8-km height appears within 5 km from each point, based on the 33 members of 350m-EXPs (CTL) (%). Black lines denote the paths of Tsukuba, Chikusei, and Moka tornadoes in order from the south. The gray rectangle indicates the region where $\zeta^{(\mathrm{LMC})}$ was calculated (see Fig. 3.3).

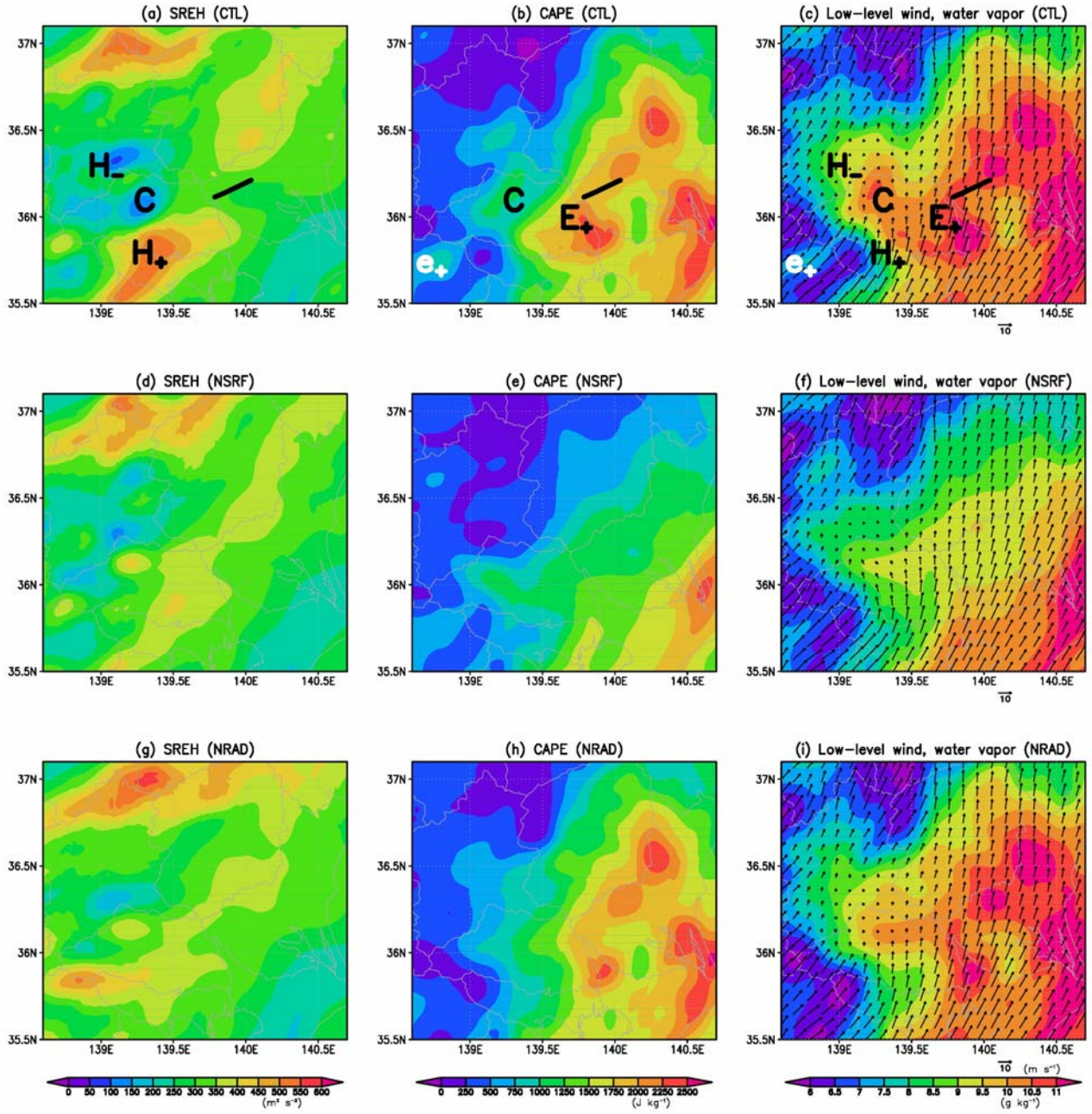

Fig. 3.5. Horizontally smoothed (a),(d),(g),(j),(m) SREH at 0–3-km height (m^2 s^{-2}), (b),(e),(h),(k),(n) MLCAPE (J kg^{-1}), and (c),(f),(i),(l),(o) horizontal winds (arrows, m s^{-1}) and water vapor (color shading, g kg^{-1}) averaged below the height of 1 km at 1100 JST in 350m-EXPm: (a)–(c) CTL; (d)–(f) NSRF; (g)–(i) NRAD; (j)–(l) NQR; (m)–(o) NSMT. Thick black lines in (a)–(c) indicate the path of the predicted LMC. Region C is as in Fig. 3.1. Regions H_+, H_-, and E_+ denote the positions of large SREH, small SREH, and large MLCAPE, respectively. Region e_+ is explained in Fig. 3.6.

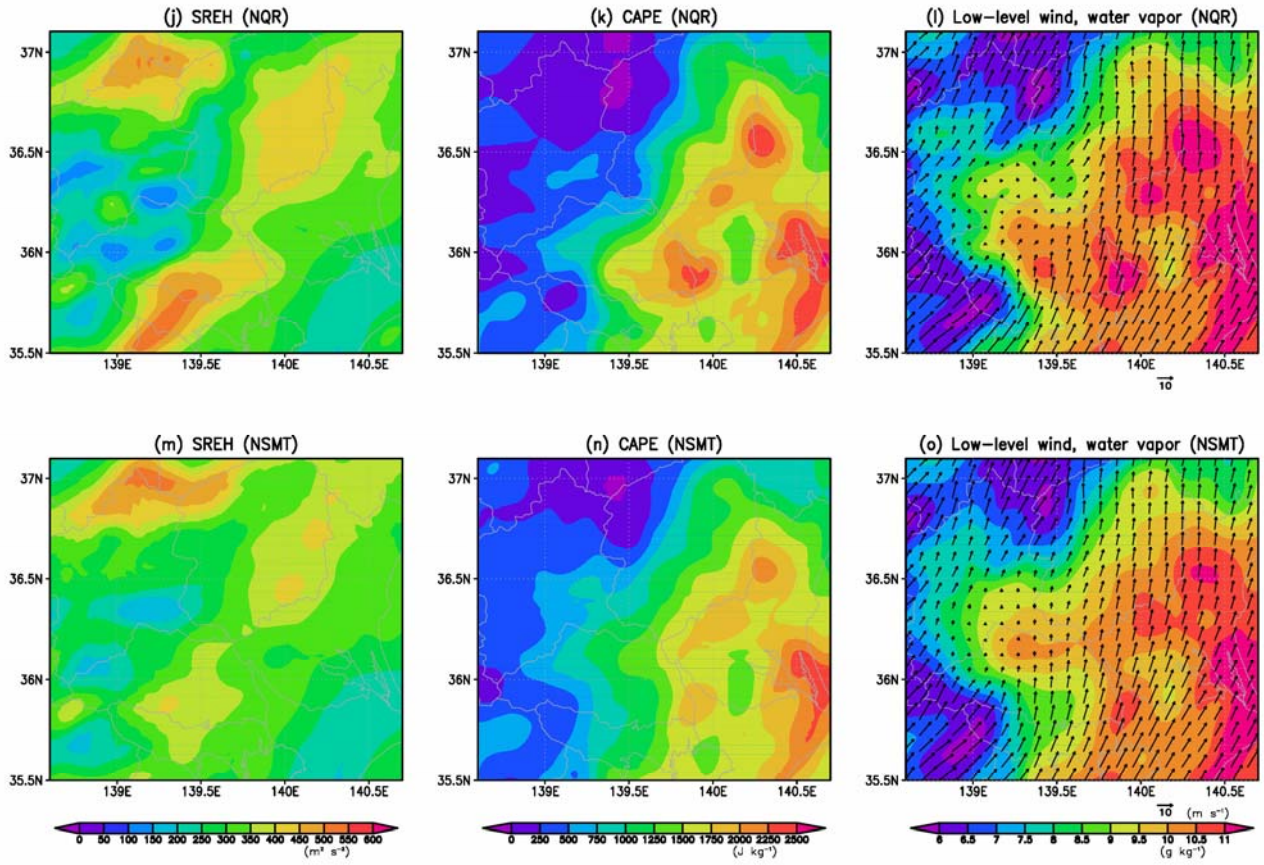

Fig. 3.5. (*Continued*)

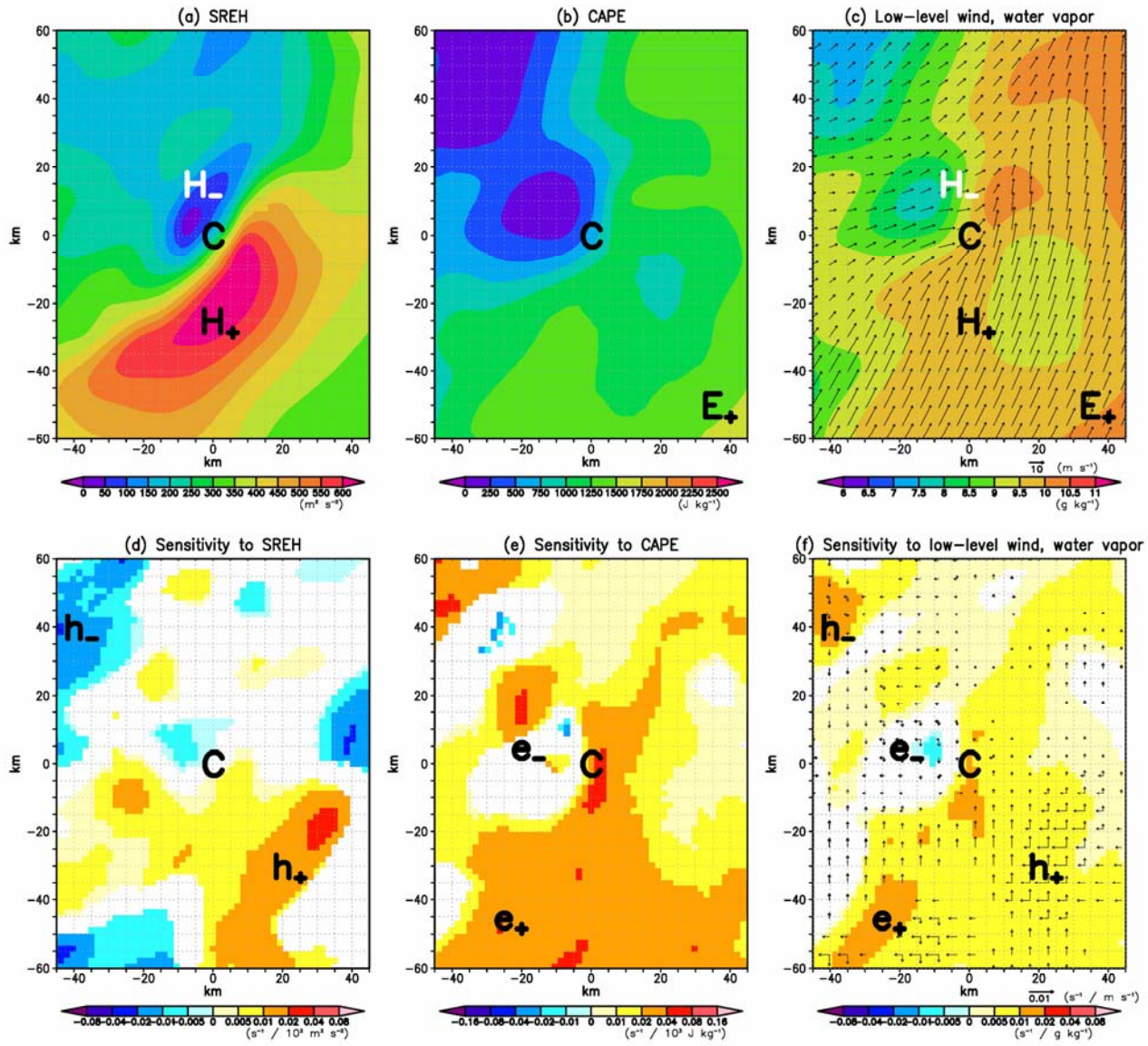

Fig. 3.6. Ensemble mean of horizontally smoothed (a) SREH at 0–3-km height (m^2 s^{-2}), (b) MLCAPE (J kg^{-1}), and (c) horizontal winds (arrows, m s^{-1}) and water vapor (color shading, g kg^{-1}) averaged below a height of 1 km, and sensitivities of $\zeta_{\mathrm{MAX}}^{(\mathrm{LMC})}$ (s^{-1}) to (d) SREH at 0–3-km height [s^{-1} (10^2 m^2 s^{-2})$^{-1}$], (e) MLCAPE [s^{-1} (10^3 J kg^{-1})$^{-1}$], and (f) zonal and meridional winds [arrows, s^{-1} (m s^{-1})$^{-1}$] and water vapor [color shading, s^{-1} (g kg^{-1})$^{-1}$] averaged below a height of 1 km in the composite field to the position of $\zeta^{(\mathrm{LMC})}$ for 350m-EXPs (CTL). Only higher reliability than 50% (absolute value of correlation > 0.122) was shown in (d)–(f), and MLCAPE > 100 J kg^{-1} was shown in (e). Region C denotes the position of $\zeta^{(\mathrm{LMC})}$. Regions $h_{+(-)}$ and $e_{+(-)}$ denote the positions of positive (negative) sensitivities to SREH and MLCAPE, respectively. The other letters are as in Fig. 3.5.

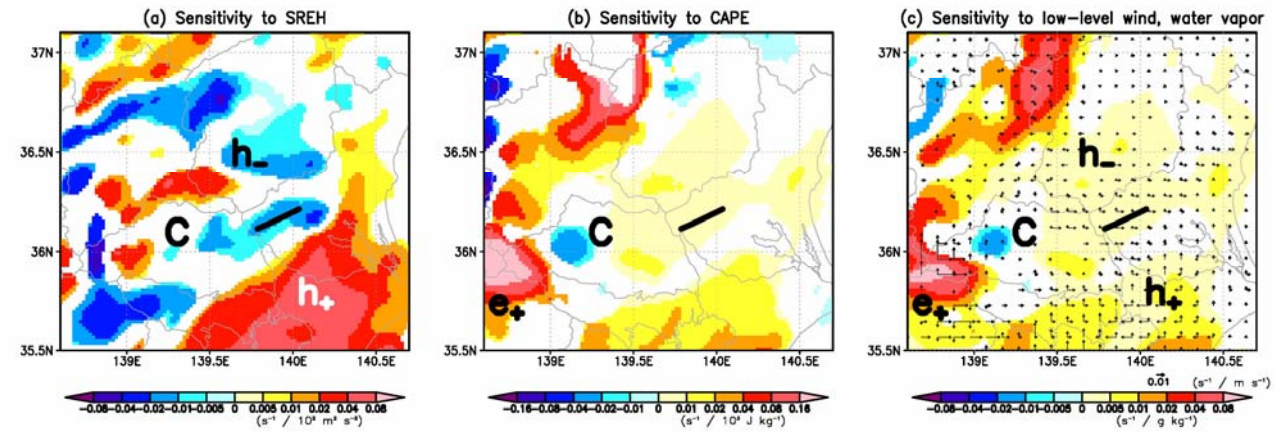

Fig. 3.7. Sensitivities of $\zeta_{\mathrm{MAX}}^{(\mathrm{LMC})}$ (s^{-1}) to (a) SREH at 0–3-km height [s^{-1} (10^2 m^2 s^{-2})$^{-1}$], (b) MLCAPE [s^{-1} (10^3 J kg^{-1})$^{-1}$], and (c) zonal and meridional winds [arrows, s^{-1} (m s^{-1})$^{-1}$] and water vapor [color shading, s^{-1} (g kg^{-1})$^{-1}$] averaged below a height of 1 km in the initial (1100 JST) field in 350m-EXPs (CTL). Only higher reliability than 50% (absolute value of correlation > 0.122) was shown, and MLCAPE > 100 J kg^{-1} was shown in (b). The thick black line denotes the path of the predicted LMC. Letters are as in Figs. 3.5 and 3.6.

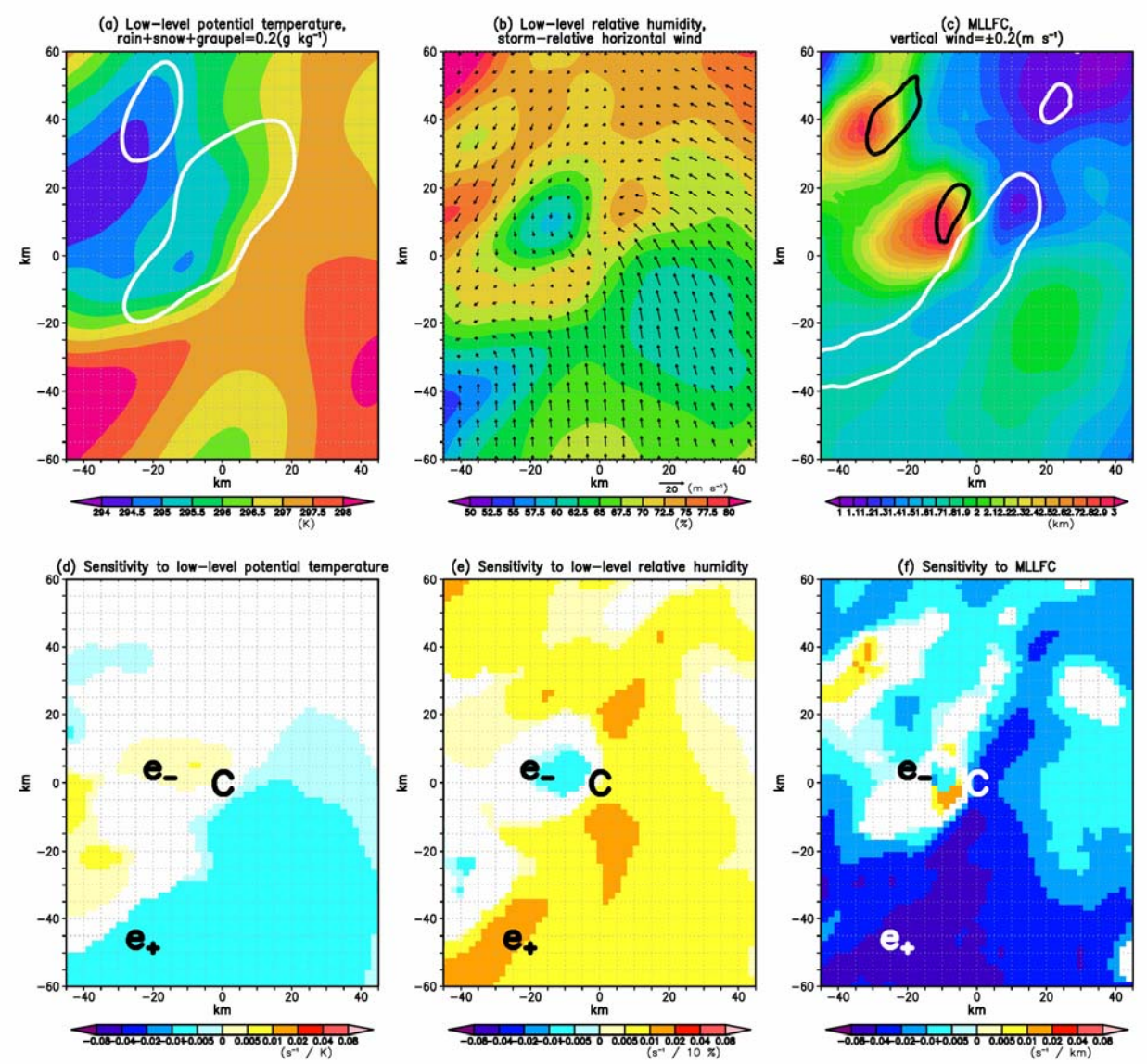

Fig. 3.8. Ensemble mean of horizontally smoothed (a) potential temperature (color shading, K) and the total of rain, snow, and graupel (white contours, 0.2 g kg^{-1}), (b) relative humidity (color shading, %) and horizontal winds relative to that of the center (arrows, m s^{-1}), and (c) MLLFC (color shading, km) and vertical velocity (white and black contours, ±0.2 m s^{-1}) in the composite field to the position of $\zeta^{(\mathrm{LMC})}$ for 350m-EXPs (CTL), and sensitivities of $\zeta^{(\mathrm{LMC})}_{\mathrm{MAX}}$ (s^{-1}) to (d) potential temperature (s^{-1} K^{-1}), (e) relative humidity [s^{-1} (10%)$^{-1}$], and (f) MLLFC (s^{-1} km^{-1}). Variables shown here have been averaged below a height of 1 km. Only higher reliability than 50% (absolute value of correlation > 0.122) were shown in (d)–(f). Letters are as in Fig. 3.6.

5 年以内に雑誌等で公表予定のため、非公開。

Fig. 3.9. Scatter plots of $\zeta_{\mathrm{MAX}}^{(\mathrm{LMC})}$ (s^{-1}) and (a),(b) water vapor (g kg^{-1}), (c),(d) potential temperature (K), and (e),(f) relative humidity (%) averaged below a height of 1 km, and (g),(h) MLLFC (km) at regions (a),(c),(e),(g) e_- and (b),(d),(f),(h) e_+. The numbers written at top left are correlation coefficient.

4. Ensemble forecasts for tornadogenesis

本章については、5 年以内に雑誌等で公表予定のため、非公開。

5. Discussion

本章については、5 年以内に雑誌等で公表予定のため、非公開。

6. Conclusions and remarks

本章については、5 年以内に雑誌等で公表予定のため、非公開。

Acknowledgements

The author thanks Prof. Hiroshi Niino for thoughtful advices about the whole of this study and encouragement to promote this study, Dr. Hiromu Seko for giving the nested 4D-LETKF system and useful advices about data assimilation and mesoscale meteorology, Mr. Masaru Kunii, Dr. Kazumasa Aonashi, Dr. Seiji Origuchi, Dr. Tadashi Tsuyuki, and Dr. Takemasa Miyoshi for important advices about how to study EnKF and associated data assimilation methods, Mr. Hiroshi Yamauchi for giving MACS-POL radar data and important suggestions about radar data, Dr. Wataru Mashiko for important advices about dynamics of tornadoes and how to perform vorticity and circulation analyses, and Prof. Hiroaki Miura, Prof. Masaki Sato, Prof. Yukari Takayabu, and Prof. Akira Oka for thoughtful comments that improved the original manuscript.

The author also thanks Dr. Kosuke Ito and anonymous reviewers of SOLA for thoughtful comments on Yokota et al. (2016a), Prof. Yvette Richardson and anonymous reviewers of Monthly Weather Review for thoughtful comments on Yokota et al. (2016b), and Dr. Kazuo Saito, Dr. Takuya Kawabata, Ms. Michiko Otsuka, Dr. Le Duc, Dr. Tsutao Oizumi, Dr. Tadashi Fujita, Mr. Yasutaka Ikuta, Prof. Keita Iga, Dr. Wataru Yanase, Dr. Junshi Ito, Dr. Eigo Tochimoto, Dr. Shun-ichi Watanabe, Mr. Kenta Sueki, Dr. Ken-ichi Shimose, Dr. Ryohei Kato, Dr. Takumi Honda, Dr. Yoshinori Shoji, Dr. Ahoro Adachi, Mr. Nobuhiro Nagumo, Mr. Eiichi Sato, Mr. Shugo Hayashi, Dr. Teruyuki Kato, Mr. Hiroshige Tsuguchi, and Mr. Kentaro Araki for many important suggestions that improved this study.

This work was supported in part by the research projects “HPCI Strategic Program for Innovative Research (SPIRE) Field 3,” “social and scientific priority issues (Theme 4) to be tackled by using post K computer of the FLAGSHIP2020 Project,” “Tokyo Metropolitan Area Convection Study for Extreme Weather Resilient Cities (TOMACS),” JSPS KAKENHI Grant Numbers JP24244074 and JP16K17804, and the Cooperative Program (No. 131, 2014; No. 136, 2015; No. 138, 2016) of Atmosphere and Ocean Research Institute, The University of Tokyo. Outer and inner LETKFs were conducted using the Fujitsu PRIMEHPC FX10 System (Oakleaf-FX, Oakbridge-FX) at the Information Technology Center, The University of Tokyo, and the 350m-EXPs and 50m-EXPs were conducted using the K computer at the RIKEN Advanced Institute for Computational Science through the HPCI System Research Project (Project ID: hp120282, hp130012, hp140220, hp150214, hp150289, hp160229).

MACS-POL Radar data were from second laboratory, Meteorological Satellite and Observation System Research Department, Meteorological Research Institute. ESN data were from NTT DOCOMO, Inc., which is Japan’s mobile service provider. XRAIN data were from Ministry of Land, Infrastructure, Transport and Tourism (MLIT). Other observations (C-band radar data, AMeDAS data, and so on), mesoscale analysis data, and global forecast data were from JMA. The simplified parameterizations, primitive-equation dynamics (SPEEDY) model, developed by Franco Molteni and Fred Kucharski, and SPEEDY-LETKF, developed by Dr. Takemasa Miyoshi, were used for assimilation experiments in Appendix C. The source code developed by Numerical Prediction Division, JMA was used for minimizing the cost function of the ensemble-based variational method (EnVAR).

Appendices

A. Quality control of ESN data

In the present experiments, surface observation data from AMeDAS and ESN were transformed to data at 20-m height before they were assimilated. AMeDAS instruments are located at about 10-m height, which is high enough for them to be applied in Eq. (2.7) for transformation to 20-m height. However, some ESN instruments are located at a height of just a few meters, which is too low for the data to be transformed to data at 20-m height. In addition, some ESN stations are located in an environment that is not suitable for surface observations. Therefore, we controlled the quality of ESN surface data for reliable assimilation results.

To evaluate the ESN data, surface zonal and meridional winds and temperature of the JMA hourly analysis (Muroi et al. 2008) were first interpolated to the horizontal positions of the ESN instruments. Because the heights of the interpolated winds (u_A and v_A) and temperature (T_A) were 10 m and 1.5 m, respectively, the ESN data ($u_{\mathrm{obs}}, v_{\mathrm{obs}}, T_{\mathrm{obs}}$) were transformed to data at heights of 10 m, 10 m, and 1.5 m for comparison with (u_A, v_A, T_A), respectively. The differences between the transformed ESN data and (u_A, v_A, T_A) are given as

$$\begin{pmatrix}\delta u\\ \delta v\end{pmatrix} = \frac{\ln(10.0/z_0)}{\ln(z_{\mathrm{obs}}/z_0)}\begin{pmatrix}u_{\mathrm{obs}}\\ v_{\mathrm{obs}}\end{pmatrix} - \begin{pmatrix}u_A\\ v_A\end{pmatrix}, \tag{A.1}$$

$$\delta T = T_{\mathrm{obs}} - \Gamma[(z_{\mathrm{m}} + 1.5) - (z_{\mathrm{s}} + z_{\mathrm{obs}})] - T_A\,. \tag{A.2}$$

In this study, u_{20} and v_{20} were not assimilated at points where the bias of δu or δv was more than 2.0 m s^{-1} or the RMS of δu or δv was more than 1.5 m s^{-1}. Similarly, T_{20} was not assimilated at points where the bias or RMS of δT was more than 1.0 K. These thresholds are the same as those used by Nishi et al. (2015). Biases and RMSs were calculated from hourly surface data for 29 April to 13 May 2012 and 26 August to 9 September 2013; both of these periods include the time when tornadoes were generated on the Kanto Plain.

Relative humidity data from ESN were not evaluated in this study because the horizontal interval between JMA meteorological observatories where relative humidity is observed is too coarse (50–100 km) to be used as a reference for the ESN data. In the present study, relative humidity was assimilated only at points where temperature data were used, because ESN hygrometers are located at the same locations as ESN thermometers.

B. Ensemble-based sensitivity analysis of the case in 2 September 2013

本章については、5 年以内に雑誌等で公表予定のため、非公開。

C. Ensemble-based variational data assimilation compared to LETKF

The analytical method in EnKF assumes linearity of the observation operator and Gaussianity of the probability density function (PDF) to explicitly solve the analysis from the first guess. These assumptions in EnKF cause problems in data assimilation with a multi-scale model (Tsuyuki 2014). In particular, analyses of mixing ratios of water vapor, water, and ice are not expected to be accurate with EnKF because their PDFs are not Gaussian. One way to avoid such assumptions in EnKF is to minimize the cost function implicitly with an ensemble-based variational method (EnVAR, Zupanski 2005; Zupanski et al. 2008; Liu et al. 2008, 2009). In this appendix, we show some advantages of 4D-EnVAR compared to 4D-LETKF.

It is not simple to make clean comparisons between EnVAR and EnKF because generic variational data assimilation systems and EnKF systems differ in many respects of solution algorithm, which are optimized for each system to improve efficiency of the calculation, dynamical balance of the analysis, and so on (Buehner et al. 2010). Although Liu et al. (2008) showed that the result of 4D-EnVAR is closer to the true value than that of EnKF, they did not compare 4D-EnVAR to 4D-EnKF, which performs the analysis with observations for any time in the assimilation window. It is not yet known whether 4D-EnVAR is better than 4D-EnKF from the viewpoint of minimizing the cost function either implicitly or explicitly.

One unavoidable problem in developing an ensemble data assimilation system is the sampling error generated by limiting the number of ensemble members. To reduce this error, spatial localization should be used in EnVAR as well as in EnKF. In the previous EnVAR systems (e.g., Buehner 2005; Liu et al. 2009; Aonashi and Eito 2011), spatial localization has been applied to non-diagonal components of the forecast error covariance matrix (model space localization). To make clean comparisons between EnVAR and LETKF, however, we need to apply same localization factor as Eq. (2.6), the practice adopted in LETKF. Hence, we designed a 4D-EnVAR system with observation space localization to demonstrate that the result of 4D-EnVAR was closer to the true value than that of 4D-LETKF.

The formulation of 4D-EnVAR with observation space localization is derived from the cost function $\tilde{J}$ with the localized forecast error covariance matrix (model space localization) defined as

$$\tilde{J} = \frac{1}{2}\left(\overline{\mathbf{x}_0^a} - \overline{\mathbf{x}_0^f}\right)^T \mathbf{B}_0^{-1}\left(\overline{\mathbf{x}_0^a} - \overline{\mathbf{x}_0^f}\right) + \frac{1}{2}\sum_{t=0}^{T}\left[H\left(\overline{\mathbf{x}_t^a}\right) - \mathbf{y}_t\right]^T \mathbf{R}_t^{-1}\left[H\left(\overline{\mathbf{x}_t^a}\right) - \mathbf{y}_t\right], \tag{C.1}$$

where $\overline{\mathbf{x}_t^{a(f)}} = \left(\overline{x_{1j,t}^{a(f)}}, \ldots, \overline{x_{nj,t}^{a(f)}}\right)$, $\mathbf{y}_t = \left(y_{1,t}, \ldots, y_{K,t}\right)$, and $H\left(\overline{\mathbf{x}_t^a}\right) = \left[H_1\left(\overline{\mathbf{x}_t^a}\right), \ldots, H_K\left(\overline{\mathbf{x}_t^a}\right)\right]$. $H_k\left(\overline{\mathbf{x}_t^a}\right)$ is the observation operator to convert the value corresponding to observation $y_{k,t}$ from analysis $\overline{\mathbf{x}_t^a}$. $\mathbf{R}_t$ is $K \times K$ observation error covariance matrix at time slot t, and (k_1, k_2) component of $\mathbf{R}_t$ is

$$\left(\mathbf{R}_t\right)_{k_1 k_2} = \begin{cases} R_{k_1,t} & (k_1 = k_2) \\ 0 & (k_1 \neq k_2) \end{cases}. \tag{C.2}$$

$\mathbf{B}_t$ is $n \times n$ localized forecast error covariance matrix at time slot t, and (i_1, i_2) component of $\mathbf{B}_t$ is

$$(\mathbf{B}_t)_{i_1 i_2} = \frac{\alpha^2 L_{i_1 i_2}}{m-1} \sum_{j=1}^{m} \delta x^f_{i_1 j,t} \delta x^f_{i_2 j,t} \,, \tag{C.3}$$

where $L_{i_1 i_2}$ is the localization factor between points i_1 and i_2.

Using Eqs. (C.2) and (C.3) and variable transformation from $\overline{x^a_{i,t}}$ to $\widetilde{w}_{lj}$ by

$$\overline{x^a_{i,t}} = \overline{x^f_{i,t}} + \sum_{j=1}^{m} \sum_{l=1}^{n} L_{il}^{\frac{1}{2}} \delta x^f_{ij,t} \widetilde{w}_{lj} \,, \tag{C.4}$$

where $L_{i_1 i_2} = \sum_{l=1}^{n} L_{i_1 l}^{1/2} L_{i_2 l}^{1/2}$, Eq. (C.1) is rearranged to

$$\tilde{J} = \frac{1}{2} \left\{ \frac{m-1}{\alpha^2} \sum_{l=1}^{n} \sum_{j=1}^{m} \widetilde{w}_{lj}^2 + \sum_{t=0}^{T} \sum_{k=1}^{K} \frac{1}{R_{k,t}} \left[H_k\left(\overline{\mathbf{x}^a_t}\right) - y_{k,t} \right]^2 \right\}. \tag{C.5}$$

To minimize $\tilde{J}$ in Eq. (C.5) as a function of $\widetilde{w}_{lj}$,

$$\frac{\partial \tilde{J}}{\partial \widetilde{w}_{lj}} = \frac{m-1}{\alpha^2} \widetilde{w}_{lj} + \sum_{t=0}^{T} \sum_{k=1}^{K} \frac{1}{R_{k,t}} \frac{\partial H_k\left(\overline{\mathbf{x}^a_t}\right)}{\partial \widetilde{w}_{lj}} \left[H_k\left(\overline{\mathbf{x}^a_t}\right) - y_{k,t} \right] = 0 \tag{C.6}$$

is required, where

$$\frac{\partial H_k\left(\overline{\mathbf{x}^a_t}\right)}{\partial \widetilde{w}_{lj}} = \sum_{i\prime=1}^{n} \frac{\partial \overline{x^a_{i\prime,t}}}{\partial \widetilde{w}_{lj}} \frac{\partial H_k\left(\overline{\mathbf{x}^a_t}\right)}{\partial \overline{x^a_{i\prime,t}}} = \sum_{i\prime=1}^{n} L_{i\prime l}^{\frac{1}{2}} \delta x^f_{i\prime j,t} \frac{\partial H_k\left(\overline{\mathbf{x}^a_t}\right)}{\partial \overline{x^a_{i\prime,t}}}. \tag{C.7}$$

When $H_k\left(\overline{\mathbf{x}^a_t}\right)$ is linear and calculated only at observation point k, the right hand side of Eq. (C.7) is equal to $L_{kl}^{1/2} \delta H^a_{kj,t}$, where $\delta H^a_{kj,t} = H_k\left(\overline{\mathbf{x}^a_t} + \delta \mathbf{x}^f_{j,t}\right) - H_k\left(\overline{\mathbf{x}^a_t}\right)$. Therefore, from Eqs. (C.6), (C.7), and $L_{ik} = \sum_{l=1}^{n} L_{il}^{1/2} L_{kl}^{1/2}$,

$$\frac{m-1}{\alpha^2} \left(\sum_{l=1}^{n} L_{il}^{\frac{1}{2}} \widetilde{w}_{lj} \right) + \sum_{t=0}^{T} \sum_{k=1}^{K} \frac{L_{ik} \delta H^a_{kj,t}}{R_{k,t}} \left[H_k\left(\overline{\mathbf{x}^a_t}\right) - y_{k,t} \right] \simeq \sum_{l=1}^{n} L_{il}^{1/2} \frac{\partial \tilde{J}}{\partial \widetilde{w}_{lj}} = 0 \tag{C.8}$$

is obtained. When w_{ij} is defined as $w_{ij} = \sum_{l=1}^{n} L_{il}^{1/2} \widetilde{w}_{lj}$, Eq. (C.4) is rearranged to Eq. (2.1) and Eq. (C.8) is to

$$\frac{m-1}{\alpha^2} w_{ij} + \sum_{t=0}^{T} \sum_{k=1}^{K} \frac{L_{ik} \delta H^a_{kj,t}}{R_{k,t}} \left[H_k\left(\overline{\mathbf{x}^a_t}\right) - y_{k,t} \right] = 0 \,, \tag{C.9}$$

where the left hand side of Eq. (C.9) is defined as $\partial J / \partial w_{ij}$. Eq. (C.6) is approximately equal to Eq. (C.9); in other words, the cost function $\tilde{J}$ is minimized by solving Eq. (C.9). Because $\overline{x^a_{i,t}}$ can be calculated independently for each analysis point through Eq. (2.1), solving w_{ij} in Eq. (C.9) is easier than solving $\widetilde{w}_{lj}$ in Eq. (C.6) with parallel computing. For that reason, Eq. (C.9) was used in this system instead of Eq. (C.6).

The analysis ensemble perturbation in this 4D-EnVAR system is calculated independently for each analysis point with Eqs. (2.2) and (2.4), where λ_{ij_2} and $\left(U_{i1j_2}, \ldots, U_{imj_2}\right)$ in Eq. (2.4) are the j_2th eigenvalue and eigenvector of the Hessian $\nabla_i^2 J$. $\nabla_i^2 J$ is an $m \times m$ matrix and its (j_1, j) component, derived from the left hand side of Eq. (C.9), is shown as

$$(\nabla_i^2 J)_{j_1 j} := \frac{\partial^2 J}{\partial w_{ij_1} \partial w_{ij}} = \frac{m-1}{\alpha^2} \delta_{j_1 j} + \sum_{k=1}^{K} \frac{L_{ik}}{R_{k,t}} \delta H^a_{kj_1,t} \delta H^a_{kj,t} \,. \tag{C.10}$$

To summarize the above formulation, Eqs. (C.9) and (C.10) are used in 4D-EnVAR to calculate $\overline{x^a_{i,t}}$ and $\delta x^a_{ij,t}$ instead of Eqs. (2.3) and (2.5) used in 4D-LETKF. If the observation operator H_k is a linear function, then Eq. (C.10) is equivalent to Eq. (2.5) because $\delta H^a_{kj,t} = \delta H^f_{kj,t}$. Moreover, if H_k in Eq. (C.9) is linear and can be calculated from $\overline{x^a_{i,t}}$

alone, then $\partial J/\partial w_{ij}$ in Eq. (C.9) is a linear function of w_{ij} because $H_k(\overline{\mathbf{x}_t^a}) = \overline{H_{k,t}^f} + \sum_{j=1}^m \delta H_{kj,t}^f w_{ij}$. Linear $\partial J/\partial w_{ij}$ means that $\exp(-J)$, which is assumed to be the PDF in the variational method, is Gaussian. In this case, the equations to solve w_{ij} and T_{ij_1j} are identical to the equations of 4D-LETKF (Hunt et al. 2004, 2007; Miyoshi et al. 2007). Therefore, the analysis and its perturbation of 4D-EnVAR are the same as those of 4D-LETKF when $H_k(\boldsymbol{x})$ is linear and analysis point i is located at observation point k. In other words, the analysis and its perturbation of LETKF are obtained with Eqs. (C.9) and (C.10) if $H_k(\boldsymbol{x})$ is linear and J is locally defined.

We confirmed above conformity between EnVAR and LETKF using single-observation assimilation experiments, in which 20-member ensemble forecasts with the "simplified parameterizations, primitive-equation dynamics" (SPEEDY) model (Molteni 2003) were used for the first guess. The SPEEDY model is an AGCM with a T30L7 resolution (represented by 96 × 48 × 7 grid points), and the model variables are zonal and meridional winds (u, v), temperature T, specific humidity q, and surface pressure p_s. Here, these variables are also used as control variables in assimilation with LETKF and EnVAR. If the observation operator is the identity transformation (linear), the EnVAR and LETKF analyses are identical at the observation point (Fig. C.1a and C.1b). However, except for the zonal wind at the observation point, the analysis increment in EnVAR (Fig. C.1b) was smaller than that in LETKF (Fig. C.1a). This increment was smaller because the observation space localization in EnVAR, which was shown to be almost the same as model space localization, was stronger (i.e., it ignored observation information more quickly with distance) than the localization in LETKF (Greybush et al. 2011). If the observation operator was the non-linear, even at the observation point, the EnVAR analysis (Fig. C.1d) is different from the LETKF analysis (Fig. C.1c).

In the weak non-Gaussian PDF, then $\exp(-J)$ is a good approximation of the PDF (Tsuyuki 2014). Therefore, the result from EnVAR, which minimizes globally defined J without assuming linearity of H_k, should be closer to the true value than that of LETKF when $H_k(\boldsymbol{x})$ is non-linear or when observations globally affect physically distant analysis points. To show this advantage of EnVAR, we also performed OSSEs with the SPEEDY model that compared 20-member ensemble forecasts from 4D-LETKF and 4D-EnVAR. In the OSSEs, the true value was defined as the forecast with the SPEEDY model. We used 20 forecasts from the initial true value, in which forecast times ranged from 744 to 972 hours at 12-hour intervals, for the initial values of the 20-member ensemble forecasts. A 6-hour assimilation window was used, extending 3 hours before and after the analysis time. Assimilated observations were created by adding random errors to the true values at 2-hour intervals at the points shown in Fig. C.2, which were u, v, T, p_s, and the relative humidity as calculated from T, q, and p_s. The amplitudes of these random errors were 1 m s^{-1} for u and v, 1 K for T, 100 hPa for p_s, and 10% for relative humidity. The horizontal and vertical localization lengths were same as in the single-observation assimilation experiments (1000 km and 0.1σ, respectively). The multiplicative inflation parameter α (Anderson and Anderson 1999) was 1.1. The analysis-forecast cycle was repeated 160 times (40 days).

Histograms of differences of observations assimilated in EnVAR from ensemble means of their forecasts $(O - F)$ at all analysis times were close to Gaussian (Figs. C.3a–e). However, the histogram for specific humidity (which was not assimilated directly) was far from Gaussian (Fig. C.3f), which is consistent with the result of ensemble experiments with 10,240 members (Miyoshi et al. 2014). Differences from true values of the ensemble means of every-6-hour ensemble

forecasts from the LETKF and EnVAR analyses are shown in Fig. C.4. The root mean square errors (RMSEs) from EnVAR were generally smaller than those from LETKF (Figs. C.4b and C.4d). The biases of variables in EnVAR and LETKF were almost the same (e.g., Fig. C.4a) except that the bias of specific humidity was smaller from EnVAR than from LETKF (Fig. C.4c).

Locally calculating the observation operator is a major reasons why the LETKF analysis in this OSSE was worse than the EnVAR analysis. In fact, even when all observation operators were linear (including direct assimilation of specific humidity rather than relative humidity), the RMSEs and the bias of specific humidity from EnVAR were smaller than those from LETKF (not shown). Moreover, when only non-linear H_k was treated like EnVAR but analyses were solved independently for every analysis point i as in LETKF, RMSEs and biases almost equaled those from LETKF (blue lines in Fig. C.4). These results show that the effect of non-linearity of the observation operator is relatively small and the improvement resulting from globally calculating the observation operator is particularly important for accurate analyses in EnVAR.

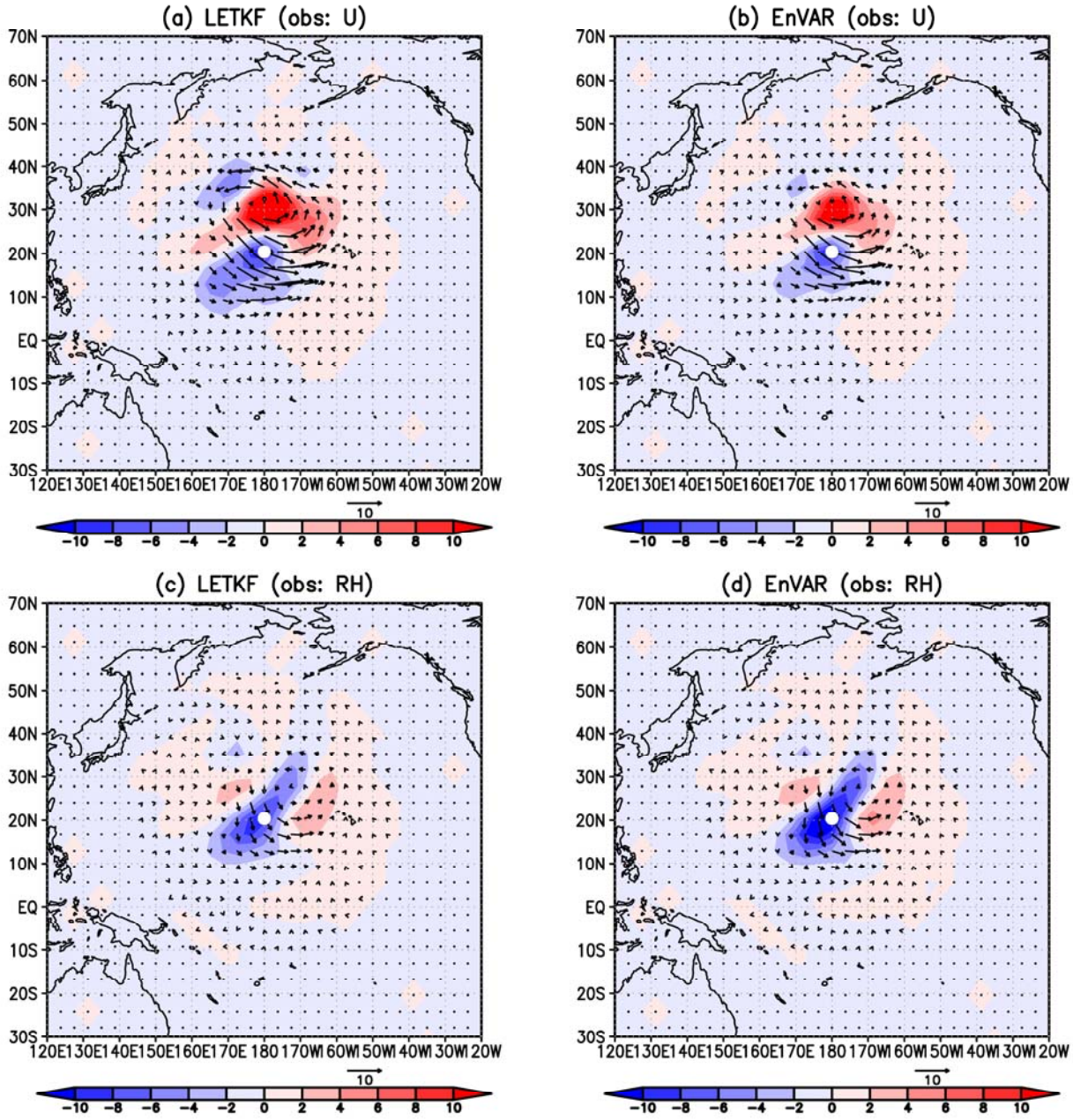

Fig. C.1. Analysis increments of zonal wind (arrows; m s^{-1}) and relative humidity (color shading; %) after assimilation of a single observation at 180°E, 20°N, and 0.835σ (sigma coordinate): zonal wind of 5.0 m s^{-1} with (a) LETKF and (b) EnVAR and relative humidity of 30.0% with (c) LETKF and (d) EnVAR. The horizontal and vertical localization lengths are 1000 km and 0.1σ, respectively. First guesses of a zonal wind and relative humidity at the observation point are –9.8 m s^{-1} and 53.2%, respectively. In the case assimilating zonal wind, the observation operator is the identity transformation (linear), and the LETKF and EnVAR analyses of zonal wind at the observation point are identical (–0.9 m s^{-1}). In the case assimilating relative humidity, the observation operator is the non-linear function of T, q, and p_s, and the LETKF and EnVAR analyses of relative humidity at the observation point are 44.2% and 39.6%, respectively.

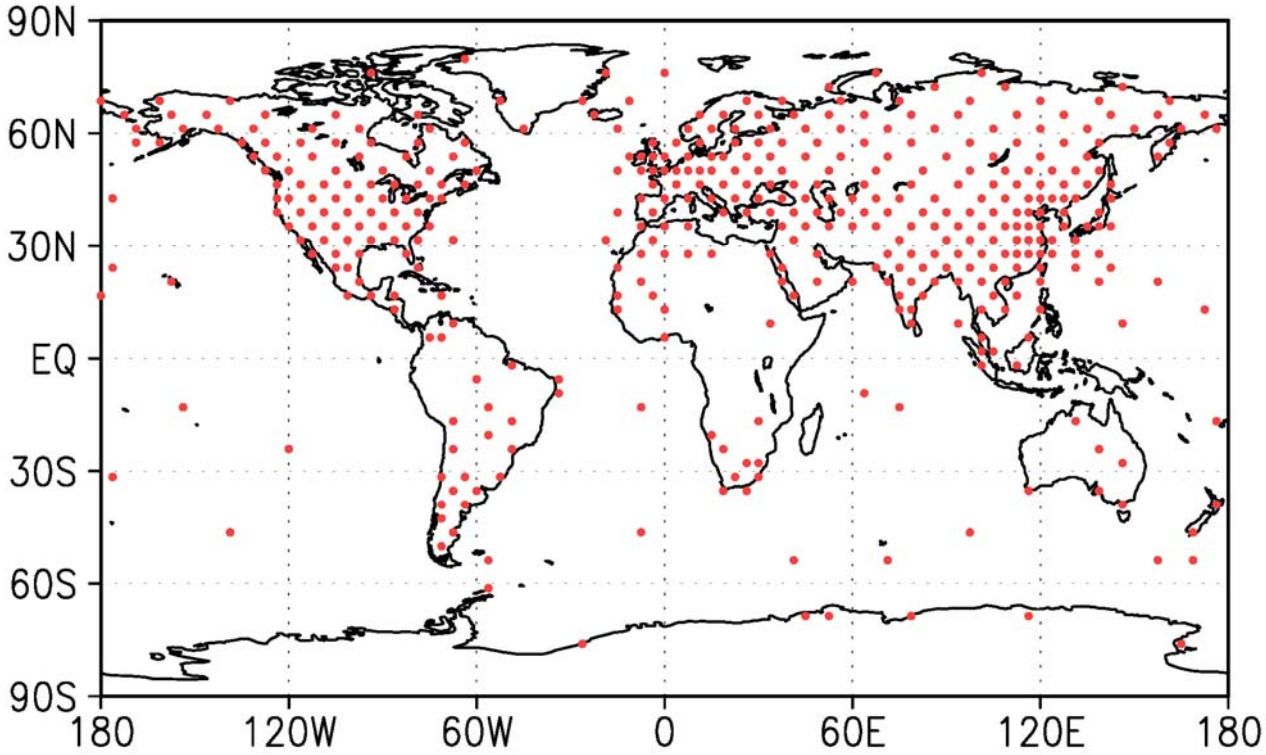

Fig. C.2. Distribution of observations assimilated in OSSEs.

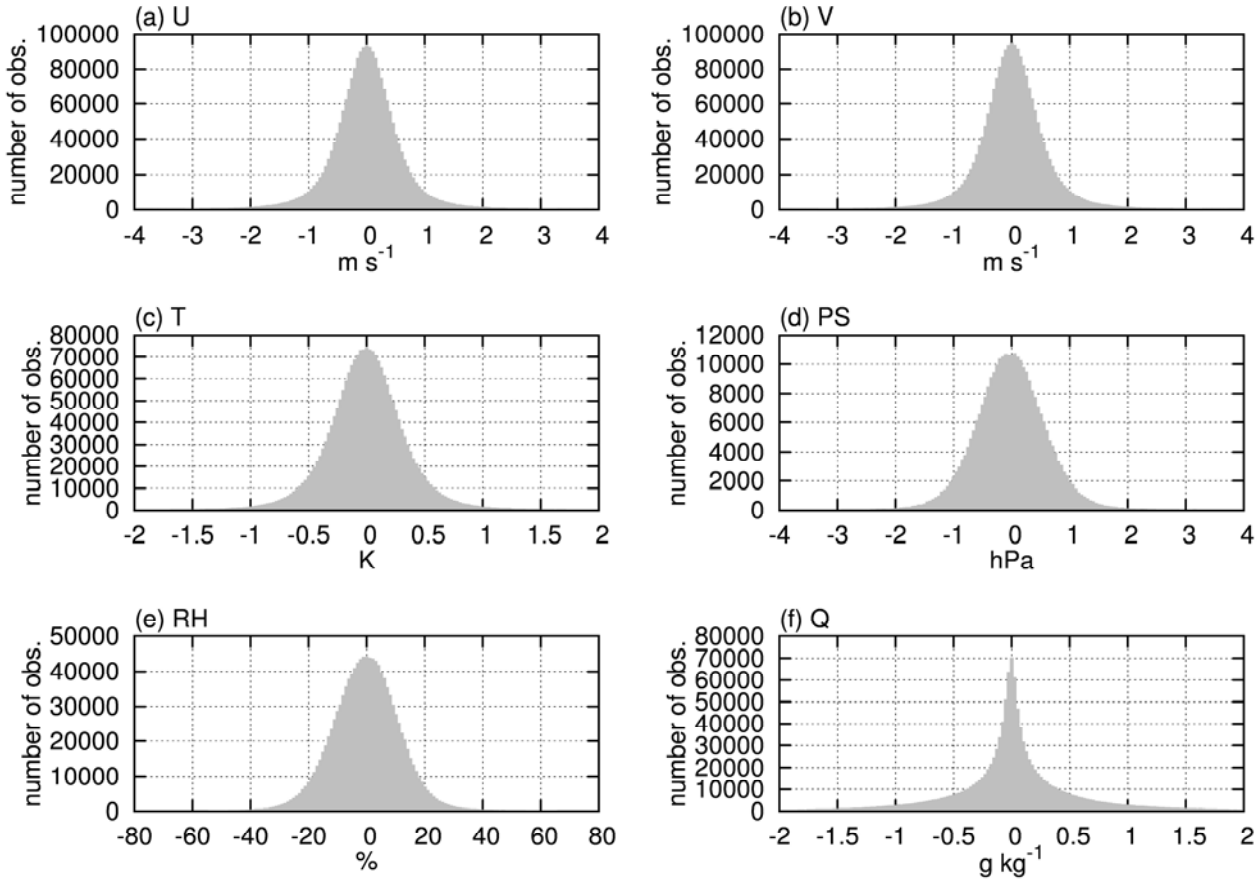

Fig. C.3. Histograms of $(O - F)$ (observation minus forecast) for all analysis times in 4D-EnVAR: (a) zonal winds (m s^{-1}), (b) meridional winds (m s^{-1}), (c) temperature (K), (d) surface pressure (hPa), (e) relative humidity (%), and (f) specific humidity (g kg^{-1}). Note that specific humidity was not assimilated in the experiments shown in Fig. C.4.

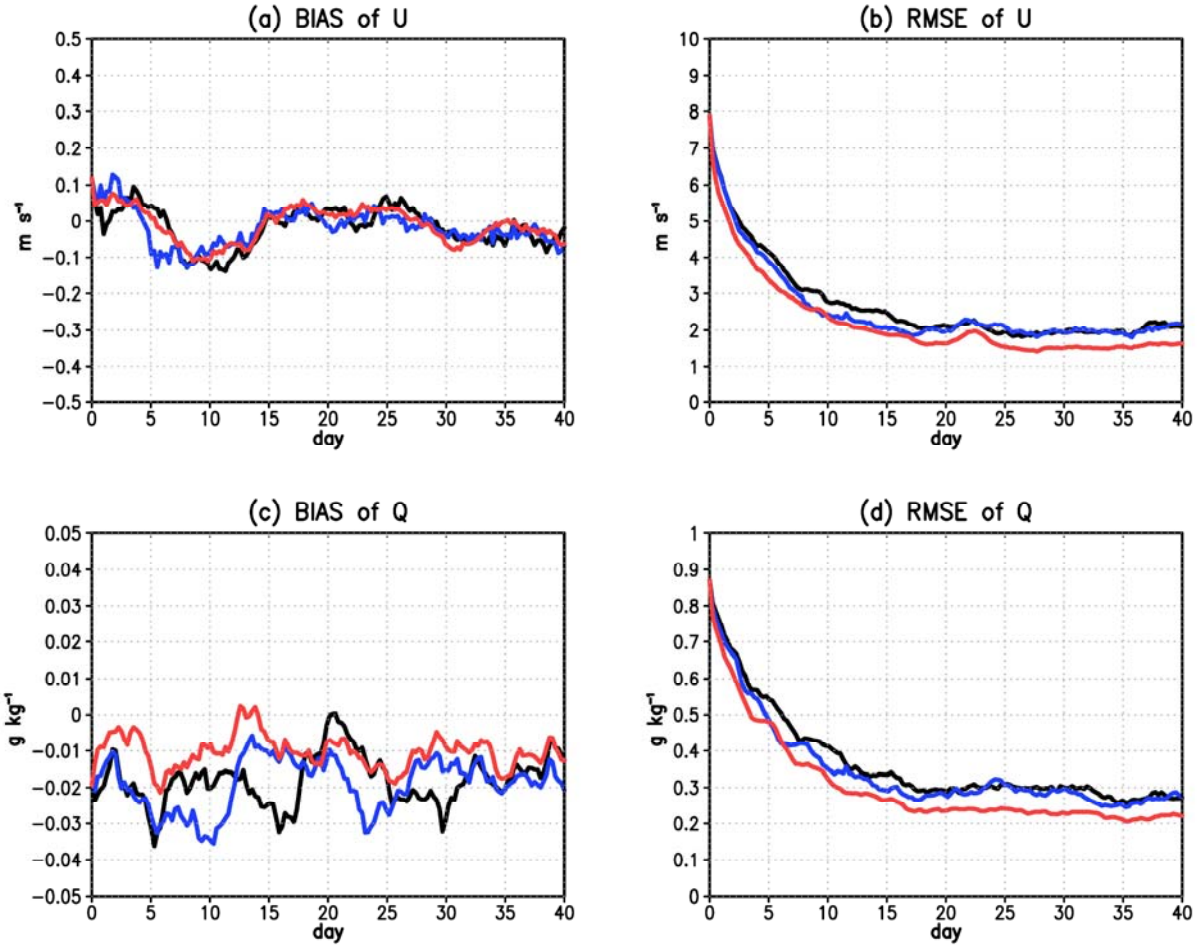

Fig. C.4. (a) Bias and (b) RMSE of ensemble means of zonal wind (m s^{-1}) and (c) bias and (d) RMSE of those of specific humidity (g kg^{-1}) that were predicted for 6 hours from 4D-LETKF analyses (black lines), 4D-EnVAR analyses (red lines), and 4D-EnVAR analyses solved independently for every analysis point (blue lines).

References

Adachi, A., T. Kobayashi, H. Yamauchi, and S. Onogi, 2013: Detection of potentially hazardous convective clouds with a dual-polarized C-band radar. *Atmos. Meas. Tech.*, **6**, 2741–2760.

Adlerman, E. J., K. K. Droegemeier, and R. Davies-Jones, 1999: A numerical simulation of cyclic mesocyclogenesis. *J. Atmos. Sci.*, **56**, 2045–2069.

Ancell, B. C., and G. J. Hakim, 2007: Comparing adjoint- and ensemble-sensitivity analysis with applications to observation targeting. *Mon. Wea. Rev.*, **135**, 4117–4134.

——, C. F. Mass, and G. J. Hakim, 2011: Evaluation of surface analyses and forecasts with a multiscale ensemble Kalman filter in regions of complex terrain. *Mon. Wea. Rev.*, **139**, 2008–2024.

Anderson, J. L., 2001: An ensemble adjustment Kalman filter for data assimilation. *Mon. Wea. Rev.*, **129**, 2884–2903.

——, and S. L. Anderson, 1999: A Monte Carlo implementation of the nonlinear filtering problem to produce ensemble assimilations and forecasts. *Mon. Wea. Rev.*, **127**, 2741–2758.

Aonashi, K., and H. Eito, 2011: Displaced ensemble variational assimilation method to incorporate microwave imager brightness temperatures into a cloud-resolving model. *J. Meteor. Soc. Japan*, **89**, 175–194.

Beljaars, A. C. M., and A. A. M. Holtslag, 1991: Flux parameterization over land surfaces for atmospheric models. *J. Appl. Meteor.*, **30**, 327–341.

Borowska, L., A. Ryzhkov, D. Zrnic, C. Simmer, and R. Palmer, 2011: Attenuation and differential attenuation of 5-cm-wavelength radiation in melting hail. *J. Appl. Meteor. Climatol.*, **50**, 59–76.

Bringi, V. N., and V. Chandrasekar, 2001: *Polarimetric Doppler weather radar: principles and applications*. Cambridge University Press, 636 pp.

Browning, K. A., 1964: Airflow and precipitation trajectories within severe local storms which travel to the right of the winds. *J. Atmos. Sci.*, **21**, 634–639.

Buehner, M., 2005: Ensemble-derived stationary and flow-dependent background-error covariances: Evaluation in a quasi-operational NWP setting. *Quart. J. Roy. Meteor. Soc.*, **131**, 1013–1043.

——, P. L. Houtekamer, C. Charette, H. L. Mitchell, and B. He, 2010: Intercomparison of variational data assimilation and the ensemble Kalman filter for global deterministic NWP. Part I: Description and single-observation experiments. *Mon. Wea. Rev.*, **138**, 1550–1566.

Burgers, G., P. J. van Leeuwen, and G. Evensen, 1998: Analysis scheme in the ensemble Kalman filter. *Mon. Wea. Rev.*, **126**, 1719–1724.

Carey, L. D., S. A. Rutledge, D. A. Ahijevych, and T. D. Keenan, 2000: Correcting propagation effects in C-band polarimetric radar observations of tropical convection using differential propagation phase. *J. Appl. Meteor.*, **39**, 1405–1433.

Caya, A., J. Sun, and C. Snyder, 2005: A comparison between the 4DVAR and the ensemble Kalman filter techniques for

radar data assimilation. *Mon. Wea. Rev.*, **133**, 3081–3094.

Chandrasekar, V., V. N. Bringi, N. Balakrishnan, and D. S. Zrnic, 1990: Error structure of multiparameter radar and surface measurements of rainfall. Part III: Specific differential phase. *J. Atmos. Oceanic Technol.*, **7**, 621–629.

Cintineo, R. M., and D. J. Stensrud, 2013: On the predictability of supercell thunderstorm evolution. *J. Atmos. Sci.*, **70**, 1993–2011.

Craven, J. P., and H. E. Brooks, 2004: Baseline climatology of sounding derived parameters associated with deep, moist convection. *Nat. Wea. Digest*, **28**, 13–24.

Cressman, G. P., 1959: An operational objective analysis system. *Mon. Wea. Rev.*, **87**, 367–374.

Dahl, J. M. L., M. D. Parker, and L. J. Wicker, 2012: Uncertainties in trajectory calculations within near-surface mesocyclones of simulated supercells. *Mon. Wea. Rev.*, **140**, 2959–2966.

Davies-Jones, R. P., 1982: Observational and theoretical aspects of tornadogenesis. *Intense Atmospheric Vortices*, L. Bengtsson and J. Lighthill, Eds. Springer-Verlag, 175–189.

——, D. W. Burgess, and M. P. Foster, 1990: Test of helicity as a tornado forecast parameter. Preprints, *16th Conf. on Severe Local Storms*, Kananaskis, AB, Canada, Amer. Meteor. Soc., 588–592.

Dawson, D. T., M. Xue, J. A. Milbrandt, and M. K. Yau, 2010: Comparison of evaporation and cold pool development between single-moment and multimoment bulk microphysics schemes in idealized simulations of tornadic thunderstorms. *Mon. Wea. Rev.*, **138**, 1152–1171.

——, L. J. Wicker, E. R. Mansell, and R. L. Tanamachi, 2012: Impact of the environmental low-level wind profile on ensemble forecasts of the 4 May 2007 Greensburg, Kansas, tornadic storm and associated mesocyclones. *Mon. Wea. Rev.*, **140**, 696–716.

——, M. Xue, J. A. Milbrandt, and A. Shapiro, 2015: Sensitivity of real-data simulations of the 3 May 1999 Oklahoma city tornadic supercell and associated tornadoes to multimoment microphysics. Part I: Storm- and tornado-scale numerical forecasts. *Mon. Wea. Rev.*, **143**, 2241–2265.

——, ——, A. Shapiro, J. A. Milbrandt, and A. D. Schenkman, 2016: Sensitivity of real-data simulations of the 3 May 1999 Oklahoma city tornadic supercell and associated tornadoes to multimoment microphysics. Part II: Analysis of buoyancy and dynamic pressure forces in simulated tornado-like vortices. *J. Atmos. Sci.*, **73**, 1039–1061.

Dazhang, T., S. G. Geotis, R. E. Passarelli Jr., A. L. Hansen, and C. L. Frush, 1984: Evaluation of an alternating-PRF method for extending the range of unambiguous Doppler velocity. Preprints, *22nd Conf. on Radar Meteorology*, Zurich, Switzerland, Amer. Meteor. Soc., 523–527.

Deardorff, J. W., 1980: Stratocumulus-capped mixed layers derived from a three-dimensional Model. *Bound.-Layer Meteor.*, **18**, 495–527.

Dowell, D. C., F. Zhang, L. J. Wicker, C. Snyder, and N. A. Crook, 2004: Wind and temperature retrievals in the 17 May 1981 Arcadia, Oklahoma, supercell: ensemble Kalman filter experiments. *Mon. Wea. Rev.*, **132**, 1982–2005.

——, L. J. Wicker, and C. Snyder, 2011: Ensemble Kalman filter assimilation of radar observations of the 8 May 2003 Oklahoma city supercell: influences of reflectivity observations on storm-scale analyses. *Mon. Wea. Rev.*, **139**, 272–

294.

Evensen, G., 1994: Sequential data assimilation with a nonlinear quasi-geostrophic model using Monte Carlo methods to forecast error statistics. *J. Geophys. Res.*, **99**, 10 143–10 162.

Fujita, T., D. J. Stensrud, and D. C. Dowell, 2007: Surface data assimilation using an ensemble Kalman filter approach with initial condition and model physics uncertainties. *Mon. Wea. Rev.*, **135**, 1846–1868.

Fujita, T. T., 1971: Proposed characterization of tornadoes and hurricanes by area and intensity. *SMRP Res. Pap. No. 91, Univ. Chicago*, 42 pp.

Greybush, S. J., E. Kalnay, T. Miyoshi, K. Ide, and B. R. Hunt, 2011: Balance and ensemble Kalman filter localization techniques. *Mon. Wea. Rev.*, **139**, 511–522.

Ha, S.-Y., and C. Snyder, 2014: Influence of surface observations in mesoscale data assimilation using an ensemble Kalman filter. *Mon. Wea. Rev.*, **142**, 1489–1508.

Hacker, J. P., and C. Snyder, 2005: Ensemble Kalman filter assimilation of fixed screen-height observations in a parameterized PBL. *Mon. Wea. Rev.*, **133**, 3260–3275.

Honda, Y., 2010: Observation operator. *Append. to Prog. Rep. Numer. Weather Predict.*, **56**, 19–20. (in Japanese).

——, M. Nishijima, K. Koizumi, Y. Ohta, K. Tamiya, T. Kawabata, and T. Tsuyuki, 2005: A Pre-operational variational data assimilation system for a non-hydrostatic model at the Japan Meteorological Agency: formulation and preliminary results. *Quart. J. Roy. Meteor. Soc.*, **131**, 3465–3475.

Hu, M., and M. Xue, 2007: Impact of configurations of rapid intermittent assimilation of WSR-88D radar data for the 8 May 2003 Oklahoma city tornadic thunderstorm case. *Mon. Wea. Rev.*, **135**, 507–525.

——, ——, and K. Brewster, 2006a: 3DVAR and cloud analysis with WSR-88D level-II data for the prediction of the Fort Worth, Texas, tornadic thunderstorms. Part I: Cloud analysis and its impact. *Mon. Wea. Rev.*, **134**, 675–698.

——, ——, J. Gao, and K. Brewster, 2006b: 3DVAR and cloud analysis with WSR-88D level-II data for the prediction of the Fort Worth, Texas, tornadic thunderstorms. Part II: Impact of radial velocity analysis via 3DVAR. *Mon. Wea. Rev.*, **134**, 699–721.

Hubbert, J., and V. N. Bringi, 1995: An iterative filtering technique for the analysis of copolar differential phase and dual-frequency radar measurements. *J. Atmos. Oceanic Technol.*, **12**, 643–648.

Hunt, B. R., and Coauthors, 2004: Four-dimensional ensemble Kalman filtering. *Tellus*, **56A**, 273−277.

——, E. J. Kostelich, and I. Szunyogh, 2007: Efficient data assimilation for spatiotemporal chaos: A local ensemble transform Kalman filter. *Phys. D*, **230**, 112–126.

Ikuta, Y., 2012: Radar reflectivity assimilation in JMA's operational meso-analysis system. *CAS/JSC WGNE Res. Activ. Atmos. Oceanic Modell.*, **42**, 0105–0116.

——, and Y. Honda, 2011: Development of 1D+4DVAR data assimilation of radar reflectivity in JNoVA. *CAS/JSC WGNE Res. Activ. Atmos. Oceanic Modell.*, **41**, 0109–0110.

Ishida, J., 2007: Development of a hybrid terrain-following vertical coordinate for JMA non-hydrostatic model. *CAS/JSC WGNE Res. Activ. Atmos. Oceanic Modell.*, **37**, 0309–0310.

Japan Meteorological Agency, 2012: Tornadoes generated on 6 May 2012 (report). 14 pp. [Available online at http://www.jma.go.jp/jma/press/1206/08b/toppu120608.html] (in Japanese).

——, 2013: Tornadoes generated on 2 September 2013 (report). 2 pp. [Available online at http://www.jma.go.jp/jma/press/1309/03a/20130903_toppuu.pdf] (in Japanese).

——, 2015: Guideline about Japanese enhanced Fujita scale. 166 pp. [Available online at http://www.jma.go.jp/jma/kishou/know/toppuu/tornado1-2-2.html] (in Japanese).

Jung, Y., M. Xue, G. Zhang, and J. M. Straka, 2008a: Assimilation of simulated polarimetric radar data for a convective storm using the ensemble Kalman filter. Part II: Impact of polarimetric data on storm analysis. *Mon. Wea. Rev.*, **136**, 2246–2260.

——, G. Zhang, and M. Xue, 2008b: Assimilation of simulated polarimetric radar data for a convective storm using the ensemble Kalman filter. Part I: Observation operators for reflectivity and polarimetric variables. *Mon. Wea. Rev.*, **136**, 2228–2245.

——, M. Xue, and G. Zhang, 2010a: Simulations of polarimetric radar signatures of a supercell storm using a two-moment bulk microphysics scheme. *J. Appl. Meteor. Climatol.*, **49**, 146–163.

——, ——, and ——, 2010b: Simultaneous estimation of microphysical parameters and the atmospheric state using simulated polarimetric radar data and an ensemble Kalman filter in the presence of an observation operator error. *Mon. Wea. Rev.*, **138**, 539–562.

Kain, J. S., 2004: The Kain-Fritsch convective parameterization: An update. *J. Appl. Meteor.*, **43**, 170–181.

——, and J. M. Fritsch, 1990: A one-dimensional entraining/detraining plume model and its application in convective parameterization. *J. Atmos. Sci.*, **47**, 2784–2802.

——, S. J. Weiss, D. R. Bright, M. E. Baldwin, J. J. Levit, G. W. Carbin, C. S. Schwartz, M. L. Weisman, K. K. Droegemeier, D. B. Weber, and K. W. Thomas, 2008: Some practical considerations regarding horizontal resolution in the first generation of operational convection-allowing NWP. *Wea. Forecasting*, **23**, 931–952.

Kalman, R. E., 1960: A new approach to linear filtering and prediction problems. *Trans. ASME J. Basic Eng.*, **82**, 35–45.

Kalnay, E., H. Li, T. Miyoshi, S.-C. Yang, and J. Ballabrera-Poy, 2007: Response to the discussion on "4-D-Var or EnKF?" by Nils Gustafsson. *Tellus*, **59A**, 778–780.

Kato, T., and H. Niino 2007: Environmental atmospheric conditions under which a tornado formed over Hokkaido Island, Japan on 7 Nov. 2006, detected from a supercell reproduced by a cloud-resolving model. Preprints, *12th Conf. on Mesoscale Processes*, Waterville Valley, NH, Amer. Meteor. Soc., 13 3.

Kawabata, T., T. Kuroda, H. Seko, and K. Saito, 2011: A cloud-resolving 4DVAR assimilation experiment for a local heavy rainfall event in the Tokyo metropolitan area. *Mon. Wea. Rev.*, **139**, 1911–1931.

Klemp, J. B., 1987: Dynamics of tornadic thunderstorms. *Annu. Rev. Fluid Mech.*, **19**, 369–402.

Koizumi, K., Y. Ishikawa, and T. Tsuyuki, 2005: Assimilation of precipitation data to the JMA mesoscale model with a four-dimensional variational method and its impact on precipitation forecasts. *SOLA*, **1**, 45–48.

Kunii, M., 2014: The 1000-member ensemble Kalman filtering with the JMA nonhydrostatic mesoscale model on the K

computer. *J. Meteorol. Soc. Japan*, **92**, 623–633.

Li, X., and J. R. Mecikalski, 2010: Assimilation of the dual-polarization Doppler radar data for a convective storm with a warm-rain radar forward operator. *J. Geophys. Res.*, **115**, D16208.

——, and ——, 2012: Impact of the dual-polarization Doppler radar data on two convective storms with a warm-rain radar forward operator. *Mon. Wea. Rev.*, **140**, 2147–2167.

——, and ——, 2013: Evaluation of the sensitivity of the dual-polarization Doppler warm-rain radar data assimilation to radar forward operators for a convective storm. *J. Meteor. Soc. Japan*, **91**, 287–304.

Lin, Y.-L., R. D. Farley, and H. D. Orville, 1983: Bulk parameterization of the snow field in a cloud model. *J. Climate Appl. Meteor.*, **22**, 1065–1092.

Liu, C., Q. Xiao, and B. Wang, 2008: An ensemble-based four-dimensional variational data assimilation scheme. Part I: Technical formulation and preliminary test. *Mon. Wea. Rev.*, **136**, 3363–3373.

——, ——, and ——, 2009: An ensemble-based four-dimensional variational data assimilation scheme. Part II: Observing system simulation experiments with advanced research WRF (ARW). *Mon. Wea. Rev.*, **137**, 1687–1704.

Lorenc, A. C., 1986: Analysis methods for numerical weather prediction. *Quart. J. Roy. Meteor. Soc.*, **112**, 1177–1194.

Maddox, R. A., 1976: An evaluation of tornado proximity wind and stability data. *Mon. Wea. Rev.*, **104**, 133–142.

Maesaka, T., M. Maki, K. Iwanami, S. Tsuchiya, K. Kieda, and A. Hoshi, 2011: Operational Rainfall Estimation by X-band MP Radar Network in MLIT, Japan, *35th Conf. on Radar Meteorology*, Pittsburgh, PA, Amer. Meteor. Soc., 142.

Markowski, P. M., 2016: An idealized numerical simulation investigation of the effects of surface drag on the development of near-surface vertical vorticity in supercell thunderstorms. *J. Atmos. Sci.*, **73**, 4349–4385.

——, and Y. P. Richardson, 2010: *Mesoscale Meteorology in Midlatitudes*. Wiley-Blackwell, 430 pp.

——, and ——, 2014: The influence of environmental low-level shear and cold pools on tornadogenesis: Insights from idealized simulations, *J. Atmos. Sci.*, **71**, 243–275.

——, J. M. Straka, and E. N. Rasmussen, 2002: Direct surface thermodynamic observations within the rear-flank downdrafts of nontornadic and tornadic supercells. *Mon. Wea. Rev.*, **130**, 1692–1721.

——, ——, and ——, 2003: Tornadogenesis resulting from the transport of circulation by a downdraft: Idealized numerical simulations. *J. Atmos. Sci.*, **60**, 795–823.

——, Y. P. Richardson, E. Rasmussen, J. Straka, R. Davies-Jones, and R. J. Trapp, 2008: Vortex lines within low-level mesocyclones obtained from pseudo-dual-Doppler radar observations. *Mon. Wea. Rev.*, **136**, 3513–3535.

Marquis, J., Y. Richardson, P. Markowski, D. Dowell, and J. Wurman, 2012: Tornado maintenance investigated with high-resolution dual-Doppler and EnKF analysis. *Mon. Wea. Rev.*, **140**, 3–27.

——, ——, ——, ——, ——, K. Kosiba, P. Robinson, and G. Romine, 2014: An investigation of the Goshen county, Wyoming, tornadic supercell of 5 June 2009 using EnKF assimilation of mobile mesonet and radar observations collected during VORTEX2. Part I: Experiment design and verification of the EnKF analyses. *Mon. Wea. Rev.*, **142**, 530–554.

Mashiko, W., 2016a: A numerical study of the 6 May 2012 Tsukuba city supercell tornado. Part I: Vorticity sources of low-level and midlevel mesocyclones. *Mon. Wea. Rev.*,**144**, 1069–1092.

——, 2016b: A numerical study of the 6 May 2012 Tsukuba city supercell tornado. Part II: Mechanisms of tornadogenesis., *Mon. Wea. Rev.*, **144**, 3077–3098.

——, H. Niino, and T. Kato, 2009: Numerical simulation of tornadogenesis in an outer-rainband minisupercell of typhoon Shanshan on 17 September 2006. *Mon. Wea. Rev.*, **137**, 4238–4260.

McDonald, J. R., and K. C. Mehta, 2004: A recommendation for an enhanced Fujita scale (EF-scale). 111 pp. [Available online at http://www.spc.noaa.gov/efscale].

Meng, M., and F. Zhang, 2007: Tests of an ensemble Kalman filter for mesoscale and regional-scale data assimilation. Part II: Imperfect model experiments. *Mon. Wea. Rev.*, **135**, 1403–1423.

——, and ——, 2008: Tests of an ensemble Kalman filter for mesoscale and regional-scale data assimilation. Part III: Comparison with 3DVAR in a real-data case study. *Mon. Wea. Rev.*, **136**, 522–540.

Meteorological Research Institute 2012: Tornadoes generated near Tsukuba, Ibaraki on 6 May 2012. [Available online at http://www.jma.go.jp/jma/press/1205/11c/120511tsukuba_tornado.pdf] (in Japanese).

Miyoshi, T., S. Yamane, and T. Enomoto, 2007: Localizing the error covariance by physical distances within a local ensemble transform Kalman filter (LETKF). *SOLA*, **3**, 89–92.

——, T., K. Kondo, and T. Imamura, 2014: The 10,240-member ensemble Kalman filtering with an intermediate AGCM. *Geophys. Res. Lett.*, **41**, 5264–5271.

Molteni, F., 2003: Atmospheric simulations using a GCM with simplified physical parametrizations. I: Model climatology and variability in multi-decadal experiments. *Clim. Dyn.*, **20**, 175–191.

Murakami, M., 1990: Numerical modeling of dynamical and microphysical evolution of an isolated convective cloud -The 19 July 1981 CCOPE cloud-. *J. Meteor. Soc. Japan*, **68**, 107–128.

Muroi, C., T. Fujita, and Y. Ishikawa, 2008: Hourly analysis at the Japan Meteorological Agency. *Tenki*, **55**, 401–408. (in Japanese).

Nakanishi, M., 2001: Improvement of the Mellor-Yamada turbulence closure model based on large-eddy simulation data. *Bound.-Layer Meteor.*, **99**, 349–378.

——, and H. Niino, 2004: An improved Mellor-Yamada Level-3 model with condensation physics: Its design and verification. *Bound.-Layer Meteor.*, **112**, 1–31.

——, and ——, 2006: An improved Mellor–Yamada Level-3 model: Its numerical stability and application to a regional prediction of advection fog. *Bound.-Layer Meteor.*, **119**, 397–407.

Navon, I. M., and D. M. Legler, 1987: Conjugate-gradient methods for large-scale minimization in meteorology. *Mon. Wea. Rev.*, **115**, 1479–1502.

Niino, H., O. Suzuki, H. Nirasawa, T. Fujitani, H. Ohno, I. Takayabu, N. Kinoshita, and Y. Ogura, 1993: Tornadoes in Chiba Prefecture on 11 December 1990. *Mon. Wea. Rev.*, **121**, 3001–3018.

Nishi, A., K. Araki, K. Saito, T. Kawabata, and H. Seko, 2015: The consideration and application of the quality control

method for the atmospheric environmental regional observation system (AEROS) meteorological observation data. *Tenki*, **8**, 627–639 (in Japanese).

Nocedal, J., 1980: Updating quasi-Newton matrices with limited storage. *Math. Computation*, **35**, 773–782.

Parker M. D. and J. M. L. Dahl, 2015: Production of near-surface vertical vorticity by idealized downdrafts. *Mon. Wea. Rev.*, **143**, 2795–2816.

Putnam, B. J., M. Xue, Y. Jung, N. Snook, and G. Zhang, 2014: The analysis and prediction of microphysical states and polarimetric radar variables in a mesoscale convective system using double-moment microphysics, multinetwork radar data, and the ensemble Kalman filter. *Mon. Wea. Rev.*, **142**, 141–162.

Rasmussen, E. N., J. M. Straka, R. Davies-Jones, C. A. Doswell, F. H. Carr, M. D. Eilts, and D. R. MacGorman, 1994: Verification of the Origins of Rotation in Tornadoes Experiment: VORTEX. *Bull. Amer. Meteor. Soc.*, **75**, 995–1006.

Richardson, Y. P., K. K. Droegemeier, and R. P. Davies-Jones, 2007: The influence of horizontal environmental variability on numerically simulated convective storms. Part I: Variations in vertical shear. *Mon. Wea. Rev.*, **135**, 3429–3455.

Roberts, B., M. Xue, A. D. Schenkman, and D. T. Dawson, 2016: The role of surface drag in tornadogenesis within an idealized supercell simulation. *J. Atmos. Sci.*, **73**, 3371–3395.

Rotunno, R., and J. Klemp, 1982: The influence of the shear-induced pressure gradient on thunderstorm motion. *Mon. Wea. Rev.*, **110**, 136–151.

——, and ——, 1985: On the rotation and propagation of simulated supercell thunderstorms. *J. Atmos. Sci.*, **42**, 271–292.

Sachidananda, M., and D. S. Zrnic, 1986: Differential propagation phase shift and rainfall rate estimation. *Radio Sci.*, **21**, 235–247.

——, and ——, 1987: Rain rate estimates from differential polarization measurements. *J. Atmos. Oceanic Technol.*, **4**, 588–598.

Saito, K., and Coauthors, 2006: The operational JMA nonhydrostatic mesoscale model. *Mon. Wea. Rev.*, **134**, 1266–1298.

Sasaki, Y., 1958: An objective analysis based on the variational method. *J. Meteor. Soc. Japan*, **36**, 77–88.

——, 1969: Proposed inclusion of time variation terms, observational and theoretical, in numerical variational objective analysis. *J. Meteor. Soc. Japan*, **47**, 115–124.

——, 1970: Some basic formalisms in numerical variational analysis. *Mon. Wea. Rev.*, **98**, 875–883.

Schenkman, A. D., M. Xue, A. Shapiro, K. Brewster, and J. Gao, 2011a: The analysis and prediction of the 8–9 May 2007 Oklahoma tornadic mesoscale convective system by assimilating WSR-88D and CASA radar data using 3DVAR. *Mon. Wea. Rev.*, **139**, 224–246.

——, ——, ——, ——, and ——, 2011b: Impact of CASA radar and Oklahoma mesonet data assimilation on the analysis and prediction of tornadic mesovortices in an MCS. *Mon. Wea. Rev.*, **139**, 3422–3445.

——, ——, and ——, 2012: Tornadogenesis in a simulated mesovortex within a mesoscale convective system, *J. Atmos. Sci.*, **69**, 3372–3390.

——, ——, and M. Hu, 2014: Tornadogenesis in a high-resolution simulation of the 8 May 2003 Oklahoma city

supercell., *J. Atmos. Sci.*, **71**, 130–154.

Seko, H., T. Kawabata, T. Tsuyuki, H. Nakamura, K. Koizumi, and T. Iwabuchi, 2004: Impacts of GPS-derived water vapor and radial wind measured by Doppler radar on numerical prediction of precipitation. *J. Meteor. Soc. Japan*, **82**, 473–489.

——, T. Tsuyuki, K. Saito, and T. Miyoshi, 2013: Development of a two-way nested LETKF system for cloud-resolving model. *Data Assimilation for Atmospheric, Oceanic and Hydrologic Applications*, **2**, 489–507.

——, M. Kunii, S. Yokota, T. Tsuyuki, and T. Miyoshi, 2015: Ensemble experiments using a nested LETKF system to reproduce intense vortices associated with tornadoes of 6 May 2012 in Japan. *Prog. Earth Planet. Sci.*, **2**, 42.

Shoji, Y., W. Mashiko, H. Yamauchi, and E. Sato, 2015: Estimation of local-scale precipitable water vapor distribution around each GNSS station using slant path delay: Evaluation of a tornado case using high-resolution NHM. *SOLA*, **11**, 31–35.

Snook, N., M. Xue, and Y. Jung, 2012: Ensemble probabilistic forecasts of a tornadic mesoscale convective system from ensemble Kalman filter analyses using WSR-88D and CASA radar data. *Mon. Wea. Rev.*, **140**, 2126–2146.

——, ——, and ——, 2015: Multiscale EnKF assimilation of radar and conventional observations and ensemble forecasting for a tornadic mesoscale convective system. *Mon. Wea. Rev.*, **143**, 1035–1057.

Snyder, C., and F. Zhang, 2003: Assimilation of simulated Doppler radar observations with an ensemble Kalman filter. *Mon. Wea. Rev.*, **131**, 1663–1677.

Sobash, R. A., and D. J. Stensrud, 2015: Assimilating surface mesonet observations with the EnKF to improve ensemble forecasts of convection initiation on 29 May 2012. *Mon. Wea. Rev.*, **143**, 3700–3725.

Stensrud, D. J., and J. Gao, 2010: Importance of horizontally inhomogeneous environmental initial conditions to ensemble storm-scale radar data assimilation and very short-range forecasts. *Mon. Wea. Rev.*, **138**, 1250–1272.

——, M. Xue, L. J. Wicker, K. E. Kelleher, M. P. Foster, J. T. Schaefer, R. S. Schneider, S. G. Benjamin, S. S. Weygandt, J. T. Ferree, and J. P. Tuell, 2009: Convective-scale warn-on-forecast system. *Bull. Amer. Meteor. Soc.*, **90**, 1487–1499.

——, and Coauthors, 2013: Progress and challenges with Warn-on-Forecast, *Atmos. Res.*, **123**, 2–16.

Straka, J. M., E. N. Rasmussen, R. P. Davies-Jones, and P. M. Markowski, 2007: An observational and idealized numerical examination of low-level counter-rotating vortices in the rear flank of supercells. *Electronic J. Severe Storms Meteor.*, **2**, 1–22

Sun, J., and N. A. Crook, 1997: Dynamical and microphysical retrieval from Doppler radar observations using a cloud model and its adjoint. Part I: Model development and simulated data experiments. *J. Atmos. Sci.*, **54**, 1642–1661.

Tabary, P., G. Vulpiani, J. J. Gourley, A. J. Illingworth, R. J. Thompson, and O. Bousquet, 2009: Unusually High Differential Attenuation at C Band: Results from a Two-Year Analysis of the French Trappes Polarimetric Radar Data. *J. Appl. Meteor. Climatol.*, **48**, 2037–2053.

Tanamachi, R. L., L. J. Wicker, D. C. Dowell, H. B. Bluestein, D. T. Dawson, and M. Xue, 2013: EnKF assimilation of high-resolution, mobile Doppler radar data of the 4 May 2007 Greensburg, Kansas, supercell into a numerical cloud

model. *Mon. Wea. Rev.*, **141**, 625–648.

Thompson, P. D., 1969: Reduction of analysis error through constraints of dynamical consistency. *J. Appl. Meteor.*, **8**, 738–742.

Tong, M., and M. Xue, 2005: Ensemble Kalman filter assimilation of Doppler radar data with a compressible nonhydrostatic model: OSS experiments. *Mon. Wea. Rev.*, **133**, 1789–1807.

Torn, R. D., and G. J. Hakim, 2008: Ensemble-based sensitivity analysis. *Mon. Wea. Rev.*, **136**, 663–677.

Trapp, R. J., G. J. Stumpf, and K. L. Manross, 2005: A reassessment of the percentage of tornadic mesocyclones. *Wea. Forecasting*, **20**, 680–687.

Tromel, S., M. R. Kumjian, A. V. Ryzhkov, C. Simmer, and M. Diederich, 2013: Backscatter differential phase—estimation and Variability. *J. Appl. Meteor. Climatol.*, **52**, 2529–2548.

Tsuyuki, T., 2014: Deterministic predictability of the most probable state and reformulation of variational data assimilation. *J. Meteorol. Soc. Japan*, **92**, 599–622.

Weisman, M. L., and J. B. Klemp, 1982: The dependence of numerically simulated convective storms on vertical wind shear and buoyancy. *Mon. Wea. Rev.*, **110**, 504–520.

Wicker, L. J., and R. B. Wilhelmson, 1995: Simulation and analysis of tornado development and decay within a three-dimensional supercell thunderstorm. *J. Atmos. Sci.*, **52**, 2675–2703.

Whitaker, J. S., and T. H. Hamill, 2002: Ensemble data assimilation without perturbed observations. *Mon. Wea. Rev.*, **130**, 1913–1924.

Wurman, J., D. Dowell, Y. Richardson, P. Markowski, E. Rasmussen, D. Burgess, L. Wicker, and H. B. Bluestein, 2012: The Second Verification of the Origins of Rotation in Tornadoes Experiment: VORTEX2. *Bull. Amer. Meteor. Soc.*, **93**, 1147–1170.

Xue, M., M. Tong, and K. K. Droegemeier, 2006: An OSSE framework based on the ensemble square root Kalman filter for evaluating the impact of data from radar networks on thunderstorm analysis and forecasting. *J. Atmos. Oceanic Technol.*, **23**, 46–66.

——, M. Hu, and A. D. Schenkman, 2014: Numerical prediction of the 8 May 2003 Oklahoma city tornadic supercell and embedded tornado using ARPS with the assimilation of WSR-88D data. *Wea. Forecasting*, **29**, 39–62.

Yamauchi, H., O. Suzuki, and K. Akaeda, 2006: A hybrid multi-PRI method to dealias Doppler velocities. *SOLA*, **2**, 92–95.

——, H. Niino, O. Suzuki, Y. Shoji, E. Sato, A. Adachi, and W. Mashiko, 2013: Vertical structure of the Tsukuba F3 tornado on 6 May 2012 as revealed by a polarimetric radar. Preprints, *36th Conf. on Radar Meteorology*, Breckenridge, CO, Amer. Meteor. Soc., 320.

Yang, S.-C., M. Corazza, A. Carrassi, E. Kalnay, and T. Miyoshi, 2009: Comparison of local ensemble transform Kalman filter, 3DVAR, and 4DVAR in a quasigeostrophic model. *Mon. Wea. Rev.*, **137**, 693–709.

Yokota, S., M. Kunii, K. Aonashi, and S. Origuchi, 2016a: Comparison between four-dimensional LETKF and ensemble-based variational data assimilation with observation localization. *SOLA*, **12**, 80–85.

——, H. Seko, M. Kunii, H, Yamauchi, and H. Niino, 2016b: The tornadic supercell on the Kanto Plain on 6 May 2012: Polarimetric radar and surface data assimilation with EnKF and ensemble-based sensitivity analysis. *Mon. Wea. Rev.*, **144**, 3133–3157.

Yoshino, J., H. Ishikawa, and H. Ueda, 2002: MM5 simulations of the 24 September 1999 tornadic outbreaks in the outer rainband associated with Typhoon Bart. Preprints, *12th PSU/NCAR Mesoscale Model Users' Workshop*, Boulder, CO, Univ. Corp. Atmos. Res., 5 1.

Yussouf, N., E. R. Mansell, L. J. Wicker, D. M. Wheatley, and D. J. Stensrud, 2013a: The ensemble Kalman filter analyses and forecasts of the 8 May 2003 Oklahoma city tornadic supercell storm using single- and double-moment microphysics schemes. *Mon. Wea. Rev.*, **141**, 3388–3412.

——, J. Gao, D. J. Stensrud, and G. Ge, 2013b: The impact of mesoscale environmental uncertainty on the prediction of a tornadic supercell storm using ensemble data assimilation approach. *Adv. Meteor.*, **2013**, 1–15

Zhang, F., C. Snyder, and J. Sun, 2004: Impacts of initial estimate and observation availability on convective-scale data assimilation with an ensemble Kalman filter. *Mon. Wea. Rev.*, **132**, 1238–1253.

——, Z. Meng, and A. Aksoy, 2006: Tests of an ensemble Kalman filter for mesoscale and regional-scale data assimilation. Part I: Perfect model experiments. *Mon. Wea. Rev.*, **134**, 722–736.

Zupanski, M., 2005: Maximum likelihood ensemble filter: Theoretical aspects. *Mon. Wea. Rev.*, **133**, 1710–1726.

——, I. M. Navon, and D. Zupanski, 2008: The maximum likelihood ensemble filter as a non-differentiable minimization algorithm. *Quart. J. Roy. Meteor. Soc.*, **134**, 1039–1050.